National Library of Canada
Bibliothèque nationale du Canada

Canadian Theses Service
Service des thèses canadiennes

Ottawa, Canada
K1A 0N4

NOTICE

The quality of this microform is heavily dependent upon the quality of the original thesis submitted for microfilming. Every effort has been made to ensure the highest quality of reproduction possible.

If pages are missing, contact the university which granted the degree.

Some pages may have indistinct print especially if the original pages were typed with a poor typewriter ribbon or if the university sent us an inferior photocopy.

Reproduction in full or in part of this microform is governed by the Canadian Copyright Act, R.S.C. 1970, c. C-30, and subsequent amendments.

AVIS

La qualité de cette microforme dépend grandement de la qualité de la thèse soumise au microfilmage. Nous avons tout fait pour assurer une qualité supérieure de reproduction.

S'il manque des pages, veuillez communiquer avec l'université qui a conféré le grade.

La qualité d'impression de certaines pages peut laisser à désirer, surtout si les pages originales ont été dactylographiées à l'aide d'un ruban usé ou si l'université nous a fait parvenir une photocopie de qualité inférieure.

La reproduction, même partielle, de cette microforme est soumise à la Loi canadienne sur le droit d'auteur, SRC 1970, c. C-30, et ses amendements subséquents.

NL-339 (r. 88/04) c

Canada

UNIVERSITY OF ALBERTA

ELECTRON TUNNELING: INELASTIC ELECTRON TUNNELING SPECTROSCOPY AND LOW TEMPERATURE SCANNING TUNNELING MICROSCOPY

BY

MARK GALLAGHER

A THESIS
SUBMITTED TO THE FACULTY OF GRADUATE STUDIES AND
RESEARCH IN PARTIAL FULFILLMENT OF THE REQUIREMENTS FOR
THE DEGREE OF DOCTOR OF PHILOSOPHY
IN
SOLID STATE PHYSICS
DEPARTMENT OF PHYSICS

EDMONTON, ALBERTA
SPRING 1990

National Library of Canada
Bibliotheque nationale du Canada

Canadian Theses Service
Service des thèses canadiennes

Ottawa, Canada
K1A 0N4

NOTICE

The quality of this microform is heavily dependent upon the quality of the original thesis submitted for microfilming. Every effort has been made to ensure the highest quality of reproduction possible.

If pages are missing, contact the university which granted the degree.

Some pages may have indistinct print especially if the original pages were typed with a poor typewriter ribbon or if the university sent us an inferior photocopy.

Reproduction in full or in part of this microform is governed by the Canadian Copyright Act, R.S.C. 1970, c. C-30, and subsequent amendments.

AVIS

La qualité de cette microforme dépend grandement de la qualité de la thèse soumise au microfilmage. Nous avons tout fait pour assurer une qualité supérieure de reproduction.

S'il manque des pages, veuillez communiquer avec l'université qui a conféré le grade.

La qualité d'impression de certaines pages peut laisser à désirer, surtout si les pages originales ont été dactylographiées à l'aide d'un ruban usé ou si l'université nous a fait parvenir une photocopie de qualité inférieure.

La reproduction, même partielle, de cette microforme est soumise à la Loi canadienne sur le droit d'auteur, SRC 1970, c. C-30, et ses amendements subséquents.

ISBN 0-315-60336-4

NL-339 (r. 88/04) c

Canada

UNIVERSITY OF ALBERTA

RELEASE FORM

NAME OF AUTHOR: MARK GALLAGHER

TITLE OF THESIS: ELECTRON TUNNELING: INELASTIC ELECTRON TUNNELING SPECTROSCOPY AND LOW TEMPERATURE SCANNING TUNNELING MICROSCOPY

DEGREE: DOCTOR OF PHILOSOPHY

YEAR THIS DEGREE GRANTED: 1990

PERMISSION IS HEREBY GRANTED TO THE UNIVERSITY OF ALBERTA LIBRARY TO REPRODUCE SINGLE COPIES OF THIS THESIS AND TO LEND OR SELL SUCH COPIES FOR PRIVATE, SCHOLARLY OR SCIENTIFIC PURPOSES ONLY.

THE AUTHOR RESERVES OTHER PUBLICATION RIGHTS, AND NEITHER THE THESIS NOR EXTENSIVE EXTRACTS FROM IT MAY BE PRINTED OR OTHERWISE REPRODUCED WITHOUT THE AUTHOR'S WRITTEN PERMISSION.

Mark Gallagher

629 GALEN DRIVE,
STATE COLLEGE, PA 16803,
U.S.A.

Date: December 5 1989

UNIVERSITY OF ALBERTA

FACULTY OF GRADUATE STUDIES AND RESEARCH

THE UNDERSIGNED CERTIFY THAT THEY HAVE READ, AND RECOMMEND TO THE FACULTY OF GRADUATE STUDIES AND RESEARCH FOR ACCEPTANCE, A THESIS ENTITLED ELECTRON TUNNELING: INELASTIC ELECTRON TUNNELING AND LOW TEMPERATURE SCANNING TUNNELING MICROSCOPY SUBMITTED BY MARK GALLAGHER IN PARTIAL FULFILLMENT OF THE REQUIREMENTS FOR THE DEGREE OF DOCTOR OF PHILOSOPHY IN SOLID STATE PHYSICS.

Dr. J.G. Adler

Dr. J.P. Franck

Dr. J.S. Rogers

Dr. Z.W. Gortel

Dr. R.G. Cavell

Dr. J. Talvacchio

Date: November 28 1989

TO MY FAMILY

Abstract

This thesis describes experiments encompassing both Inelastic Electron Tunneling Spectroscopy (IETS) and Scanning Tunneling Microscopy (STM). IETS is used to study the tunneling characteristics of undoped Mg-MgO-metal tunnel junctions. The development of a low temperature STM, and it's use to study high T_c superconductors is discussed.

The IETS experiments indicate that tunneling characteristics can be improved by increasing the uniformity of the barrier. Uniform oxidation was achieved by oxidizing in a wet environment, or by pretreating the Mg with hydrogen. The pretreated junctions exhibited a 124 meV peak in the IET spectra indicating chemisorbed hydrogen at the magnesium surface. Hydrogen acted as a nucleation site for oxidation, promoting uniform growth. Using different cover electrodes it was found that metals with smaller ionic radii penetrate into the oxide at pinholes and defects. The effect was reduced in hydrogen junctions indicating a smaller degree of imperfections. Different cover electrodes shifted the IETS hydroxyl peak to lower energies due to an image dipole effect[1]. The shift was larger with Mg negatively biassed.

Design and operation of a low temperature microscope is presented. Measurements of $NbSe_2$ at 4.2 K indicate that the microscope is capable of atomic resolution, and spectroscopy with millivolt resolution. The STM was used to measure a number of $YBa_2Cu_3O_{6.5+x}$ (YBC), and $BiSrCaCu_2O_x$ samples at 4.2 K. A non-conducting layer on most of the samples meant the tip had to be driven into the surface to tunnel, preventing scanning. The short coherence lengths produced large spatial variations in the tunneling characteristics. Many curves exhibited charging effects. Curves exhibiting a Coulomb Blockade or the Coulomb staircase[2]

were often observed. Many curves were dominated by tunneling between grains rather than tunneling between sample and tip. Ambiguity regarding the exact tunneling mechanism makes unambiguous estimate of the energy gap impossible. A 5 meV gap was observed in the YBC ceramics indicating a low temperature phase. The non-conducting layer was not observed on a number of YBC films. The surface exhibited a thin conducting shell, and measurements indicated that superconductivity could persist out to the surface. Energy gap values as high as 20 meV were observed.

---

1 J.R. Kirtley and P.K. Hansma, Phys. Rev. B 13, 2910 (1976).
2 K.A. Mullen, E. Ben-Jacob, R.C. Jaklevic and Z. Schuss, Phys. Rev. B. 37, 98 (1988).

Acknowledgements

I would like to express my gratitude to my research supervisor Dr J.G. Adler for his encouragement and guidance throughout the course of my apprenticeship. I also wish to thank Dr Adler for providing me the opportunity to attend a number of exciting conferences.

Thanks also to Mr D.P. Mullin for his valuable and enthusiastic technical assistance. Many of the successes in development the STM can be attributed to numerous fruitful coffee time discussions with Mr Mullin and Dr Adler.

The IETS experiments were performed in collaboration with my friend and colleague Mr Y.B. Ning.

I wish to acknowledge the generosity of Drs J. Jung and J.P. Franck at the University of Alberta, Drs A. Fife and J. Vrba at CTF Systems Inc., and Dr J.E. Greedan at McMaster for providing samples for the STM. Thanks also Mr S. Rogers for providing the necessary liquid helium and to Ms. M. Konkin for providing the $NbSe_2$ image which appears in this thesis.

The financial support of both the Physics Department and the Natural Sciences and Engineering Research Council has been gratefully appreciated.

Most of all I would like to thank my wife Moira. Without her patience, and moral support throughout my years of study this thesis would not have been possible.

Table of Contents

1 Introduction 1

2 Theoretical Considerations 4

3 Inelastic Electron Tunneling Spectroscopy. 9
- 3.1 Theory of Elastic Tunneling 13
- 3.2 Inelastic Tunneling Theory 20
- 3.3 Measurement of Tunneling Characteristics 29
  - 3.3.1 Modulation Spectroscopy. 29
  - 3.3.2 Data Collection. 32
  - 3.3.3 Calibration. 35
- 3.4 Data Analysis 37
  - 3.4.1 Peak identification 37
  - 3.4.2 Barrier Parameters. 44
  - 3.4.3 Peak Intensity 44
- 3.5 Sample Preparation. 46
  - 3.5.1 Formation of the Tunneling Barrier. 50
  - 3.5.2 Cover Electrode Formation. 51
- 3.6 Results and discussion 53
  - 3.6.1 Results 53
  - 3.6.2 Gun Junctions 60
  - 3.6.3 Oxidation 65
  - 3.6.4 Infleuence of Cover Electrode 72
  - 3.6.5 Summary 88

4 Low Temperature Scanning Tunneling Microscopy and Spectroscopy. 90
- 4.1 Theory of Scanning Tunneling Microscopy and Spectroscopy 94
- 4.2 Superconductivity and Superconducting Tunneling 103
- 4.3 Experimental Techniques 120
  - 4.3.1 Microscope Design 120
  - 4.3.2 Experimental Setup 132
  - 4.3.3 Tip preparation 136
  - 4.3.4 Calibration 137
- 4.4 Experimental Results 142
  - 4.4.1 Performance 142
  - 4.4.2 Scanning Tunneling Microscopy and Spectroscopy of High Temperature Superconductors. 146
    - 4.4.2.1 Structure of the Oxide Superconductors 147
    - 4.4.2.2 Spectroscopic Measurements of the Ceramic and Single Crystal Samples 150
    - 4.4.2.3 Topographic and Spectroscopic Studies of $YBa_2Cu_3O_x$ Films 175

5 Summary and Conclusions 195
- 5.1 Discussion 195
- 5.2 Suggestions for Further Work 198

6 Bibliography 200

Table of Tables

TABLE 3.1 Peak Assignment for Mg-MgO-Pb Tunnel Junctions 43

TABLE 3.2 Evaporation Materials for Mg-MgO-Metal Junctions 50

TABLE 3.3 Barrier Parameters of Mg-MgO-Metal Junctions 59

TABLE 3.4 O-H Peak Intensities and Peak Positions for Mg-MgO-Metal Junctions 77

Table of Figures

FIGURE 2.1 Transfer Hamiltonian 6

FIGURE 3.1 Inelastic Electron Tunneling 11

FIGURE 3.2 Energy Level diagram of a Metal-Insulator-Metal Junction 15

FIGURE 3.3 Modulation spectroscopy 31

FIGURE 3.4 A.C. Wheatstone bridge 34

FIGURE 3.5 IET Spectra of a Mg-MgO-Pb Plasma Junction 39

FIGURE 3.6 Tunnel Junction Sample Geometry 48

FIGURE 3.7 IET Spectra of Mg-MgO-Metal Junctions 55

FIGURE 3.8 IET Spectra of Hydrogen and Deuterium Treated Mg-MgO-Pb Junctions 62

FIGURE 3.9 H Chemisorption on the Mg(0001) Surface 67

FIGURE 3.10 Initial Oxidation of the Mg(0001) Surface 69

FIGURE 3.11 Barrier Height of Mg-MgO-Metal Junctions vs. the Ionic Radius of the Cover Electrode 75

FIGURE 3.12 Energy of the Hydroxyl IETS Peak vs. the Atomic Radius of the Covermetal 80

FIGURE 3.13 Energy of the Hydroxyl IETS Peak vs. the d Character of the Covermetal 83

FIGURE 3.14 Polarity Shift vs. the Cover Electrode Shift of the Hydroxyl Peak 86

FIGURE 4.1 STM Schematic 92

FIGURE 4.2 Metal-Insulator-Superconductor Tunneling 106

FIGURE 4.3 Superconductor-Insulator-Superconductor Tunneling 111

FIGURE 4.4 Andreev Reflection 114

FIGURE 4.5 Tunneling and Point Contact Characteristics of a Pb Film 116

FIGURE 4.6 Point Contact Characteristics of a YBC Ceramic Sample 118

FIGURE 4.7 Piezoelectric Actuators of the Bimorph Microscope 122
FIGURE 4.8 Sectored Piezoelectric Tube 125
FIGURE 4.9 Bimorph Microscope 127
FIGURE 4.10 Tube Microscope 131
FIGURE 4.11 Schematic of the Experimental STM/STS Setup 134
FIGURE 4.12 Atomic Resolution STM Image of Highly Ordered Pyrolytic Graphite 140
FIGURE 4.13 STM Image and I-V Curve of $NbSe_2$ 144
FIGURE 4.14 Crystal Structure of $YBa_2Cu_3O_7$ 149
FIGURE 4.15 Crystal Structure of $BiSrCaCu_2O_8$ 152
FIGURE 4.16 Tunneling Characteristics of an Al Doped YBC Sample 156
FIGURE 4.17 Tunneling Characteristics of a YBC Single Crystal 158
FIGURE 4.18 5 meV Energy Gap Obtained on a YBC Ceramic Sample 161
FIGURE 4.19 Asymmetric Tunneling Characteristics of an Al Doped YBC Sample 164
FIGURE 4.20 Tunneling in Small Capacitance Junctions 167
FIGURE 4.21 Resistance Dependent Tunneling Characteristics of $BiSrCaCu_2O_X$ 172
FIGURE 4.22 Large Area STM Image of a YBC film 178
FIGURE 4.23 Scanning Electron Micrograph of a YBC Film 180
FIGURE 4.24 Cross section of a YBC Film 182
FIGURE 4.25 Spatially Resolved Spectroscopy on a YBC Film 185
FIGURE 4.26 Coulomb Blockade Obtained on a YBC Film 187
FIGURE 4.27 Coulomb Staircase Obtained on a YBC Film 190
FIGURE 4.28 Area of low surface conductivity on a YBC Film 194

1 Introduction

The concept of a particle tunneling through a classically forbidden region is as old as Quantum Mechanics. In the case of electrons, if the forbidden region is sufficiently thin, there exists a finite quantum mechanical probability that electrons can tunnel through the potential barrier rather than having to go over it. The first discussion of electron tunneling between two metals separated by a vacuum was presented by Frenkel (1930). Frenkel's ideas were extended by Sommerfeld and Bethe (1933) to consider tunneling through a thin insulating layer. The first experimental observation of electron tunneling in a metal - insulator - metal system did not occur until 1960, when thin film technology became sufficiently advanced, and allowed Fisher and Giaever (1960) to fabricate an aluminum - aluminum oxide - aluminum tunnel junction. Utilizing this new found technique, Giaever (1960a, 1960b) was able to directly measure the quasiparticle density of states in superconducting electrodes, and thus provide direct experimental evidence for the superconducting energy gap as predicted by the theory of Bardeen, Cooper, and Schrieffer (BCS) (1957). Subsequent tunneling experiments with superconducting electrodes demonstrated how tunneling can provide a measure of both the strength and the detailed dynamics of the interaction giving rise to superconductivity in various materials (Schrieffer et al., 1963; McMillan and Rowell, 1965).

One of the appealing features of electron tunneling is that by applying a voltage across the junction, an electron flux with a well defined energy $0 \leq E \leq eV$ is produced. This enables tunneling to provide spectroscopic information with an energy resolution of k_BT. In addition to the superconducting spectroscopy developed by Giaever, the technique of inelastic electron tunneling spectroscopy

(IETS) can investigate inelastic excitations like phonon generation, plasmons, spin waves, and a host of other processes which occur either in the electrodes, or the barrier region and may be excited by tunneling electrons (Wolf, 1985).

One application of IETS is the measurement of the vibrational frequencies of molecules incorporated into the junction (Jaklevic and Lambe, 1966). Peaks in $d\sigma/dV$ (d^2I/dV^2) correspond to vibrational modes of these molecules, and the identification of the peaks provides insight into the bonding of molecules at solid surfaces, and any reactions which the molecules may undergo.

Recently Binnig, Rohrer and coworkers (Binnig et al., 1982a, 1982b) have developed a new technique based on the original concepts of vacuum tunneling. Scanning tunneling microscopy (STM) exploits the tunneling current which occurs when a fine metal tip and a conducting surface are brought into close proximity. A feedback mechanism is used to stabilize the tunnel current and thus maintain a constant separation between the sample and tip. If the tip is rastered across the surface, structure on the surface will cause the tip to follow in a corresponding manner. By recording the feedback signal as a function of tip position, a three dimensional map of the surface may be constructed. With sharp enough tips the resolution of STM is of the order of Ångstroms and enables the imaging of surface atoms in real space. Although first developed in vacuum, STM works equally well in air, or liquids such as water, or liquid He^4 (Park and Quate, 1985; Sonnenfeld and Hansma, 1986; Elrod et al., 1984). Low temperature scanning tunneling microscopy was first demonstrated by de Lozanne et al. (1985) who measured the spatial variation of the superconducting energy gap in Nb_3Sn. The tip and sample in the

STM are essentially a microscopic tunnel junction, and combined with the scanning capability, enable tunneling spectroscopy to be performed spatially on an atomic scale.

This thesis describes two series of experiments which encompass different aspects of electron tunneling. The first is an IETS study of undoped Mg-MgO-metal tunnel junctions. The purpose of the work is to try to understand the variability between the observed IET spectra obtained at different laboratories. The effect of different vacuum conditions, and preparation techniques on the oxidation of the magnesium surface, and subsequent barrier formation are discussed. In particular, how chemisorbed hydrogen, or hydroxyls can promote uniform oxide growth is discussed. The effect of the cover electrode on the resultant IET spectra is also considered.

The remainder of the thesis is devoted to the subject of low temperature STM. The development of a low temperature scanning tunneling microscope, including it's design, and operation is presented. The STM is used to perform a series of experiments to investigate the surface properties of a number of high temperature superconductors. In addition to revealing a number of intrinsic properties of the materials studied, the experiments produced a number of more general results concerning tunneling into granular materials.

2 Theoretical Considerations

This chapter provides a theoretical basis for the process of electron tunneling. The most widely used technique to describe electron tunneling was developed by Bardeen (1961). The technique has been applied to a wide variety of tunneling problems including the case of metal-insulator-metal thin film tunnel junctions, and the three dimensional problem of STM.

The transfer Hamiltonian approach relies on the fact that any electron incident to the tunnel barrier has a near unity probability being reflected. In this context a perturbation approach to tunneling is appropriate. Bardeen considered the tunnel junction as two nearly independent electrodes, each described by the Hamiltonians H_L and H_R and corresponding eigenfunctions Ψ_L and Ψ_R. The barrier is treated as a perturbing potential through which the two electrodes are weakly coupled, and tunneling as the transition of an electron from one electrode to the other.

The wavefunctions Ψ_L and Ψ_R resemble standing waves in each electrode, and decay exponentially within the barrier, continuing to zero in the opposite electrodes. Figure 1 shows a schematic representation of the tunnel junction in the Bardeen picture.

The Hamiltonian for the system, including tunneling, can be expressed as

$$H = H_L + H_R + H^T \tag{2.1}$$

with H^T describing the tunneling process or the coupling between the two electrodes. This choice of Hamiltonian allows the use of standard time dependent perturbation theory (Liboff, 1980) to express the transition rate for tunneling in the form

FIGURE 2.1 Schematic representation of the tunnel junction in the Bardeen picture. The barrier is considered as a perturbing potential through which the two electrodes are weakly coupled.

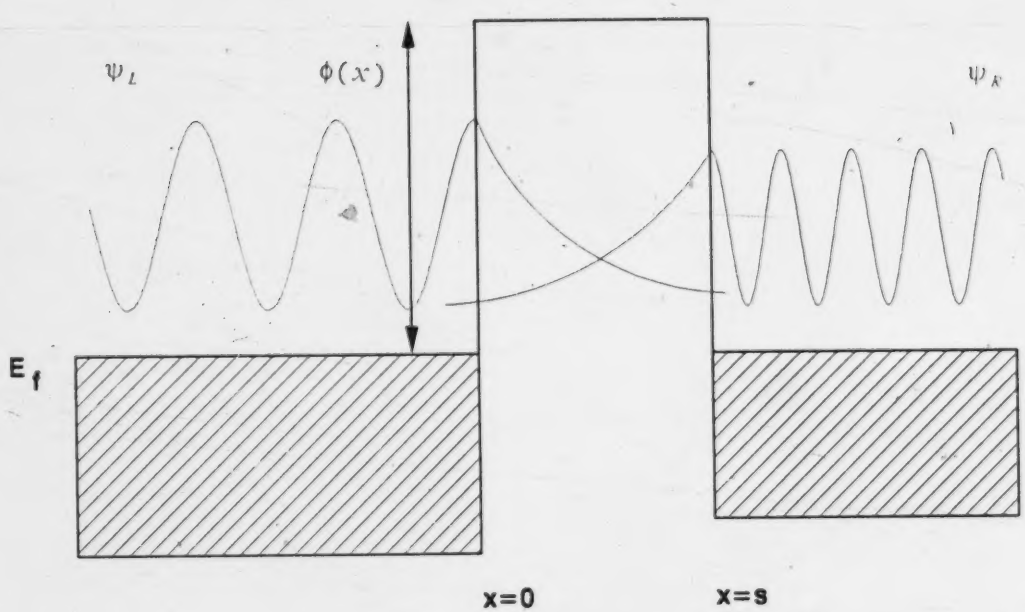
ψ_L
$\phi(x)$
ψ_R
E_f
x=0
x=s

$$w_{LR} = \left(\frac{2\pi}{\hbar}\right) |<\Psi_R|H^T|\Psi_L>|^2 \rho_R(E_R)\delta(E_R - E_L) \tag{2.2}$$

where $<\Psi_R|H^T|\Psi_L>$ is the tunneling matrix element, $\rho_R(E_R)$ is the density of states available to tunnel into in the right electrode at energy E_R, and the delta function ensures conservation of energy.

To estimate the transition probability per unit time of an electron traversing the barrier, the probability that electron states in electrode L at energy E_L are occupied $f(E_L)$, and states in electrode R are empty $(1-f(E_R))$, must be considered, and yields the result

$$P_{LR} = \left(\frac{2\pi}{\hbar}\right) |<\Psi_R|H^T|\Psi_L>|^2 \rho_R(E_R) f(E_L)(1 - f(E_R))\delta(E_R - E_L) \tag{2.3}$$

where f(E) are Fermi functions of the form

$$f(E) = \frac{1}{1 - e^{(E-E_f)/k_B T}} \tag{2.4}$$

and E_f is the Fermi energy of the electrode, k_B is Boltzmann's constant, and T the temperature in degrees Kelvin.

To simplify the problem, the barrier is assumed to be planar and $k_{||}$, the momentum parallel to the barrier, is conserved during tunneling i.e. specular reflection. To obtain the tunnel current from electrode L to electrode R, P_{LR} is summed over states in L with constant $k_{||}$, multiplied by 2 to include spin, and by e for charge. The sum over states in electrode L is equivalent to an integration in energy over the density of states at fixed $k_{||}$. To obtain the net current the corresponding current flow from electrode R to electrode L is subtracted, and the result is

$$j = \frac{4\pi e}{\hbar} \sum_{k_{||}} \int_0^\infty |<\Psi_R|H^T|\Psi_L>|^2 \rho_L(E_x)\rho_R(E_x + eV)\{f(E) - f(E+eV)\}dE_x \tag{2.5}$$

where ρ_i are one dimensional density of states associated with motion perpendicular to the barrier. The expression has been simplified by using the fact that $E_x = E - E_{||}$, and by setting $E_L = E$, and $E_R = E + eV$, where V is the bias potential across the junction.

To calculate the tunnel current more explicitly, the problem requires evaluation of the tunneling matrix $|<\Psi_R|H^T|\Psi_L>|^2$. Bardeen simplified this task by demonstrating that the matrix element can be rewritten in terms of the current density operator

$$<\Psi_R|H^T|\Psi_L> = -i\hbar <\Psi_R|j|\Psi_L> = -\frac{i\hbar}{2m}\int\left(\Psi_R^* \frac{\partial \Psi_L}{\partial x} - \frac{\partial \Psi_R^*}{\partial x}\Psi_L\right)d\vec{s} \tag{2.6}$$

where the integration is performed over a surface contained within the barrier region. Calculation of the tunnel current becomes a process of choosing the appropriate wavefunctions. Equation 2.5 and the expression for the matrix element act as a starting point for a wide variety of tunneling problems.

Although similar to first order perturbation theory, formally the transfer Hamiltonian technique is quite different. Unlike the traditional theory, in the tunneling problem Ψ_L and Ψ_R are solutions of two independent Hamiltonians. Despite this difference the validity of using first order perturbation techniques to evaluate the tunnel current has been verified by Kane (1969).

3 Inelastic Electron Tunneling Spectroscopy.

The technique of inelastic electron tunneling was first developed by Jaklevic and Lambe (1966) who studied the tunneling characteristics of a number of metal insulator metal tunnel junctions. Jaklevic and Lambe observed that while the majority of tunneling electrons traverse the barrier elastically, a small amount transfer some of their energy to vibrational modes within the barrier region. The transfer of energy acts as an additional tunneling channel, and introduces structure into the tunneling characteristic. Peaks in d^2I/dV^2 as a function of voltage are observed at energies $eV = \hbar\omega$ corresponding to the energies of the vibrational mode excited (Fig. 3.1). By incorporating molecules into the barrier region of a junction, IETS can be used as a form of vibrational spectroscopy, providing information similar to Raman and infrared techniques.

This part of the thesis describes a series of IETS experiments performed on a number of undoped Mg-MgO-metal tunnel junctions. The d^2I/dV^2 spectra, and the elastic tunneling characteristics, have been used to investigate the effects of different preparation conditions, and the choice of cover electrode on the resultant tunnel junction.

It is important to study the properities of undoped junctions since the oxide provides the active surface for chemisorbed molecules which are studied by IETS. The spectra of Mg based tunnel junctions has been found to vary a great deal between different laboratories (Adler, 1969; Klein et al., 1973; Walmsley et al., 1980; Plesiewicz and Adler, 1986). Some of this variation has been attributed to the influence of moisture during junction fabrication (Plesiewicz and Adler, 1986). To better understand this variation, including the role of moisture, Mg junctions were

FIGURE 3.1 Schematic illustrasting the two possible tunneling mechanisms: elastic tunneling (a), inelastic tunneling (b). At voltages $|V| \geq \hbar\omega/e$, the tunneling electron may lose energy to a vibrational mode of frequency ω. The additional tunneling channel produces a kink in the I-V characteristics, a step in dI/dV, and a peak in d^2IdV^2.

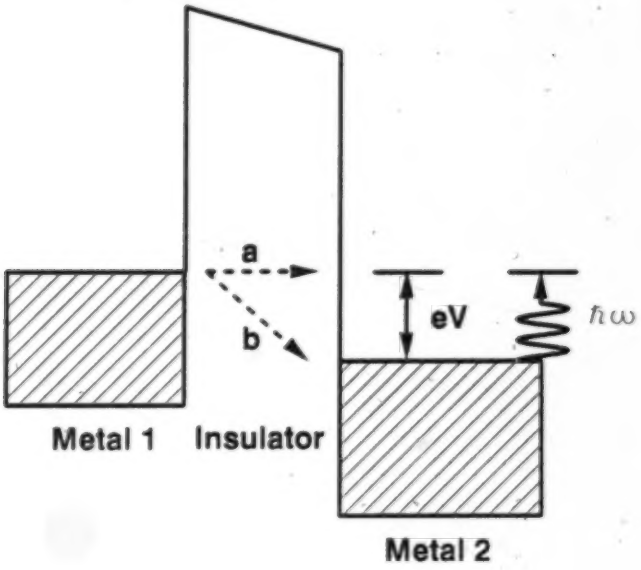
a
b
eV
ħω
Metal 1
Insulator
Metal 2

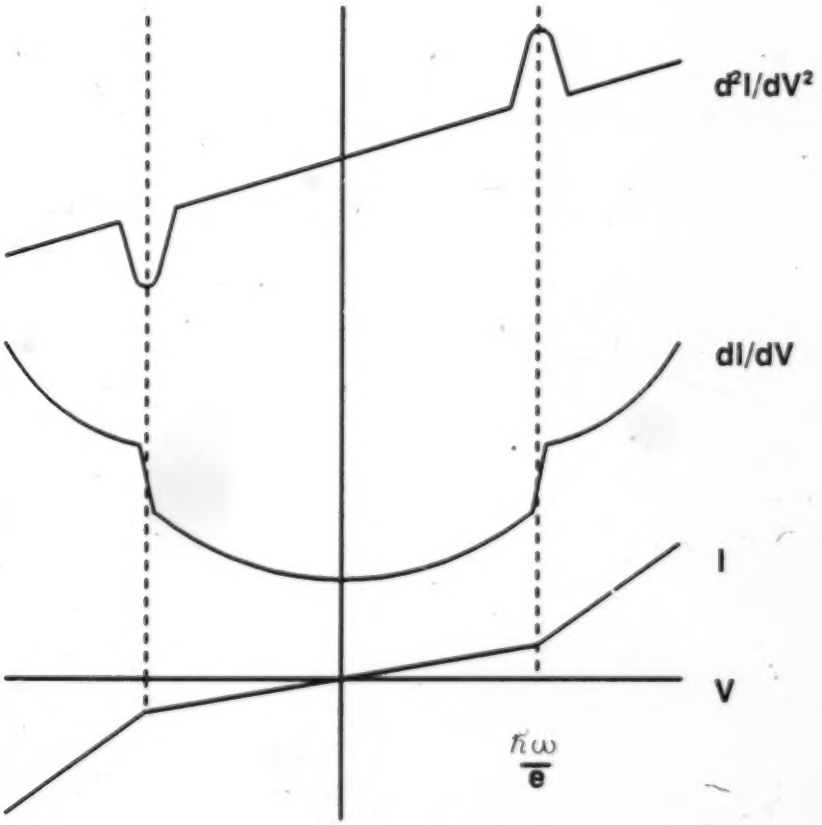
d²I/dV²
dI/dV
I
V
ħω
e

prepared using a variety of different preparation conditions, and with a number of cover electrodes. It is found that the variation can be ascribed to the nature of the oxide layer, and how different preparation conditions can influence Mg oxidation.

To better understand the technique of IETS, the theoretical aspects of tunneling in metal insulator metal junctions are discussed. By obtaining an expression for the tunnel current, it is demonstrated how the experimental current voltage characteristics can be used to provide information about the tunnel barrier.

The inelastic tunneling mechanism which provides the interaction between electron and molecule, and the resultant effect on the tunneling characteristics is also dicussed.

The experimental techniques to measure and extract information from the tunneling curves is introduced, and the result of the experiments performed on Mg junctions is presented.

3.1 Theory of Elastic Tunneling

The majority of electrons which tunnel in a junction do not excite vibrational modes and traverse the barrier with no loss of energy. Elastic tunneling between normal metals separated by a tunnel barrier (Fig. 3.2) was discussed by Harrison (1961).

Using Bardeen's formalism as a starting point, Harrison considered tunneling from a independent particle point of view. By using the appropriate boundary conditions, and by making a WKB approximation (Liboff, 1980) at the barrier interface he obtained expressions for the electron wavefunctions in each electrode. The wavefunction in electrode L was expressed as

$$\Psi_L = C_L(k_x)^{-1/2}\cos\left(\int_x^0 k_x dx + \gamma_L\right) \qquad x<0$$

$$= \frac{1}{2}C_L(k_x)^{-1/2}\exp\left(-\int_0^x |k_x| dx\right) \qquad x>0 \qquad (3.1)$$

where the barrier extends from x=0 to x=s. A corresponding wavefunction was constructed to describe the electron in electrode R. The wavefunctions are consistent with the Bardeen picture since they oscillate periodically in the metal electrode, and decay to zero inside the barrier.

By substituting the two wavefunctions into Bardeen's expression for the tunneling matrix element, Harrison finds

$$|\langle \Psi_R | H^T | \Psi_L \rangle|^2 = \left(\frac{\hbar^2}{2m}\right)\frac{k_{xL}k_{xR}}{L_L L_R}\exp\left(-2\int_0^s |k_x| dx\right) \qquad (3.2)$$

where L_i are the thicknesses of the metal electrodes. For independent particles

$$k_{xi} = \left(\frac{m}{\hbar^2}\right)\frac{L_i}{\pi\rho_i} \qquad (3.3)$$

FIGURE 3.2 The energy level diagram of a metal-insulator-metal tunnel junction with and without applied bias. The trapezoidal tunnel barrier $\phi(x, V)$ is described by barrier heights ϕ_1, and ϕ_2 of metal 1 and 2 respectively, the thickness s, and the voltage V. E_{f1} and E_{f2} are the Fermi levels of the two metals.

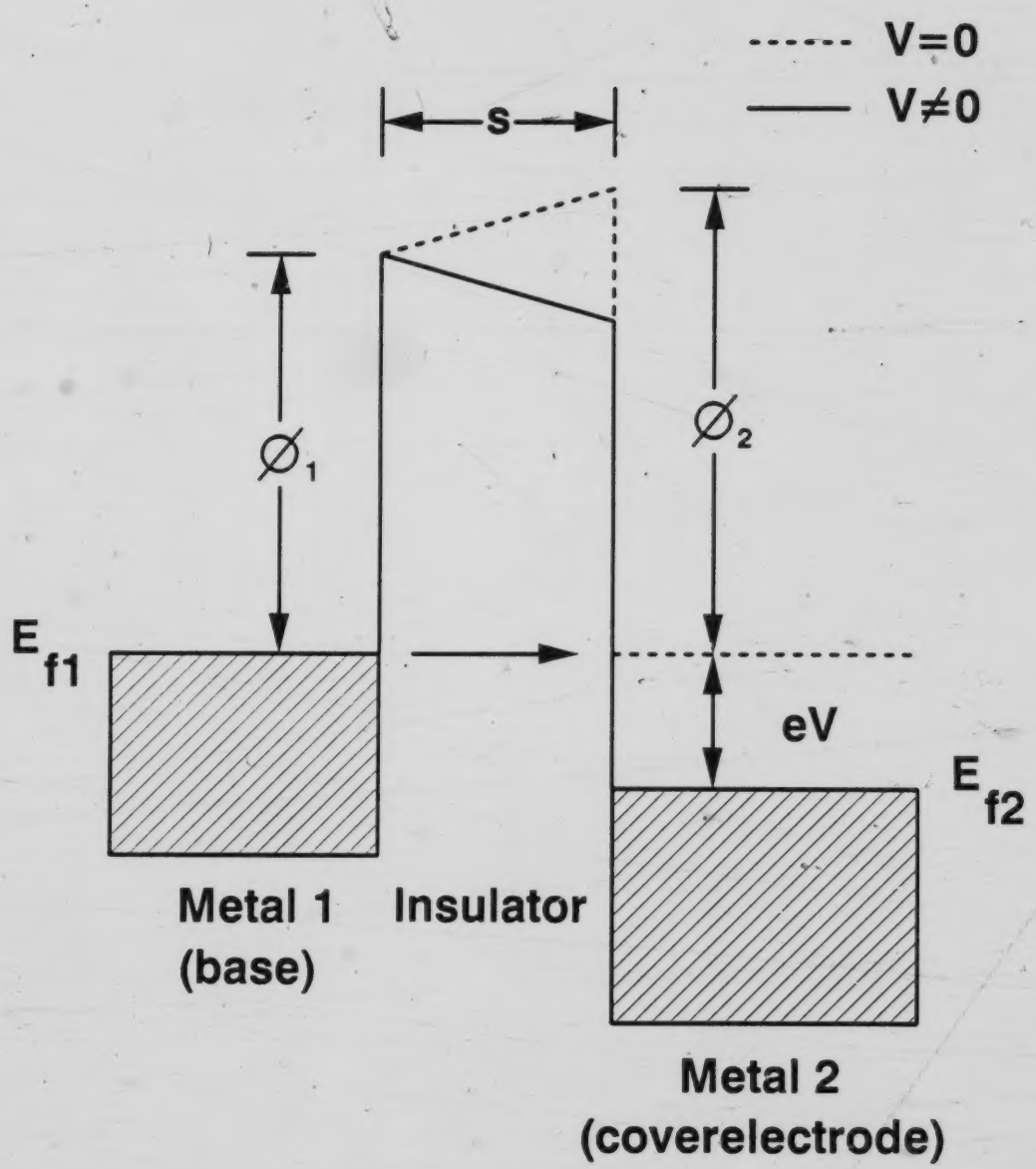
V=0
V≠0
s
$\varnothing_1$
$\varnothing_2$
E_{f1}
eV
E_{f2}
Metal 1
(base)
Insulator
Metal 2
(coverelectrode)

and the expression for the tunnel current can be written as

$$j = \frac{2e}{h} \sum_{k_t} \int_{-\infty}^{\infty} \exp\left(-2 \int_0^s |k_x| dx \right) (f(E) - f(E + eV)) dE_x \tag{3.4}$$

The key feature of Harrison's treatment is that additional density of states terms which appear in the denominator of the matrix element, cancel the original terms. This means the tunnel current is independent of the density of states of the metal electrodes. The result is in contrast to superconducting tunneling experiments, where the superconducting density of states are clearly observed (Giaever,1960a, 1960b). The discrepancy may be attributed to the single particle approximation made in Harrison's derivation, yet it seems strange that such a clear experimental result would depend on such a subtle aspect of the many particle system. The WKB approximation is only valid in regions where the fractional change in the electron wavelength is small. This is not true at a band edge, or energy gap where the kinetic energy is small, and this may introduce observable structure into the tunnel current. The apparent contradiction may be understood if it is assumed that the density of states terms in the matrix element are sensitive only to the normal metal states, while the additional terms outside the matrix element probe quasiparticle states.

The sum over $k_{||}$ in the expression for the tunnel current may be replaced by an integral in energy over projections of a constant energy surface onto the plane of the barrier, in other words replace

$$\sum_{k_t} \rightarrow \int_0^{\infty} \frac{2\pi m}{h^2} dE_{||} \tag{3.5}$$

The modified expression for the tunnel current then becomes

$$j = \frac{4\pi me}{h^3}\int_0^{\infty} dE_{||}\int_0^{E_m} \exp\left(-2\int_0^{s}|k_x|dx\right)(f(E)-f(E-eV))dE_x \tag{3.6}$$

where $E_m = E - E_{||}$, is the maximum possible energy normal to the barrier.

Within the barrier region the wavevector k_x may be expressed as

$$k_x(E_x) = \frac{1}{\hbar}(2m(\phi(x,V)-E_x))^{\frac{1}{2}} \tag{3.7}$$

Where $\phi(x,V)$ is the potential barrier (Fig 3.2). Substituting this form into the tunnel current the resultant expression may be written in the form

$$j = \frac{4\pi me}{h^3}\int_0^{\infty} dE_{||}\int_0^{E_m} D(E_x)(f(E)-f(E+eV))dE_x \tag{3.8}$$

where $D(E_x)$ is defined as the barrier transmission coefficient, or

$$D(E_x) = \exp\left(-\frac{2}{h}\int_0^{s}\{2m(\phi(x,V)-E_x)\}^{1/2}dx\right) \tag{3.9}$$

To simplify the expression further Harrison defined the following integrals,

$$\xi_L = \frac{4\pi me}{h^3}\int_0^{\infty} f(E)dE_{||}$$

$$\xi_R = \frac{4\pi me}{h^3}\int_0^{\infty} f(E+eV)dE_{||} \tag{3.10}$$

and

$$\xi = \xi_L - \xi_R$$

Most tunneling spectroscopy, including IETS, is performed at 4.2 K. At this temperature the Fermi functions can be approximated by their zero temperature form. This simplifies the integrals and the result is

$$\xi_1 = \frac{4\pi me}{h^3}(E_F - E_x) \qquad E_x < E_F$$

$$= 0 \qquad E_x > E_F$$

$$\xi_1 = \frac{4\pi me}{h^3}(E_F - E_x - eV) \qquad E_x < E_F$$

$$= 0 \qquad E_x > E_F$$

Therefore

$$\xi = \left(\frac{4\pi me}{h^3}\right)eV \qquad 0 < E_x < E_F - eV$$

$$= \left(\frac{4\pi me}{h^3}\right)(E_F - E_x) \qquad E_F - eV < E_x < E_F \tag{3.11}$$

$$= 0 \qquad E_F < E_x$$

Substituting the results into the expression for the tunnel current one obtains

$$j = \frac{4\pi me}{h^3}\left\{eV\int_0^{E_F - eV} D(E_x)dE_x + \int_{E_F - eV}^{E_F}(E_F - E_x)D(E_x)dE_x\right\} \tag{3.12}$$

To allow analytical solution of the integrals Simmons (1963a, 1963b) found it necessary to replace the tunnel barrier $\phi(x, V)$ by an average barrier $\bar{\phi}(V)$. The problem with this approach is that any asymmetry in the characteristics resulting from the shape of the tunnel barrier is lost. In practice symmetric tunneling characteristics are seldom observed and indicate the importance of the barrier shape.

Realistic treatment of the barrier shape requires numerical evaluation of the tunneling integrals. By choosing a reasonable shape for the barrier as an initial guess, an iteration process can be used to fit experimental curves to the appropriate barrier.

To eliminate the need for numerical analysis, Brinkman, Dynes, and Rowell (BDR) (1970) observed that although the tunneling characteristics of many tunnel junctions are predominantly ohmic, the tunnel conductance dI/dV, has a appreciable parabolic component. Using a trapezoidal barrier (Fig. 3.2) of the form

$$\phi(x,V) = \phi_1 + (x/s)(\phi_2 - eV - \phi_1) \tag{3.13}$$

BDR inserted this into the expression for the tunnel current. Although the expression could not be solved analytically they obtained a series expansion for the current in powers of voltage. By differentiating this expression with respect to voltage they obtained an expression for the linear and quadratic terms of dI/dV.

$$\frac{\sigma(V)}{\sigma(0)} = 1 - \left(\frac{A\Delta\phi}{16\bar{\phi}^{3/2}}\right)eV + \left(\frac{9A^2}{128\bar{\phi}}\right)(eV)^2 \tag{3.14}$$

where

$$A = \frac{4\pi(2m)^{1/2}s}{3h}$$

$$\Delta\phi = \phi_2 - \phi_1$$

$$\bar{\phi} = \left(\frac{\phi_1 + \phi_2}{2}\right)$$

and

$$\sigma(0) = \frac{3.16x10^{10}\bar{\phi}^{1/2}}{s}\exp(-1.025s\bar{\phi}^{1/2})$$

where s is measured in Å and the barrier heights in volts. BDR compared these curves with exact calculations obtained numerically and found the parabolic expression agrees within 5 per cent below 200 meV. The BDR expression provides a convenient method of extracting values for ϕ_1, ϕ_2 and s for the tunnel barrier, from experimental conductance curves.

3.2 Inelastic Tunneling Theory

Despite the fact that the majority of tunneling electrons traverse the barrier with no loss in energy, experimentally it is observed that a small amount can interact with the barrier and lose energy. Jaklevic and Lambe (1966) found that electrons can transfer energy to vibrational modes of molecules in the barrier region. The interaction has the effect of opening up a new channel for tunneling, and produces a kink in the tunnel current at a voltage $V = \hbar\omega / e$, where $\hbar\omega$ is the energy of vibration. In practice, the change in slope at the kink is less than 1 % and so very hard to see. For this reason IETS experiments measure d^2I/dV^2 verses voltage where the new channel creates a peak in the characteristics (Fig. 3.1).

In general, molecules have a number of vibrational modes, and various molecules can exist within the barrier, so a d^2I/dV^2 curve for a typical tunnel junction exhibits a series of peaks. The vibrational energies of most molecules is less than 500 meV, so most d^2I/dV^2, or IETS spectra are measured over a voltage range of ±500 mV. The peaks in the IETS spectra can be related to infrared and, or Raman peaks obtained on the same molecule.

Using radioactive molecules Langen and Hansma (1975) found that IETS is sensitive to as little as one third of a monolayer of molecules at the barrier with the ultimate sensitivity determined by the sensitivity of the instrument and the patience of the experimenter. The energy resolution of IETS is limited by the line width of the peaks. The intrinsic linewidth of vibrational modes is typically about 1 meV, however both thermal and modulation voltage broadening contribute additional width to the peaks.

Thermal broadening results from the temperature smearing of the Fermi functions, which describe the energy distribution of the tunneling electrons. Lambe and Jaklevic (1966) found that this smearing contributes an additional width to the IETS peak of $5.4k_BT/e$. At 77 K this leads to a peak width of 36 meV, while at 4.2 K the width is reduced to 2 meV. The use of superconducting electrodes can reduce thermal broadening somewhat, since the energy distribution of tunneling electrons is less affected by smearing in a superconductor. To reduce these thermal effects IETS experiments are performed at 4.2 K where broadening is minimal.

Modulation voltage broadening occurs as a result of the modulation voltage signal which is applied to the junction to obtain the second derivative signal. The effect of modulation broadening was discussed by Klein et al. (1983), who found that by applying a modulation voltage $V_\omega \cos \omega t$, the inelastic peak will broaden by an amount ~$1.2V_\omega$. At 4.2 K modulation broadening will dominate for $V_\omega > 3$ mV.

In addition to both thermal and modulation broadening, the ultimate resolution of IETS will also depend on instrumental factors such as sweep speed and averaging times. Taking all these variables into account typical resolution in IETS experiments is between 1 and 4 meV.

Treatment of the peak intensities in IETS requires a dicussion of the electron molecule interaction. The first theoretical treatment of this interaction was presented by Scalapino and Marcus (1967) who suggested that there exists a Coulomb interaction between the tunneling electron and the component of the dipole moment of the molecule normal to the metal surface. The interaction potential between an electron located a perpendicular distance x inside the barrier, passing a perpendicular distance r from the dipole may be expressed as

$$\phi_{int} = \frac{2ep_x x}{(x^2 + r^2)^{3/2}} \tag{3.15}$$

where p_x is the dipole moment operator for the normal component of the dipole moment. The factor of two in the expression arises from a doubling from the contribution of the image dipole, and the image makes contribution from the parallel component negligible.

To calculate the inelastic contribution to the current, Scalapino and Marcus treated ϕ_{int} as a perturbation to the barrier potential $\phi(x)$. By assuming a rectangular barrier (i.e. $\phi(x) = \phi$ for $0<x<s$ and zero elsewhere), and by neglecting the energy lost during tunneling, Harrison's barrier transmission coefficient could be modified to become

$$D(E_x) = \exp\left(-\frac{2}{\hbar}\int_0^s \{2m(\phi_{int} + \phi - E_x)\}^{1/2} dx\right) \tag{3.16}$$

To find the lowest order effect of ϕ_{int} on the tunnel current, $\phi(x) - E_x$ was replaced by Φ and the transmission coefficient expanded in powers of ϕ_{int}/Φ. The result was

$$D(E_x) \propto \exp\left\{-\left(\frac{8m\Phi}{\hbar^2}\right)^{1/2} s\right\}\left[1 + \left(\frac{2m}{\Phi}\right)^{1/2} \frac{ep_x}{hs} g\left(\frac{r}{s}\right)\right]^2 \tag{3.17}$$

where

$$g(x) = \frac{1}{x} - \frac{1}{(1+x^2)^{1/2}}$$

For inelastic tunneling, the relevant term in $D(E_x)$ is the second one in square brackets. In general the dipole moment operator should be summed over all initial

and final states of the molecule, however at the low temperatures at which the experiments are performed, it is only necessary to consider transitions between the ground state $|0>$ and the first excited state $<1|$. The quantity of interest for direct comparison with experiment is the ratio between the conductances due to inelastic, and elastic tunneling. Using Harrison's (1961) independent particle approximation and assuming specular reflection for the inelastic processes Scalapino and Marcus found that

$$\frac{dI_i(r)/dV}{dI_e(r)/dV} = \frac{2m}{\Phi}\left(\frac{e^2}{\hbar s}\right)|<1|p_x|0>|^2 g\left(\frac{r}{s}\right)\theta\left(V - \frac{\hbar\omega_1}{e}\right) \tag{3.18}$$

where the step function $\theta(x)$ indicates the channel is not available for tunneling unless $V > \hbar\omega_1/e$. To obtain the total inelastic current due to the vibrational mode of one impurity the expression must be integrated over all r. To include all impurities the expression is then multiplied by the number of impurities per unit area N, and summed over all possible vibrational modes. The result is

$$\frac{dI_i(r)/dV}{dI_e(r)/dV} = N\frac{4\pi m e^2}{\Phi\hbar^2}\ln\left|\frac{s}{r_0}\right|\sum_m |<m|p_x|0>|^2\theta\left(V - \frac{\hbar\omega_m}{e}\right) \tag{3.19}$$

The integration over r introduces a cut off r_0. This cut off precludes any quantitative comparison with experiment. If resonable barrier parameters are inserted into the expression, and a cut off of r_0=s/30, or approximately 1 Å is used (Scalapino and Marcus, 1967), an increase of about 1 % is found in reasonable agreement with experiment.

The final expression indicates that the increase in conductance is proportional to $|\langle m|p_x|0\rangle|^2$. This is the same quantity which determines intensities in infrared absorption spectra. In general, it is observed that large IR peaks do prc luce large tunneling peaks.

The Scalapino and Marcus theory assumes that the cross section is independent of coverage, yet experimentally (Langan and Hansma, 1975) it is observed that the peak intensity increases more rapidly than the coverage. To explain the dicrepency Cederberg (1981) suggested that electrons are more likely to tunnel where there are no molecules. As the concentration of molecules is increased the elastic current decreases rapidly, therefore the ratio of the conductance step increases.

In order for the tunneling electron to produce a peak in the IETS spectra, the Scalapino and Marcus theory requires that there be a net dipole moment normal to the electrode surface. In practice many spectra exhibit peaks which do not meet this criterion. To explain this fact Lambe and Jaklevic (1968) generalized the Scalapino and Marcus theory to consider the polarizability of bonds within a molecule. In this model the tunneling electron induces a dipole moment in the molecule, and in turn interacts with it. The interaction potential for this model may be written as

$$\phi_i^R = -\frac{4e^2\alpha x^2}{(x^2+r^2)^3} \tag{3.20}$$

where α is the polarizbility of the molecule and the R signifies Raman, since modes with a polarizability are observed in Raman spectroscopy. As in Scalapino and Marcus theory the transmission coefficient may be written as

$$D(E_x)\propto\exp\left\{-\left(\frac{8m\Phi}{h^2}\right)^{1/2}s\right\}\left[1+\left(\frac{2m}{\Phi}\right)^{1/2}\frac{\alpha e^2}{4hs^3}t\left(\frac{r}{s}\right)\right]^2 \tag{3.21}$$

where t(x) is a function of the form

$$t(x)=\frac{1}{x^2}\left[\frac{1-x^2}{(1+x^2)^2}+\frac{1}{x}\tan^{-1}\left(\frac{1}{x}\right)\right]$$

and the resultant conductance jump is

$$\frac{dI_i/dV}{dI_e/dV}=N\left(\frac{4\pi me^2}{\Phi h^2}\right)\left(\frac{e^2}{16s^6}\right) \times\int_{r_0}^{s}t^2\left(\frac{r}{s}\right)r^2dr\sum_m|<m|\alpha|0>|^2\theta\left(V-\frac{\hbar\omega_m}{e}\right) \tag{3.22}$$

t(x) must be evaluated numerically and depends to a large part on the cut off r_0. Estimates of the conductance jump using reasonable values for the parameters indicate a jump of between 0.1 and 0.5 % (Lambe and Jaklevic, 1968).

The analysis of both Scalapino and Marcus (1967), and Lambe and Jaklevic (1968) indicated that IETS should be sensitive to both IR and Raman active modes. Both theories work well to within an order of magnitude but they do have their problems. Both theories assume specular reflection, and the energy loss during tunneling is neglected. Also the cut off r_0 makes quantitative prediction of intensities difficult.

With hopes of solving some of these drawbacks, Kirtley, Scalapino and Hansma (KSH) (1976) developed a three dimensional theory based on the transfer Hamiltonian methods of Bardeen (1961). Unlike the Bardeen treatment of elastic tunneling, in KSH theory, the matrix element includes the interaction potential between the tunneling electron and the molecule.

KSH assume that the charge distribution within the molecule can be split up and described by partial charges located on each atom. In this way the electron-molecule potential is considered as a sum of Coulomb potentials between the electron and each partial charge.

$$\phi_{int}(\vec{r}) = \sum_j \frac{-e^2 Z_j}{|\vec{r} - \vec{R}_j|} \tag{3.23}$$

where eZ_j and R_j are the partial charge and the location of the jth atom in the molecule respectively. The advantage of the partial charge approach is that it is still valid at distances within which the dipole appoximation breaks down.

The quantity of interest in inelastic tunneling is the part of $\phi_{int}(\vec{r})$ which connects initial and final states of energies which differ by an amount equal to the energy of vibration of the excitation. KSH seperated out the component of the interaction potential which oscillates at the frequency of the vibrational mode of interest. The atomic displacements can be written in the form $\vec{R}_j = \vec{R}_j(0) + \delta\vec{R}_j$ where $\delta\vec{R}_j$ oscillates at the desired frequency. The interaction potential may then be expressed in the form

$$\phi_{int}(\vec{r}) = \sum_j -e^2 Z_j \delta\vec{R}_j \cdot \vec{\nabla}_j \left(\frac{1}{|\vec{r} - \vec{R}_j(0)|} \right) \tag{3.24}$$

The inclusion of the image potential in both electrodes complicates this expression somewhat.

As with Bardeen's treatment of elastic tunneling, calculation of the inelastic current requires evaluation of the matrix element. In KSH the expression takes the form

$$<\Psi_R|H^T|\Psi_L> = \int_0^s d^3x\, \Psi_R^* \phi_{int}(\vec{r},\omega t)\ \Psi_L \tag{3.25}$$

where Ψ_R and Ψ_L are the same wavefunctions as used in elastic theory (equation 3.1). The inelastic tunnel current then takes the form

$$j = \frac{4\pi e}{\hbar}\sum_{L,R}|<\Psi_R|H^T|\Psi_L>|^2 \tag{3.26}$$
$$\times f(E_L)[1-f(E_R+eV+\hbar\omega)]\delta(E_L-E_R-\hbar\omega)$$

where now the conservation of energy condition includes the excitation of a vibrational mode. In general the matrix elements are very hard to evaluate, since they are a function of both the incoming and outgoing energies and directions. If the direction of the incoming and outgoing electrons are expressed in spherical coordinates the final result of KSH theory becomes

$$\frac{d^2j}{d(eV)^2} = \frac{8\pi ne}{\hbar}\left(\frac{L}{\pi}\right)^6\left(\frac{m}{\hbar^2}\right)^3 (E_{FL})^{1/2}(E_{FR}-eV)^{1/2} \tag{3.27}$$
$$\times \int_0^{2\pi} d\phi_L \int_0^{2\pi} d\phi_R \int_0^1 d(\cos\theta_L)\int_0^1 d(\cos\theta_R)$$
$$\times |<\Psi_R|H^T|\Psi_L>|^2\ \ \delta(\hbar\omega-eV)$$

where n is the surface density of molecules, and L is a normalization length for the inital wavefunction. In most cases, the integrations over incoming and outgoing angles must be performed numerically. By using values appropriate for a monolayer of hydroxyl ions oriented normal to the metal surface KSH calculated a change in conductance of 0.5 %, compared with experimental values of 0.4%.

The theory of KSH predicts that both infrared-active and Raman active modes should be observable without the introduction of molecular polarizabilities. KSH find that modes with dipole moments oriented normal to the electodes have larger intensities when located close to either metal in agreement wih Scalapino and Marcus, however within the barrier dipoles oriented parallel have larger cross sections. The reason is that energy loss, and off axis scattering allow destructive interference between individual scattering dipoles, and the dipole potential of dipoles oriented normal to the electrodes tends to integrate to zero at the center of the barrier.

KSH theory also reproduces the experimentally observed bias dependence of the IETS peak intensities, and indicates that the interaction distance is of the same order of magnitude as the barrier thickness.

To better predict the intensities of complex molecules, Kirtley and Hall (1980) replaced the atom by atom sum by a sum over symmetry coordinates. This allows for a better comparison with comparible infrared data. Using infrared data as a starting point, and by adjusting parameters in the theory until the relative peak intensities agreed with experiment, Kirtley and Hall where able to obtain the molecular orientation of $CH_3SO_3^-$ on alumina. In this way the KSH theory can use relative intensity information to infer molecular orientation.

3.3 Measurement of Tunneling Characteristics

The measurment of the tunneling characteristics $\sigma = dI/dV$, and $d\sigma/dV$ is made using a combination of both harmonic detection and bridge techniques (Adler and Jackson 1966; Adler 1982). The system is suitibly interfaced to an on-line minicomputer allowing for control of the experiment, storage of calibrated data, and subsequent data analysis.

3.3.1 Modulation Spectroscopy.

Modulation spectroscopy is a technique used to study nonlinear devices. The technique consists of modulating one variable and studying the response of the sample to this signal. For example, consider the I-V response of a nonlinear device (Adler, 1982). By modulating the current with a sinusoidal signal, the output will depend on the I-V characteristics of the device as shown in Fig. 3.3. Using a modulation current of $\delta \cos \omega t$ about the d.c. value I_0, by Taylor expansion the response will be

$$V(I) = V(I_o) + \left(\frac{dV}{dI}\right)_{I_o} \delta \cos\omega t + \frac{1}{2}\left(\frac{d^2V}{dI^2}\right)_{I_o} \delta^2 \cos^2 \omega t + \ldots \tag{3.28}$$

or,

$$V(I) = V(I_o) + \left(\frac{dV}{dI}\right)_{I_o} \delta \cos\omega t + \frac{1}{4}\left(\frac{d^2V}{dI^2}\right)_{I_o} \delta^2 (1 + \cos 2\omega t) + \ldots$$

where $V(I_O)$ is the D.C. bias across the device. If the device is only slightly nonlinear (for instance tunnel junctions), then the higher order terms may be neglected. Synchronous detection of both the ω and 2ω components yields outputs proportional to dV/dI and d^2V/dI^2 respectively.

FIGURE 3.3 Applying a modulation current $\delta\cos\omega t$ to a nonlinear device results in a waveform with components proportional to dV/dI and d^2V/dI^2.

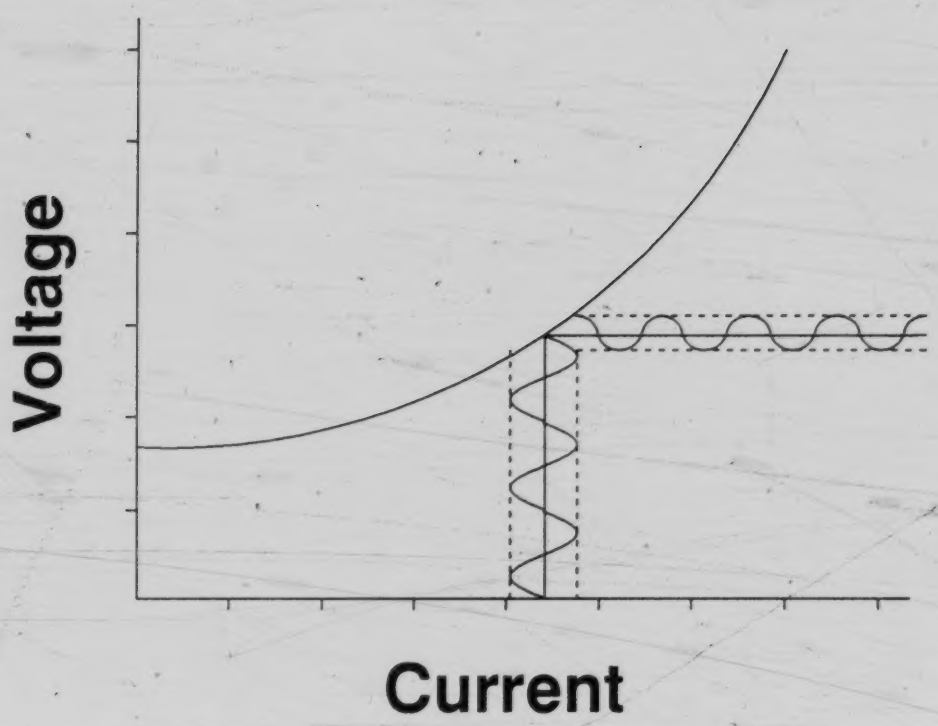
Voltage
Current

3.3.2 Data Collection

In tunneling spectroscopy, the quantities of interest are $\sigma = dI/dV$ and $d\sigma/dV$. Direct measurement of these variables would require a constant voltage load line which in practice is hard to achieve. With high impedence circuitry it much easier to obtain a constant current load line, and for this reason dV/dI and d^2V/dI^2 are measured then converted to the desired quantities in the appropriate manner (Adler, 1982).

$$\sigma = \left(\frac{1}{dV/dI} \right) \tag{3.29}$$

and,

$$\left(\frac{d\sigma}{dV} \right) = -\sigma^3 \left(\frac{d^2V}{dI^2} \right) \tag{3.30}$$

The measuring circuit for the experiment is basically an A.C. Wheatstone bridge (Adler and Jackson, 1986; Adler, 1982). The junction is placed in one arm of the bridge, while a variable resistor is placed in the opposite arm. A small modulation current is passed through the bridge (Fig. 3.4). When the bridge is correctly balanced, the potential difference V_{12} between the resistor and the junction is zero. Since the tunnel junction is a nonlinear device, when a d.c. voltage is applied across the junction, the potential difference between the two becomes non zero. In general the voltage across the junction is given by,

$$V(I) = V(I_o) + \left(\frac{dV}{dI} \right)_{I_o} \delta \cos \omega t + \frac{1}{4} \left(\frac{d^2V}{dI^2} \right)_{I_o} \delta^2 (1 + \cos 2\omega t) \tag{3.31}$$

and the voltage across the resistor is,

FIGURE 3.4 Schematic of the A.C. Wheatstone bridge used to measure the tunneling characteristics of the tunnel junctions.

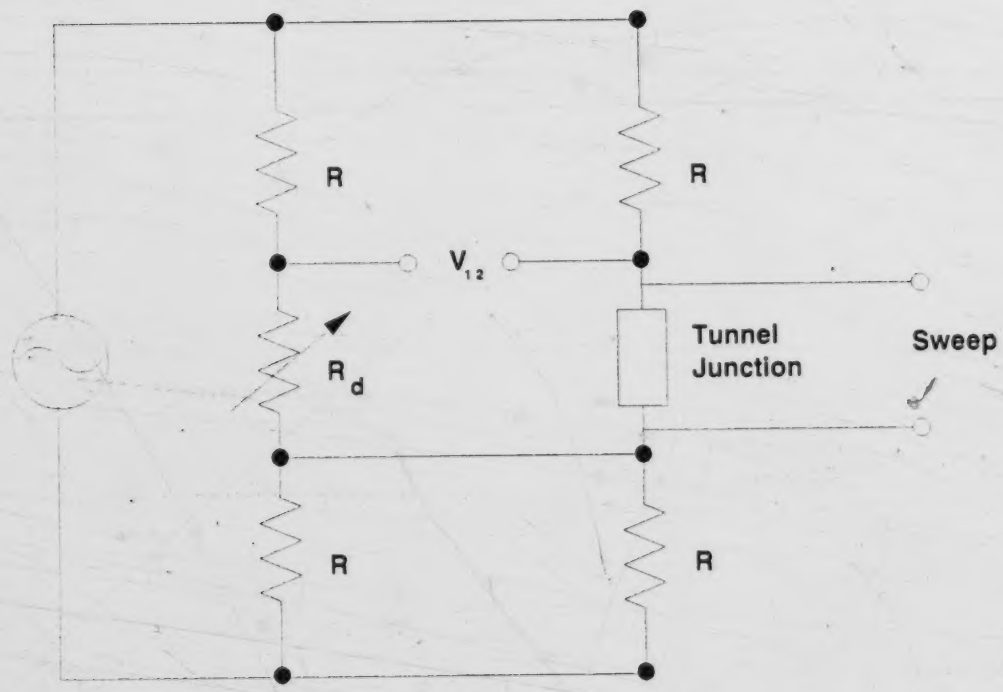
R
R
V_{12}
R_d
Tunnel
Junction
Sweep
R
R

$$V_d = \delta \cos \omega t \, (R_d) \tag{3.32}$$

The potential difference between the two may be expressed as,

$$V_{12} = V(I_o) + \delta \cos \omega t \left(\left(\frac{dV}{dI} \right)_{I_o} - R_d \right) + \delta^2 \cos 2\omega t \left(\frac{1}{4} \right) \left(\frac{d^2V}{dI^2} \right)_{I_o} \tag{3.33}$$

The ω and the 2ω components are phase sensitively detected using lock-in amplifiers. The output of the σ lock-in (Y_ω) is proportional to the departure of the dynamic resistance from R_d, and $Y_{2\omega}$ is directly proportional to (d^2V/dI^2).

3.3.3 Calibration.

To convert Y_ω and $Y_{2\omega}$ to σ and $d\sigma/dV$ the measurements must be calibrated. The process consists of substituting a resistance box for the junction and varying the resistance over the range of interest (Adler, 1982).

The first step is to place the junction into the circuit and to adjust the lock-ins so that most of their dynamic range is utilized. Next the junction is replaced by a resistance box and the resistance is adjusted over the dynamic range of the Y_ω lock-in. A least squares fit of the response to the resistor is made

$$Y_\omega = \sum_{n=0}^{N} c_n R_{cal}^n \tag{3.35}$$

In general a linear fit is sufficient, however a quadratic fit may be used. To obtain calibrated σ values, the Y_ω data is converted to dV/dI using the calibration equation and then taking the reciprocal to obtain σ.

To obtain the component of $Y_{2\omega}$ due to the junction, the portion of the signal associated with harmonic distortion ($Y^0_{2\omega}$) must be subtracted. The amount of

distortion depends on the size of the resistance. Since resistors are linear devices, any $Y_{2\omega}$ signal obtained during calibration can be attributed to harmonic distortion. This output is used to construct a curve representitive of the distortion component.

$$Y^{o}_{2\omega} = \sum_{n=0}^{N} \alpha_n R^n_{cal} \tag{3.36}$$

In this way the output of $Y_{2\omega}$ may be related to dσ/dV by,

$$\frac{d\sigma}{dV} = \eta_m(V)\sigma^3(V)\{Y_{2\omega}(V) - Y^{o}_{2\omega}\} \tag{3.37}$$

The calibration constant $\eta_m(V)$ is a Chebyshev polynomial of order m. The polynomial is found by integrating this expression, and obtaining a least squares fit with the calibrated σ data.

The measurements are made at 4.2 K to minimize thermal broadening. The sample is immersed into a storage dewer containing liquid He^4. The data is recorded in the voltage range ±500 mV with a modulation of between 3 to 5 mV. The polarities are measured with respect to the Mg base electrode. To allow direct comparison between dσ/dV spectra of different junctions, the data are presented in a normalized 1/σ dσ/dV form, which takes into account differences in junction resistance.

3.4 Data Analysis

In this chapter we dicuss the various methods of extracting information such as peak identification, peak intensity, and determination of barrier parameters from the tunneling data.

3.4.1 Peak identification

Figure 3.5 shows a typical IET spectra of a Mg-MgO-Pb plasma junction. To assign each peak in the spectra with a particular vibrational mode requires combined information from a variety of sources. Previous tunneling experiments are used, and comparison with peaks seen in Raman, infrared (IR), and neutron scattering experiments. The energy of the peaks may also be compared with theoretical predictions. Any comparisons are made with the conditions under which the junctions were fabricated in mind.

The phonons of most metals occur at energies of between about 0 to 40 meV since their atomic masses are quite large and metallic bonds are weak. Vibrations of the insulator can be expected to occur at higher energies (0-90 meV) because the bonds are stronger, like MgO, which is an ionic solid. The vibrational modes of molecular impurities tend to be at higher energies since most of the impurities contain hydrogen, which is both light and bonds strongly.

As an example of the peak assignment procedure, let us analyse the spectrum of Figure 3.5 and try and identify the peaks. Undoped MgO based junctions have been studied by a number of authors (Adler, 1969; Klein et al., 1973; Walmsley et al., 1980; Plesiewicz and Adler, 1986), and it is found that the nature of the spectra varies

FIGURE 3.5 The IET spectra of an undoped Mg-MgO-Pb plasma junction.

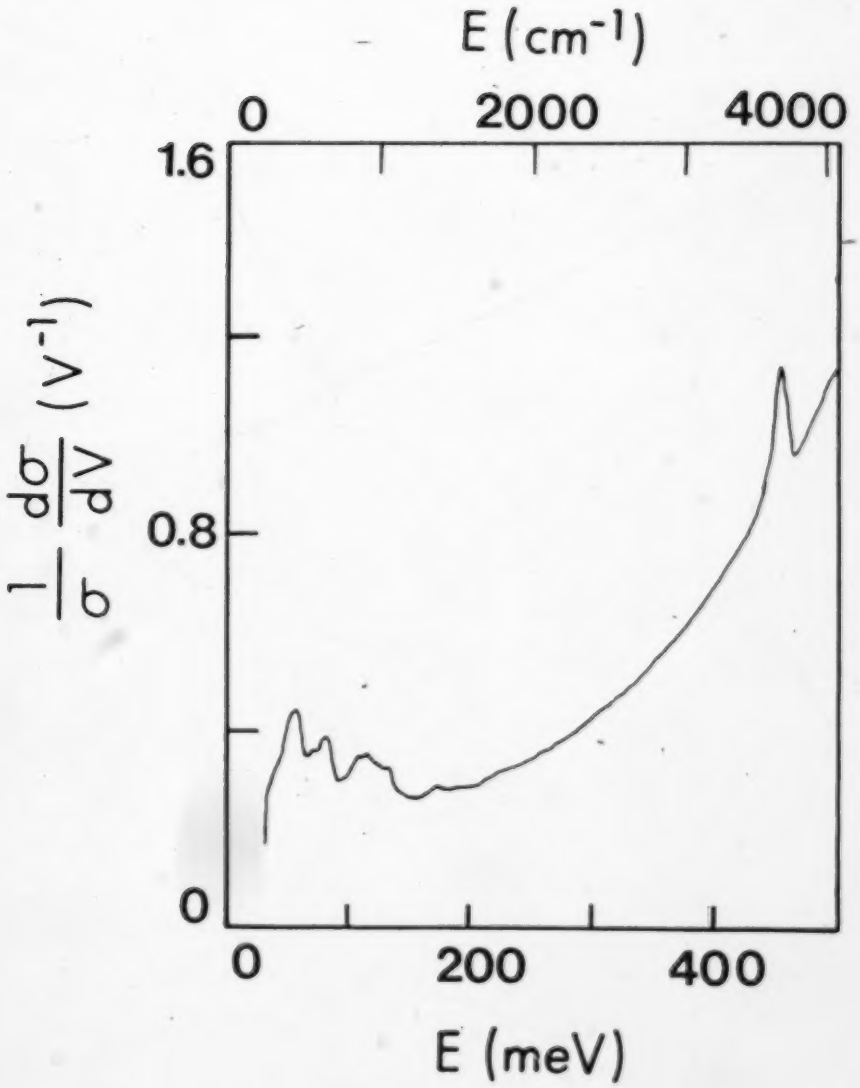
E (cm⁻¹)
0
2000
4000
1.6
0.8
0
$\frac{1}{\sigma}\frac{d\sigma}{dV}$ (V⁻¹)
0
200
400
E (meV)

substantially from lab to lab. The variation depends in a large part on the amount of water present in the vacuum chamber during fabrication (Plesiewicz and Adler, 1986).

The characteristic peak in the spectra at 450 meV is observed in both undoped Al, and Mg junctions and is attributed to hydroxyl groups located close to the cover electrode (Jaklevic and Lambe, 1966; Lambe and Jaklevic, 1968). Water is one of the hardest substances to eliminate from a vacuum system, and the residual water acts as a source of the O-H. The water molecule breaks up during the plasma oxidation and is incorporated into the tunnel barrier.

The assignment of the peak is reinforced by observing the isotopic shift which occurs when heavy water is introduced into the system. A quantitative measure of this shift can provide clues to the environment surrounding the O-H radicals. Klein et al. (1973) found $\omega_{OH}/\omega_{OD} = 1.355 \pm 0.004$. This value is consistent with free O-H molecules or with O-H impurities in a rare gas matrix (Herzberg, 1950; Aquista et al., 1963). The value is also consistent with an internal vibration of $O\text{-}H^-$ radicals in a $Mg(OH)_2$ lattice (Buchanan et al., 1963).

The energy of the peak can also reveal something about the environment of the O-H. The IR work of Glass and Searle (1967) identified a line at 410 meV and a broad band ranging from 440 to 460 meV related to O-H impurities in MgO crystals. The IR spectrum of brucite ($Mg(OH)_2$) (Buchanan et al., 1963; Dawson et al., 1973) indicates that the internal stretching modes of O-H radicals are at 453 and 459 meV which is within the linewidth of the 450 meV peak. The position of the peak does indicate that there is little hydrogen bonding present, since this would shift the peak

to lower energies (Pauling, 1949). These results indicate that that the 450 meV peak is an O-H stretch. We are unable to say if the O-H exists in the form of O-H radicals or as part of $Mg(OH)_2$ using energy considerations alone.

The inelastic peaks below 90 meV were discussed in some detail by Adler (1969), Klein et al. (1973) and Plesiewicz and Adler (1986), who interpreted the peaks in terms of MgO phonons. Peaks were observed in the spectra at 54, 66, and 82 meV. Adler (1969) illustrated that the peaks in the IET spectra show a striking correspondence with the IR measurements of Willmott (1956)and the theoretical predictions of Verma and Dayal (1967), in particular the longitudinal optical (LO) mode at 82 meV. Klein et al. (1973) pointed out that there are discrepancies between the tunneling data and the IR, and neutron (Sangster et. al., 1970) spectra. The IR exhibited a single peak at 50 meV, however the technique is restricted to the observation of transverse optical (TO) modes at $\vec{k} = 0$. The neutron results indicated a low density of high energy phonons, despite the fact that there was a strong LO peak at 82 meV in the tunneling data. Klein et al. (1973) concluded that despite the fact that tunneling reproduces the phonon density of states for covalent, amorphous oxides, tunneling electrons are more likely to couple to LO mode in the crystalline, ionic MgO. Taking this enhancement into account the authors construct a theoretical tunneling density of states which agrees with experiment. The authors ascribed the 54 meV peak in the tunneling data to the TO mode, and the peak at 66 meV was also present in the theoretical curve.

Plesiewicz and Adler (1986) observed that the relative peak intensities depended on the amount of water present during barrier formation. They suggested that OH bending modes were responsible for some of the observed peak intensities at 54 and 66 meV. Plesiewicz and Adler (1986) also indicated that despite the

general agreement between the tunneling data and the neutron reults (Sangster et al., 1970; Rieder and Horl, 1968) the energy of the tunneling peaks were shifted to lower energies. This shift was ascribed to the importance of surface phonons in the MgO microcrystals which make up the barrier. The surface phonons shift the peaks to lower energies in agreement with experiment.

The spectra also exhibits a number of peaks between 110 and 134 meV, and two small bumps located at 160 and 180 meV. The origin of these peaks is unclear. Adler (1969) assigned the peak at 120 meV to a two phonon process in MgO while Klein et al. (1973) suggested it was related to O-H bending. Since the intensity of these peaks increased in junctions which exhibit signs of organic contaminants, Plesiewicz and Adler (1986) ascribed the peaks to the presence of carbon oxides in the vacuum system, and in particular identified the peak at 134 meV to C-H bending.

A brief summary of the preceding discussion is presented in Table 3.1.

Table 3.1

Peak Assignment in Mg-MgO-Pb Tunnel Junctions.

Energy (meV)	Peak Assignment
450	O-H stretch[1]
82	LO mode in MgO[2]
54	TO mode in MgO[3] + O-H bend[4]
66	MgO phonon[3] + O-H bend[4]
120	Two phonon process in MgO[2] or O-H bend[3]
134	C-H bend[4]

1 Jaklevic and Lambe, 1966
2 Adler, 1969
3 Klein et al., 1973
4 Plesiewicz and Adler, 1986

3.4.2 Barrier Parameters.

To analyse the elastic tunneling characteristics, the data is fit to a trapezoidal barrier model (Fig. 3.2) to obtain values for the three parameters ϕ_1, ϕ_2 and d. Two different methods are used to obtain these parameters. The first is a method developed by Brinkman, Dynes and Rowell (BDR) (1969), and the second is based on Harrison's (1961) expressions for the tunneling current.

In the BDR method a polynomial fit of the $\sigma(V)$ data between ±500 mV is made. The region between ±150 meV is excluded from the fit, since the contribution from inelastic tunneling in this energy range is too large. The linear and quadratic terms of the curve are inserted into the BDR expression to obtain the parameters ϕ_1, ϕ_2 and d.

The second method uses an iterative process to obtain the best fit parameters. An initial guess of ϕ_1, ϕ_2 and d is made and using these parameters the tunneling current is calculated numerically using Harrisons expressions (Eq. 3.12). The resulting curve is fit to the experimental data using a least squares technique in order to produce a new set of parameters. This process continues until the iteration converges and yields the best combination of parameters.

3.4.3 Peak Intensity

The area under the peaks in the IET spectra, or the so called peak intensity was also measured. The peak intensity is defined as

$$F(V) = \int_{V_1}^{V_2} \left\{ \left(\frac{1}{\sigma} \right) \frac{d\sigma}{dV} - g(V) \right\} dV \qquad (3.38)$$

where g(V) is an arbitrary fit to smooth background the in the vicinity of the peak and subtracted from the data. In general g(V) is a polynomial fit, however in most cases a linear fit is sufficient. V_1 and V_2 are the lower and upper bounds of the peak in question.

The quantity F(V) is a measure of the increase in tunnel current due to the inelastic channel opening up at voltage V.

3.5 Sample Preparation.

The tunnel junction, or the spectrometer, used in IETS consists of two crossed thin film electrodes which are separated by a thin tunnel barrier (Fig. 3.6). The barrier in this work is provided by the natural oxide of the Mg base electrode.

The junctions were formed by first evaporating a set of silver contacts onto a clean glass substrate. The Mg base film was then evaporated, and subsequently oxidized to form the tunnel barrier. To complete the process the counterelectrode was evaporated. The whole preparation process was performed without breaking vacuum thus enabling strict control over conditions during fabrication.

The substrate was a 1 x 1 cm^2 Pyrex microscope slide. The slide was washed in detergent, rinsed in methanol and fire polished. The substrate was then placed in the vacuum system where further cleaning by both oxygen, and argon plasma glow discharge took place.

The plasma was produced by two concentric copper rings separated by approximately 1 cm. Applying a voltage of about 450 V between the rings in about 200 mTorr of oxygen produced a glow discharge with a plasma current of 10 mA. Oxygen is reactive and is expected to combine with contaminant molecules on the substrate surface which may be subsequently pumped away.

After flushing the system clear of oxygen, a similar argon plasma was produced. Argon atoms are relatively heavy and by bombarding the surface they could dislodge any dirt on the substrate.

The vacuum system was pumped for several hours prior to junction fabrication. Pumping was provided by an oil diffusion pump, which was separated from the

FIGURE 3.6 Diagram of a pair of tunnel junctions. First the Ag contacts are evaporated on to the 1 cm^2 glass microscope slide. Next the Mg film is evaporated and oxidized. The final step is the evaporation of the cover electrodes.

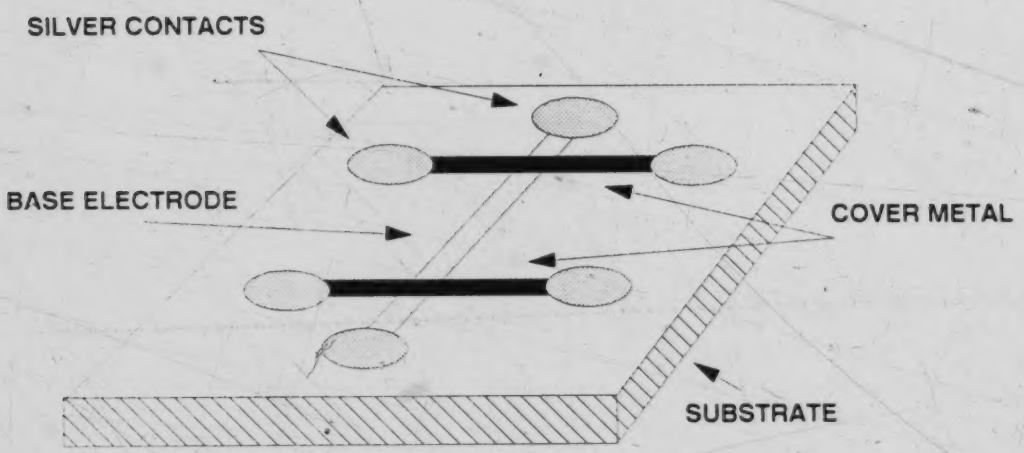
SILVER CONTACTS
BASE ELECTRODE
COVER METAL
SUBSTRATE

preparation chamber by a liquid nitrogen trap to avoid backstreaming of pump oil into the chamber. After pumping the pressure in the system was reduced to about $1x10^{-7}$ Torr.

The first step in junction fabrication was the evaporation of silver contacts. The silver contacts, the Mg base electrode, and the cover electrode were all evaporated from resistively heated boats or filaments. The geometry of both the films and the contacts was determined by evaporating through stainless steel defining masks. In order to facilitate the evaporation of all three metals without breaking vacuum, the evaporation sources were incorporated into a rotating carousel. Each source was surrounded by a glass chimney to avoid cross contamination, and the samples were placed on a holder which could be both rotated, and moved vertically with respect to the carousel.

The Mg base film was evaporated from a tubular covered boat at a rate of 20 Å/s to a thickness of 2000 Å The rate and thickness were measured by a Sloan DTM-3 quartz crystal monitor. Following the evaporation, the substrates were placed in close proximity to the concentric copper rings for formation of the tunnel barrier. The exact recipe for barrier formation depended on the system environment and the desired junction.

The environment inside the vacuum chamber was controlled by a large area Meissner trap. The trap was situated so that it was close to the substrates during barrier formation. The trap had an active area of about 10^4 cm^2, and when cooled to liquid nitrogen temperature the trap reduced the partial pressure of water in the system to 10^{-9} Torr (Plesiewicz and Adler, 1986).

Once the oxidation was complete, the system was pumped down again and a 2000 Å thick counterelectrode evaporated. A list of the different cover electrodes and their respective evaporation sources is given in table 3.2.

TABLE 3.2

Evaporation Materials

Metal	Purity	Supplier	Evaporation Source
Al	59	Alfa	W coil
Ag	69	Cominco	Mo boat
Au	69	Cominco	W basket
Cd	69	Cominco	Mo boat
Cu		INCO	Mo boat
In	39	Johnson	Mo boat
Mg	59	Matthey	Ta covered boat
Pb	69	Cominco	Mo boat
Sn	59	Cominco	Mo boat
Zn	69	Cominco	Mo boat

3.5.1 Formation of the Tunneling Barrier.

Since the Meissner trap modified the system environment, this allowed a variety of barrier preparation procedures. With the trap activated the partial pressure of water in the system was reduced, and will be referred to as the dry environment. Without the trap activated the environment is considered wet.

In the wet system the barrier was formed by exposing the freshly evaporated Mg film to a pure oxygen plasma glow discharge similar to that used for cleaning. The amount of oxidation and thus the thickness of the tunneling barrier depends on the plasma current, the pressure, and the time of exposure (Miles and Smith, 1963). To obtain junctions with the desired resistance, a typical current of 13 mA at a pressure of 200 mTorr was maintained for between 10 to 20 minutes. These junctions are referred to as plasma junctions.

The remaining methods of barrier formation were all performed in the dry system, i.e. with the Meissner trap activated. The first used a plasma oxidation similar to that of plasma junctions. To obtain finite tunneling resistances the Mg film required exposure times in excess of 1 hour. These junctions are referred to as dry junctions. Gun junctions were also prepared in the dry environment. With gun junctions, the magnesium film was exposed to a flux of low energy hydrogen ions from a saddle field ion gun immediately after evaporation for 3 to 6 min. The ion current during this pretreatment was 0.35 mA and a dynamic pressure of 1.2×10^{-5} Torr was maintained. After the treatment, the film was oxidized in an oxygen plasma discharge for 8 to 10 minutes. Molecular junctions were made by exposing the Mg film to a flux of H_2 gas for similar times and pressures as the ionic exposure in gun junctions. In order to obtain the desired resistance, the junctions were plasma oxidized for 20 to 30 min.

3.5.2 Cover Electrode Formation.

After formation of the tunnel barrier the system was pumped to below 10^{-6} Torr and the cover electrode evaporated. All steps in junction fabrication were performed without breaking vacuum, and in the dry environment, the Meissner trap

was kept cold from 20 minutes prior to the Mg evaporation until after the cover electrode was evaporated. The careful control of the system environment meant the success rate of junctions in a useable resistance range of 10 to 500 Ohms approached 100%.

After preparation, the samples were placed in a holder. The sample holder makes contact to the junction electrodes by gold pressure contacts. The electrical continuity of both the contacts and the electrodes was checked and the holder was placed on a long stainless steel dipstick and stored in liquid nitrogen for subsequent measurement at 4.2 K.

3.6 Results and discussion

In this chapter we discuss the results of our measurements on Mg based tunnel junctions. In particular we will show how different preparation environments influence the oxidation of the tunnel barrier. We investigate how, and why hydrogen ion pretreatment helps to produce a "better" barrier, and the effect of different cover electrodes on the tunneling properties of the junction.

3.6.1 Results

Four types of junctions were prepared as dicussed in section 3.5. Plasma junctions were prepared in the wet system, while dry junctions, molecular junctions and gun junctions were prepared with the Meissner trap cooled to liquid nitrogen temperatures. With the exception of dry junctions, all procedures resulted in junctions suitable for IET spectroscopy. Dry junctions had to be oxidized for extended periods to obtain finite tunneling resistances, however these junctions had very low barrier heights making spectroscopy impossible.

The plasma oxidation time for gun junctions was the shortest (~12 minutes), followed by plasma junctions which required about 15 minutes exposure, and molecular junctions needed about 25 minutes of oxidation.

Figure 3.7 illustrates the IET spectra for a number of plasma and gun junctions prepared with different cover electrodes. Molecular junctions were prepared only with lead, and the spectra were similar to plasma junctions, and will not be discussed explicitly. Most of the peaks in the spectra have been identified in previous tunneling work (Adler, 1969; Klein et al., 1973; Plesiewicz and Adler, 1986) as discussed in section 3.4.1. The exception is the large peak at 124 meV in gun junctions. The position of this peak and the peak intensity was found to be independent of the cover

FIGURE 3.7 IET spectra of Mg-MgO-Metal junctions. (a) and (b): gun junctions. (c) and (d): plasma junctions. The quality of the plasma oxide made it impossible to produce plasma junctions with Al or Mg cover electrodes.

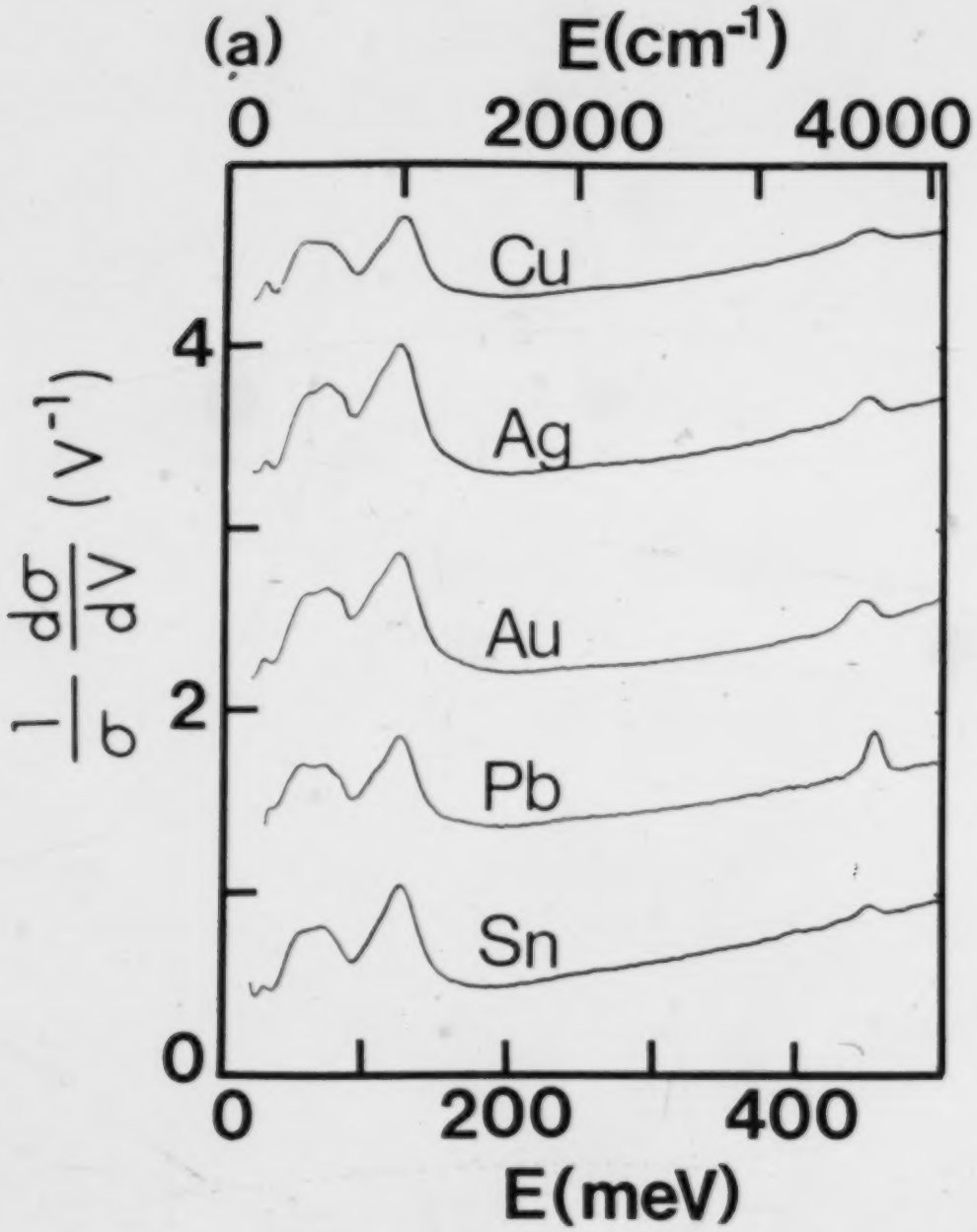
(a)
E(cm-1)
0
2000
4000
Cu
Ag
Au
Pb
Sn
4
2
0
1/σ dσ/dV (V-1)
0
200
400
E(meV)

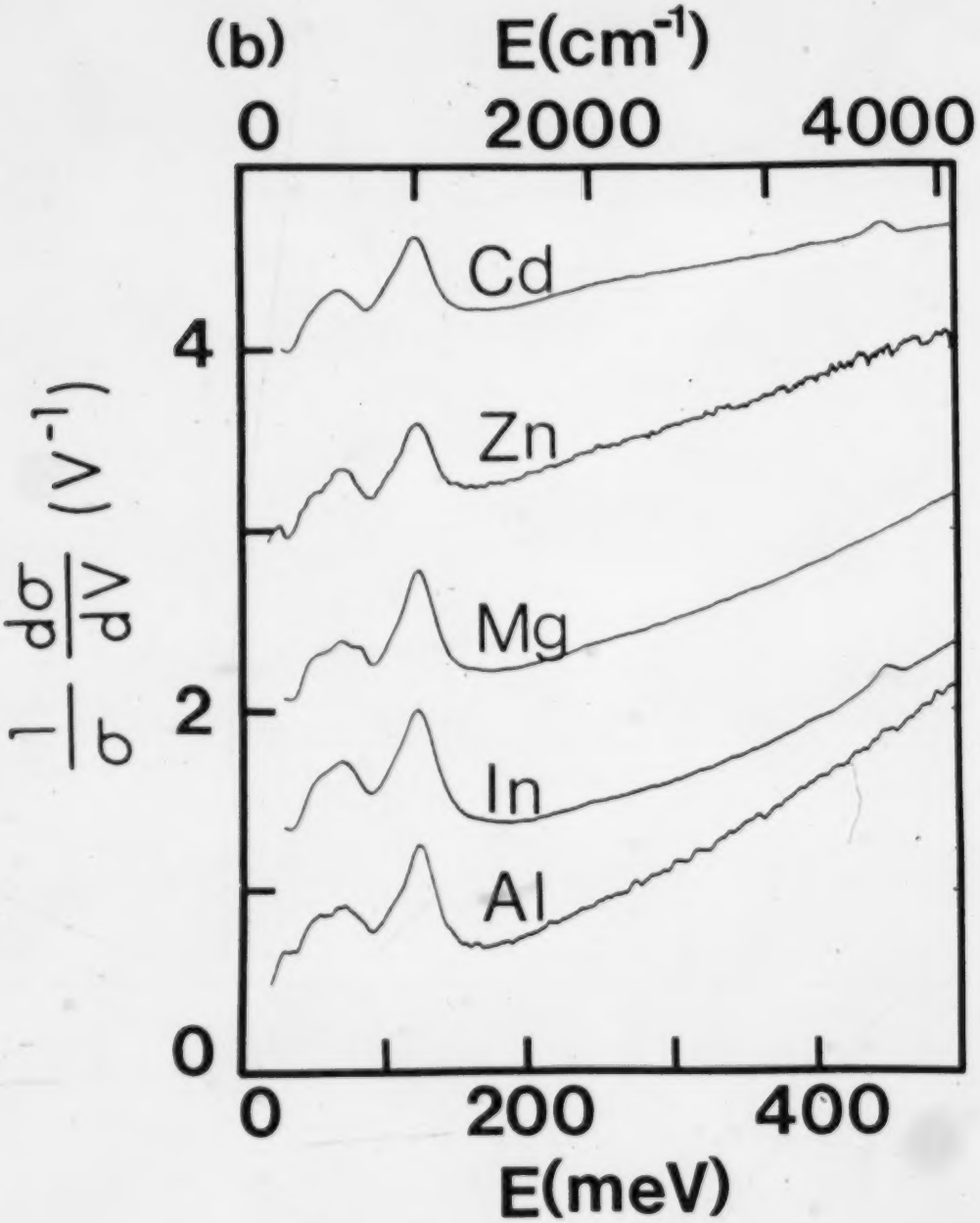
(b)
E(cm^{-1})
0
2000
4000
Cd
Zn
Mg
In
Al
4
2
0
$\frac{1}{\sigma}\frac{d\sigma}{dV}$ (V^{-1})
0
200
400
E(meV)

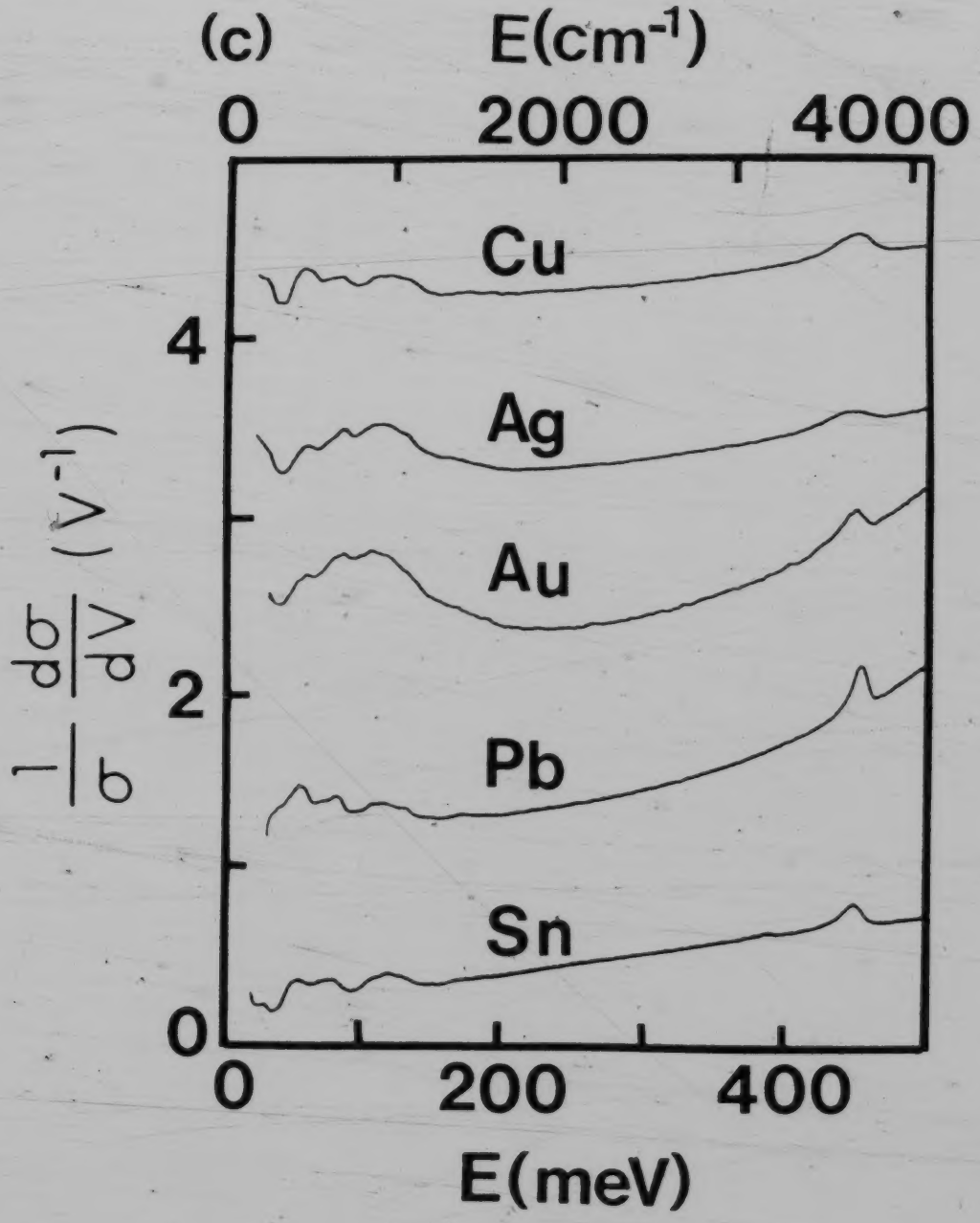
(c)
E(cm-1)
0
2000
4000
Cu
Ag
Au
Pb
Sn
4
2
0
1/σ dσ/dV (V-1)
0
200
400
E(meV)

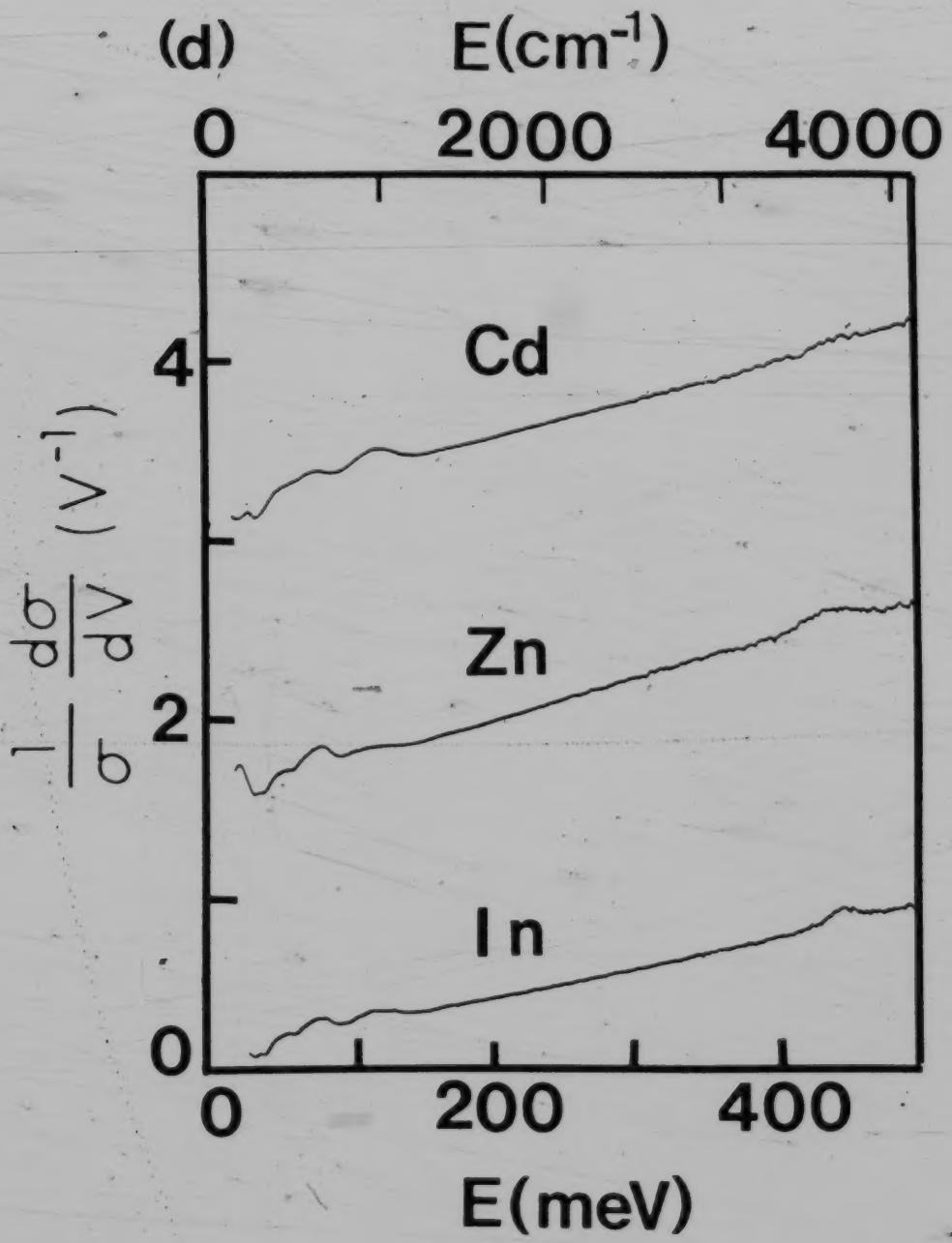
(d)
E(cm-1)
0
2000
4000
Cd
Zn
In
4
2
0
1/σ dσ/dV (V-1)
0
200
400
E(meV)

electrode. Hydrogen ion pretreatment of the magnesium was essential to the occurrence of this peak. In stark contrast to similiar studies on aluminum based tunnel junctions (Igalson and Adler, 1983), any attempt to produce the peak with ion exposure after oxidation proved unsuccessful. Pretreatment with molecular hydrogen was also unsucessful.

TABLE 3.3 Barrier Parameters (in eV)

	Plasma				Gun			
	ϕ_1	ϕ_2	$\bar{\phi}$	$\phi_2-\phi_1$	ϕ_1	ϕ_2	$\bar{\phi}$	$\phi_2-\phi_1$
Ag	1.05	8.40	4.72	7.35	0.44	8.47	4.45	8.03
Al	0.64	0.95	0.80	0.31	0.93	3.06	2.46	3.06
Au	1.53	8.32	4.93	6.79	-1.62	11.39	4.88	13.01
Cd	4.83	1.17	3.00	-3.67	2.37	3.28	2.82	0.91
Cu	0.90	9.56	5.23	8.66	-0.18	10.38	5.10	10.55
In	2.59	4.53	3.56	1.94	1.44	4.73	3.09	3.30
Mg					1.39	4.55	2.97	3.16
Pb	3.21	4.82	4.02	1.61	1.06	6.40	3.73	5.34
Sn	1.13	6.61	3.87	5.48	0.54	7.47	4.00	6.93
Zn	1.92	2.50	2.21	0.58	2.25	3.03	2.64	0.78

In general, the average barrier height of both gun and plasma junctions were similar, however gun junctions tended to be more asymmetric. Asymmetry in tunnel junctions, in excess of the difference in work functions, has been related to the presence of hydroxyls at the oxide cover electrode interface (Igalson and Adler,

1983). Surface hydroxyls have a dipole moment which contributes to the intrinsic electric field in the barrier. Quantitative analysis of the peak intensity of the 450 meV hydroxyl peak indicates that the amount of O-H is similar in both gun and plasma junctions, and suggests that the added asymmetry in gun junctions must have an additional origin.

The barrier parameters of both plasma and gun junctions is listed in table 3.3. Clearly the negative ϕ_1 evident in some gun junctions is unphysical. The values result from trying to fit the highly asymmetric tunneling characteristics to a simple trapezoidal barrier. For this reason the parameters should not be taken too literally, but they can be used as a quantitative measure of the steepness and asymmetry of the tunneling characteristics.

3.6.2 Gun Junctions

The hydrogen ion pretreatment had a unique effect on the properties of the resultant tunnel junction. The large peak at 124 meV is unique to gun junctions, and after pretreatment the films tended to oxidize more readily.

Looking at the 124 meV peak in more detail, it is found that initially the peak intensity increases with ion exposure, and saturates after about 2 minutes exposure. If the film is pretreated with deuterium, the peak shifts to 88 meV as expected in a harmonic approximation (Fig 3.8). The results indicate that the peak is clearly hydrogen related.

The increased asymmetrty in gun junctions must also be related to the hydrogen pretreatment. ϕ_1 is consistently lower in gun junctions, and indicates that the source

FIGURE 3.8 IET spectra of Mg-MgO-Pb gun junctions. Pretreatment with deuterium shifts the 124 peak to 88 meV.

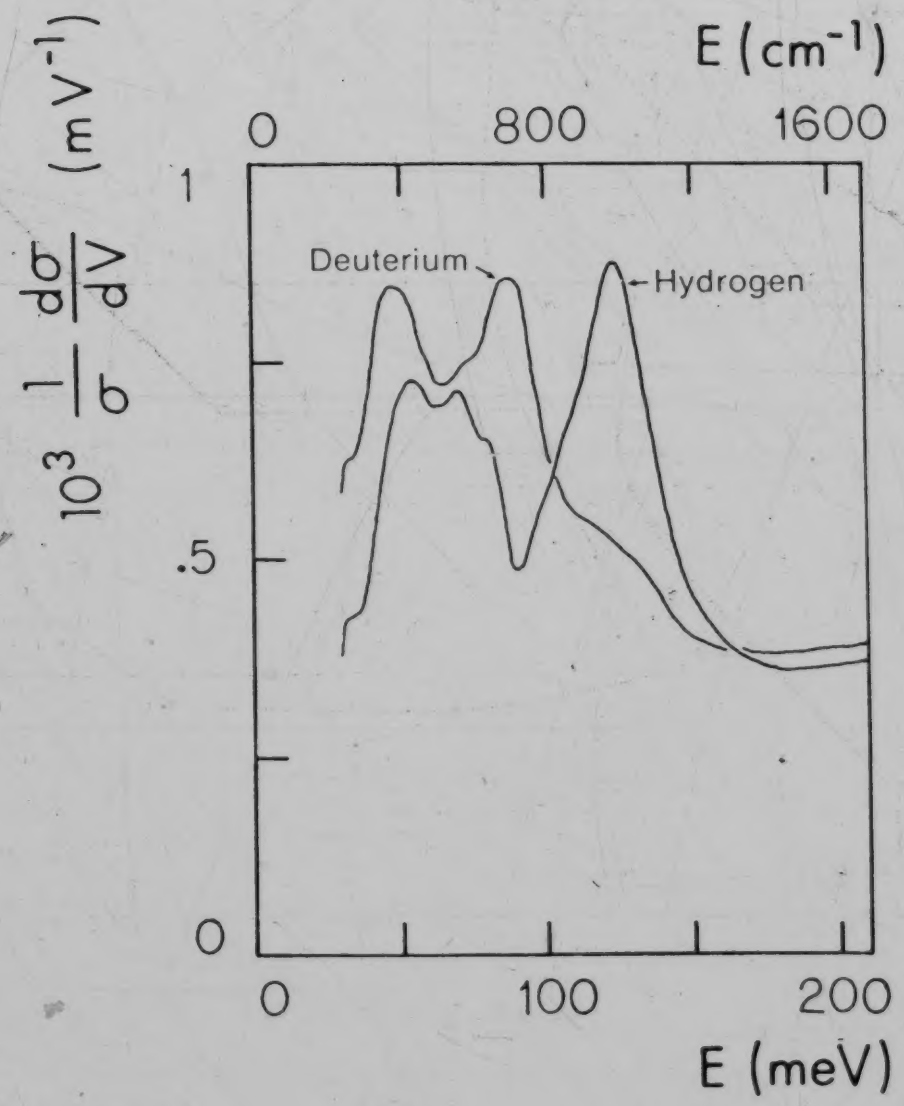
E (cm⁻¹)
0
800
1600
1
.5
0
$10^3 \frac{1}{\sigma} \frac{d\sigma}{dV}$ (mV⁻¹)
Deuterium
Hydrogen
0
100
200
E (meV)

of the peak is localized in the vicinity of the magnesium, magnesium oxide interface. Considering these results, the peak at 124 meV is ascribed to chemisorbed H at the Mg surface.

The important first step in hydrogen chemisorption on a metal surface is the dissociation of the hydrogen molecule (Hjelmberg, 1979). In simple s like metals like Mg, this dissociation energy can be quite high, making hydride formation unlikely (Johansan, 1981). By exposing the Mg film to a flux of hydrogen ions we provided a source of dissociated hydrogen, and explains why we saw no evidence of the 124 meV peak after exposure to molecular hydrogen.

Hjelmberg (1979) presented calculations for the chemisorption of atomic hydrogen on Mg (0001). Two stable sites were found, one on the surface of the metal and the other subsurface. The energy of diffusion into the subsurface site is quite low, making them relatively easy to populate. The vibrational energy for the surface site is 80 meV while the subsurface energy is 140 meV. Hjelmberg's calculations were done using a rigid lattice approximation, and any relaxation effects would reduce these energies somewhat. The bond lengths at the sites were found to be similar to bulk MgH_2. Infrared measurements on bulk MgH_2 (Mal'tseva and Kharitonov, 1962) indicated the presence of a broad band extending from 110 to 200 meV with a maximum at about 140 meV.

The lack of any peak in the IET spectra below 124 meV attributable to hydrogen in gun junctions, eliminates contributions from surface sites, and indicates that the peak at 124 meV is due to hydrogen chemisorbed at subsurface sites on the

magnesium surface. The low ϕ_1 in gun junctions supports this conclusion. Subsurface sites would create Mg-H dipoles with moments pointing away from the surface, resulting in a decrease of the barrier height at the Mg surface.

Despite the behaviour of ϕ_1, indicating that source of the peak is located close to the Mg surface, possible sources of the peak from within the oxide should be considered. MgO is known to contain impurities such as OH^- radicals, H_2, $Mg(OH)_2$ precipitates, or H^- substitutional sites (Dawson et al., 1973; Buchanan et al., 1963; Gonzalez et al., 1981; Freud and Wengler, 1982). Infrared and Raman studies have been performed on crystals containing such impurities. The vibrational modes resulting from $Mg(OH)_2$ precipitates can be split into two energy regimes. The lower energy regime includes modes with vibrational energies less than 80 meV and in the second the energies exceed 400 meV (Dawson et al., 1973; Buchanan et al., 1963). There is no mode due to $Mg(OH)_2$ located at 124 meV. In a similar manner, vibrational modes related to OH^- or H_2 can be ruled out (Gonzalez et al., 1981; Freud and Wengler, 1982).

Unlike most impurities which tend to grow as a natural result of oxide growth in the presence of water vapor, H^- sites are created only after severe chemical reduction of the oxide crystals after growth. The H^- site is produced when hydrogen replaces oxygen in the oxide lattice, and in this way the site has a net negative charge with respect to the surrounding lattice. Raman studies (Gonzalez et al.,1981) indicated that the vibrational energy of these sites is 124 meV, the same energy as the peak in the IET spectra. We attempted to produce H^- sites after oxidation by exposing the oxidized film to the same flux of hydrogen ions as gun junctions, but were unsuccesssful.

If the 124 meV peak were the result of H^- sites, these sites would be expected to distribute evenly throughout the oxide, yet the low ϕ_1 indicates that the source of the peak is concentrated close to the magnesium, magnesium oxide interface. Is it possible that chemisorbed H may evolve to produce H^- sites during oxidation?

The position of chemisorbed hydrogen, and H^- sites in MgO are different with respect to the underlying magnesium lattice. Figure 3.9 indicates the location of the subsurface H in Mg (0001) and the oxidation of this surface to produce MgO (111) is illustrated in Figure 3.10. For chemisorbed H to evole into H^- substitutional sites the chemisorbed hydrogen must move with respect to the magnesium sublattice.

During hydrogen ion treatment, hydrogen would tend to penetrate some distance into the oxide, since the energy of diffusion is low. During oxidation, mobile oxygen atoms would likely bond with any free hydrogen due to the strength of the bond, and produce OH radicals rather than allow the formation of H^- sites. As a result, after oxidation chemisorbed hydrogen is located below the magnesium surface and OH radicals reside at the surface of, or within the oxide.

The low ϕ_1, and the required movement of hydrogen with respect to the magnesium lattice means the creation of H^- sites from chemisorbed hydrogen is unlikely. For this reason we conclude that the peak at 124 meV is due to the stretching vibration of hydrogen chemisorbed at subsurface sites on the magnesium surface.

3.6.3 Oxidation

Magnesium tends to form a crystalline oxide. Using the oxidation of Mg (0001) as an example (Namba et al., 1981; Gjisen et al., 1981), one finds that the lattice

FIGURE 3.9 A top view of the Mg(0001) surface (a), hydrogen (denoted by H) chemisorbs on top of Mg atoms in the second layer (○) (b). The chemisorbed hydrogen tends to attract the surrounding magnesium atoms opening up the surface to facilitate the incorporation of oxygen atoms (○).

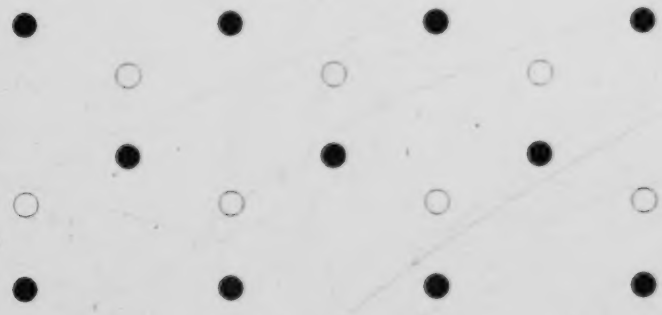

(a)

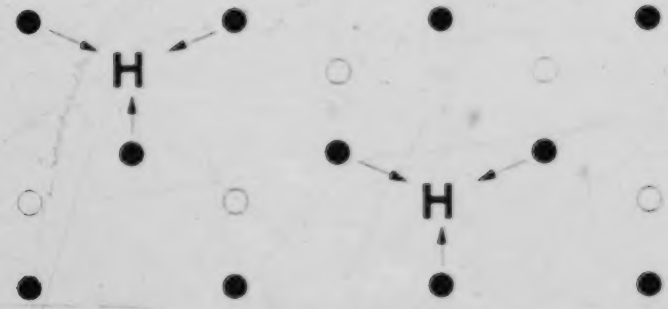

(b)

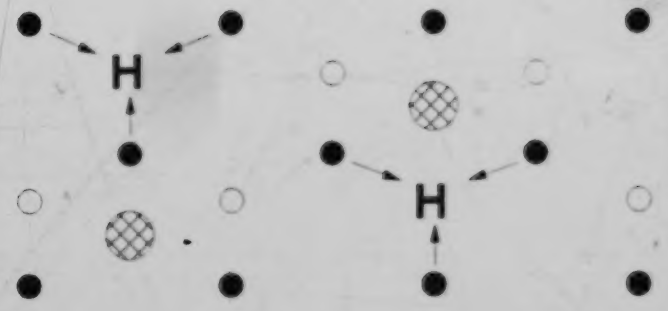

(c)

FIGURE 3.10 Incorporation of oxygen at the Mg(0001) surface: (a) top view, (b) side view. The initial incorporation takes place at subsurface sites with local symmetry of MgO(111). (●) are Mg atoms in the first layer, (○) are second layer atoms and (◎) are oxygen atoms.

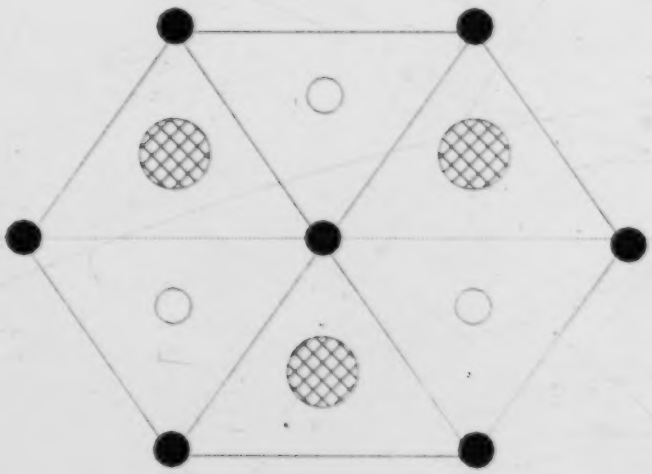

(a)

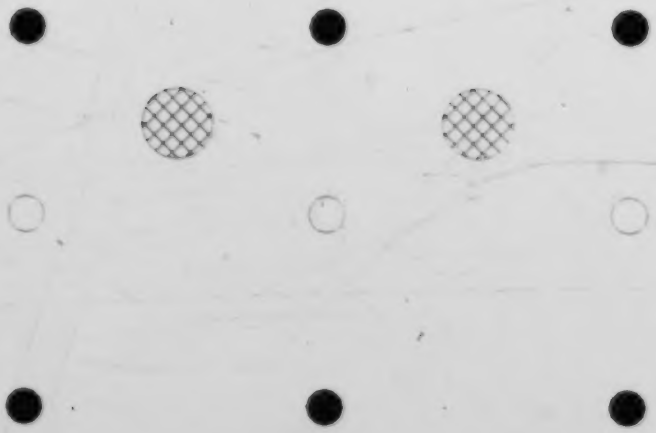

(b)

parameter of MgO in the [111] direction is very close to Mg (0001) normal to the surface. This similarity makes it relatively easy for oxygen to incorporate below the surface layer of Mg (0001) without much disruption of the lattice as shown in Fig. 3.10. The lattice is not as well matched parallel to the surface, and this mismatch makes it energetically favorable for oxidation to proceed by island growth. The islands tend to have parameters closely resembling bulk MgO (111) at the center and relax towards the perimeter. Initial oxygen chemisorption tends to take place at local defects on the magnesium surface which act as nucleation sites. The islands then grow together to form the first layer of oxide (Namba et al., 1981; Gjisen et al., 1981). Further layers of the oxide grow by a place exchange mechanism (Namba et al., 1981; Kirk and Huber, 1968; Eley and Wilkinson, 1960).

The better quality tunnel junctions tended to have large O-H peaks in the tunneling spectra, thus the presence of water seemed benefical. O-H is known to act as a catalyst in oxide growth by reducing the local work function, making oxygen chemisorption easier. It may be that adsorbed O-H acts as a nucleation site for island growth.

The peak intensity of the 450 meV O-H peak was similar in plasma, gun and molecular junctions. The residual water in the vacuum system is sufficient to produce the observed peak intensity in plasma junctions, however this not true for both the gun and molecular junctions which were fabricated in lower partial pressures of water.

The preparation techniques for junctions in the dry system required the introduction of hydrogen into the vacuum system. Pretreatment of magnesium was essential for the formation of usable tunnel junctions. Hydrogen may have produced O-H in one of two ways. Residual hydrogen in the system after petreatment could

have combined with oxygen in the glow discharge to produce O-H radicals, or the chemisorbed hydrogen on the magnesium film may have combined in much the same way. Results indicated that the O-H peak intensity in gun junctions was slightly higher than molecular junctions. The increased intensity indicates that some O-H was produced from the chemisorbed hydrogen.

The O-H peak intensity in gun and plasma junctions were similar, yet the oxidation time required to produce gun junctions was less. Since the amount of O-H was similar, the increased efficiency of oxidation must be related to the presence of chemisorbed hydrogen.

Most oxidation studies of Mg have been performed in UHV environments and at least one study included Meissner traps (Namba et al., 1981). None of these groups had any problems oxidizing magnesium in these dry environments, so why was hydrogen pretreatment essential for the tunneling experiments?

Tunneling puts a stringent requirement on the oxide layer, not only must the oxide be of suitable thickness, but it must be relatively uniform and free of any pinholes which may short out the junction. The barrier parameters of dry junctions indicated low barrier heights and large thicknesses characteristic of patchy oxides (Halbritter, 1983). Liehr and Ewert (1983) found that the large aluminum oxide peak in the IET spectra, characteristic of Al based tunnel junctions, disappeared as the oxide became more crystalline. Work on all refractory superconducting tunnel junctions with artificial MgO barriers also indicated the undesirable aspects of crystalline barriers. Talvacchio et al. (1985) found that as the crystal structure of the barrier became more defined, the superconducting tunneling characteristics deteriorated.

The crystallinity of the oxide depends on the grain size of the underlying magnesium film, and the number of nucleation sites available for oxide growth. Liehr and Ewert (1983) found that by reducing the system pressure the grain size of the metal film could be increased. Magnesium films evaporated in the wet system were exposed to a higher system pressure and a higher partial pressure of water. This may have resulted in films with smaller grain size, and subsequently a more amorphous barrier. Conversely, magnesium films evaporated in the dry system would exhibit larger grain size. The barrier parameters of dry junctions indicated low barrier heights, and large thicknesses characteristic of granular oxides.

Despite the large grain size of the underlying magnesium film, the tunneling characteristics of gun junctions indicated that the barrier was quite uniform. When hydrogen is chemisorbed into subsurface sites on the magnesium surface, it tends to open up the metal surface and makes oxygen incorporation easier (Fig. 3.10). In this way the hydrogen acts as an additional nucleation site for island growth and contributes to more uniform oxide growth. The uniformity was tested by performing annealing experiments on the tunnel junctions. Gun junctions were found to be the most stable, exhibiting longer lifetimes before developing microshorts. The added stability resulted from the lower ion mobilities characteristic of a more uniform barrier.

3.6.4 Influence of Cover Electrode

The properties of the MgO barrier were found to depend on the choice of cover electrode. The tunneling characteristics of both gun and plasma junctions with a number of different cover electrodes were measured. Despite the fact that gun junctions were more asymmetric, the average barrier height for both tended to be

similar. In Fig. 3.11 the barrier heights of both gun and plasma junctions are plotted against the ionic radius of the cover electrode. The plots indicate that the barrier height of the junctions increased with the ionic radius of the cover metal.

When the cover metal is evaporated onto the oxide to complete the junction, the metal penetrates somewhat in the oxide layer. MgO is a granular oxide and the penetration tends to take place at pinholes and grain boundaries. Metals with smaller ionic radii are more mobile and are able to penetrate more easily. The small ionic radius of both Al and Mg, and the quality of the plasma oxide made fabrication of junctions with these cover electrodes difficult. This difficulty was not apparent with gun junctions and indicates that the gun oxide was more uniform with a smaller percentage of imperfections. The uniformity of the gun oxide was also apparent by the fact that the variation in the barrier height between different cover metals was not as large as with plasma junctions.

In many ways it is suprising that the peak positions in IETS resemble the results of other techniques as closely as they do, considering that the molecules are buried in a solid state structure with deposition of the cover electrode. Despite this, it is found that if gross chemical reactions between the molecule and the cover metal are avoided, the frequencies of vibration do not change very much. By varying the cover metal one can gain insight into the influence of the covermetal on the vibrational frequencies in IETS.

Inspection of the IET spectra of junctions prepared with various cover electrodes indicated that all the spectral features observed in plasma junctions were evident in gun junctions, although the relative peak intensities differed. In addition,

FIGURE 3.11 The average barrier height verses the ionic radius of the cover metal for both gun and plasma junctions. Cover electrodes with smaller ionic radii result in junctions with lower barriers.

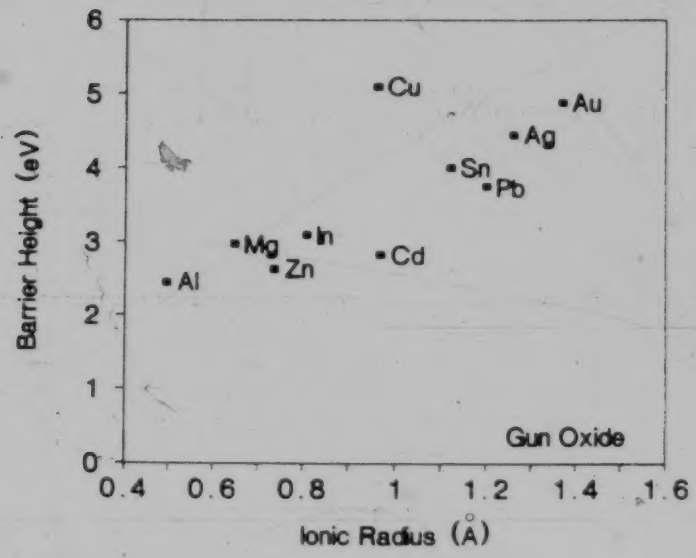
Barrier Height (eV)
Ionic Radius (Å)
Gun Oxide
Cu
Au
Ag
Sn
Pb
In
Mg
Zn
Cd
Al
0
1
2
3
4
5
6
0.4
0.6
0.8
1
1.2
1.4
1.6

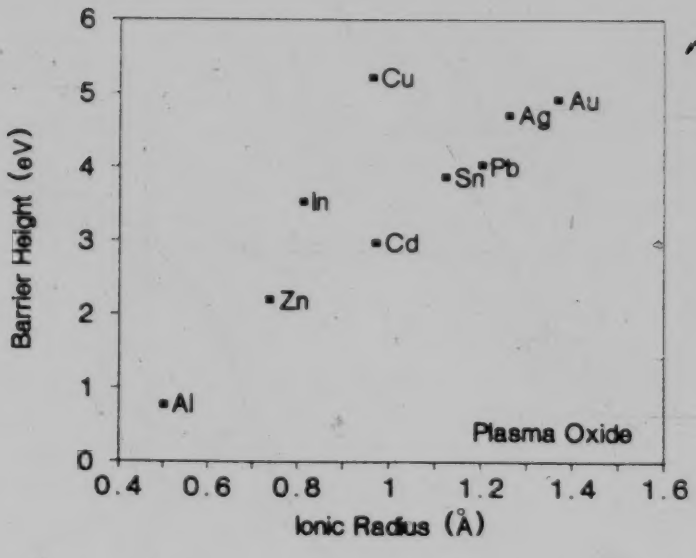
Barrier Height (eV)
Ionic Radius (Å)
Plasma Oxide
Cu
Au
Ag
Pb
Sn
In
Cd
Zn
Al
0
1
2
3
4
5
6
0.4
0.6
0.8
1
1.2
1.4
1.6

the choice of cover electrode affected the peak intensity. Like the barrier parameters, the gun spectra seemed less affected as a result of the more uniform, or "tough" gun oxide.

Generally the energy of the peaks remained constant regardless of the type of oxide, the choice of cover electrode, or the direction of current flow. The exception was the peak in the vicinity of 450 meV attributed to the stetching mode of hydroxyls in the barrier (Jaklevic and Lambe, 1966). This peak was observed in most all spectra. Both the peak position, and intensity for both the positive and negative bias were measured for various cover electrodes, and are shown in table 3.4. The polarity is measured with respect to the Mg base electrode.

The table reveals a number of tendencies in the data. The vibrational energy of the peak depended on the cover metal used to complete the junction, and this energy was lower when excited by electrons tunneling out of the magnesium base electrode. The intensity also depended both on the choice of cover electrode and the on the polarity. The intensity was larger when electrons tunneled out of the magnesium.

The peak intensity is a measure of the number of impurities giving rise to a peak, and the coupling strength of these impurities with the tunneling electrons (Scalapino and Marcus, 1967). The asymmetry in peak intensities may be explained using the fact that electrons with higher energy are more likely to penetrate the barrier. For this reason, it is more probable that an electron will first traverse the barrier elastically, then excite a vibrational mode close to the interface (Kirtley et al., 1976). The larger peak intensity was observed when electrons tunneled out of the magnesium electrode, and suggested that there is a higher concentration of hydroxyls

at the cover electrode interface. The hydroxls are expected to reside on the surface of the oxide with the H^+ pointing outwards normal to the surface (Konkin and Adler, 1976).

TABLE 3.4 O-H Peak Intensities and Peak Positions

	Plasma				
	$F(-450)x10^3$	$F(450)x10^3$	F_{av}	E(-) (meV)	E(+) (meV)
Ag	2.75	1.20	1.98	442.5	452.0
Au	2.70	2.60	2.65	445.5	449.0
Cu	3.85	2.88	3.36	447.3	449.3
In	1.90	1.30	1.60	453.5	450.0
Pb	2.80	2.77	2.79	452.6	453.6
Sn	2.72	1.58	2.15	450.2	451.0
	Gun				
	$F(-450)x10^3$	$F(450)x10^3$	F_{av}	E(-) (meV)	E(+) (meV)
Ag	2.10	1.60	1.85	446.9	450.7
Au	2.73	2.00	2.36	444.3	449.0
Cd	1.20	0.94	1.07	448.5	453.5
Cu	2.65	1.55	2.10	446.0	450.5
In	1.35	0.89	1.12	450.5	455.0
Pb	3.60	2.40	3.00	452.8	453.8
Sn	0.83	0.70	0.77	448.2	451.3

Reasons for the shift in the vibrational energy of the hydroxyl peak with different cover electrodes was discussed by Kirtley and Hansma (1976). One mechanism considered by the authors, which takes into account the proximity of the hydroxyl to the cover metal, is an image dipole effect. When a dipole oscillates in front of a metal surface, it will couple with it's image. The coupling will distort the molecule into a new equilibrium configuration, and as a result reduce the vibration frequency. The frequency shift can be estimated using the expression,

$$\omega_0 - \omega \propto \frac{q^2}{(m\omega_0 d^3 n^2)}, \tag{3.39}$$

where q is the effective charge of the dipole, ω_0 is the unperturbed oscillation frequency, m is the reduced mass, n the real index of refraction of the oxide and d is the distance between the dipole and the imaging plane.

According to Kirtley and Hansma (1976), when the cover electrode is varied the distance between the dipole and imaging plane is changed. This distance d can be related to the atomic radius of the cover electrode. By plotting the energies of the hydroxyl peaks against the atomic radius of the corresponding cover metal (Fig. 3.12), it is found that indeed metals with larger atomic radii shift the peak to lower energies.

Besides the image dipole effect Kirtley and Hansma (1976) also considered a chemical origin for the observed shift. It was suggested that the cover metal may bond with the hydroxyl impurities. With the hydroxyls oriented normal to the surface of oxide the chemical bond would be between hydrogen and the cover metal. The tendency of a metal to interact with hydrogen is measured by a quantity known as d

FIGURE 3.12 Hydroxyl peak energy plotted against the atomic radius of the cover electrode for Mg-MgO-Metal gun junctions. Lower energies (larger shift) are observed in junctions with small atomic radii.

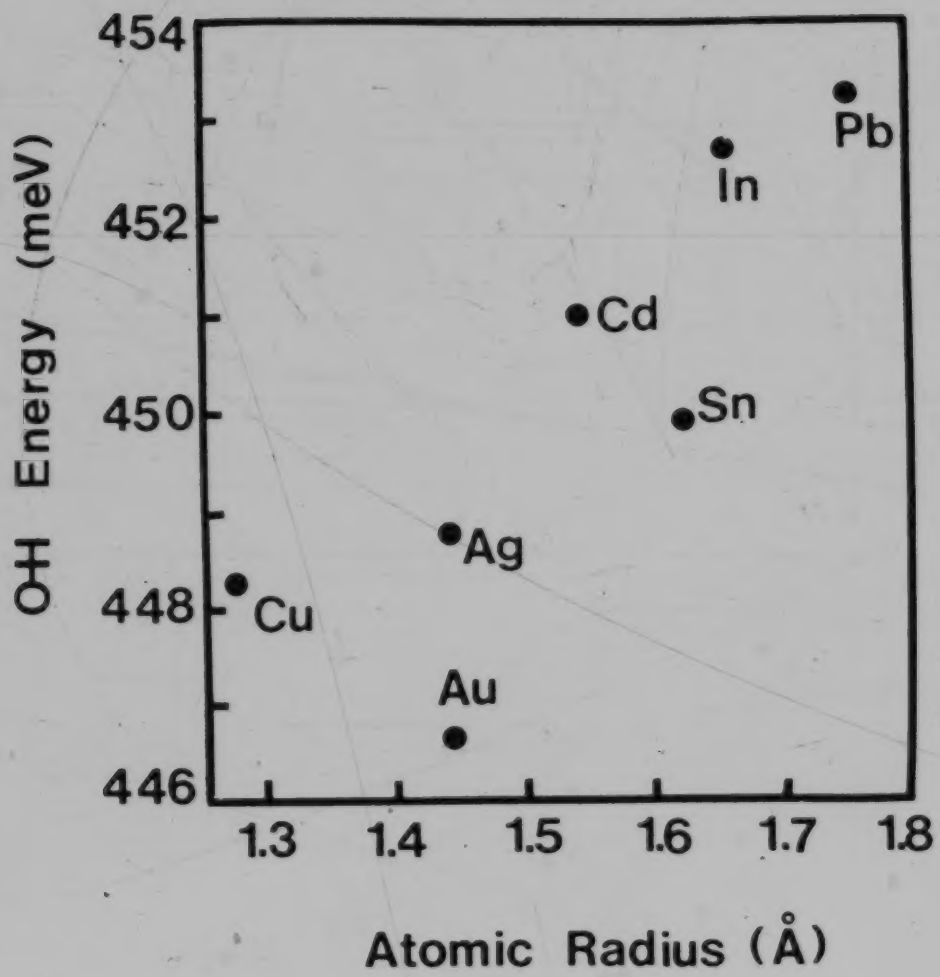
454
452
450
448
446
OH Energy (meV)
Pb
In
Cd
Sn
Ag
Cu
Au
1.3
1.4
1.5
1.6
1.7
1.8
Atomic Radius (Å)

character (Pauling, 1949). Metals with larger d character are more likely to form a bond. Bonding between hydrogen and the metal reduces the electron density of the O-H bond and decreases the vibrational frequency of peak.

A plot of the vibrational frequency of the hydroxyl ion against the percentage of d character of the cover electrode (Fig 3.13) indicates that the larger the d character, the larger the shift in frequency in agreement with Kirtley and Hansma (1976).

As table 3.2 illustrated, not only does the energy of the hydroxyl peak depend on the choice of cover electrode, it also depends on the direction of current flow. The peak is shifted to lower energies on the negative side, and the size of the shift depends on the cover electrode.

Adkins and Sleigh (1987) considered the problem of the top electrode shift and the polarity shift of the hydroxyl peak. They suggested that both effects are the result of the same mechanism. The authors considered how the equilibrium displacement of the hydrogen atom is influenced by different interactions. They considered the influence of the of the molecular potential, the effect of the image potential, and the dependence on the applied field across the barrier. The modified equilibrium position depends on the relative strengths of these effects, and the new position results in a shift of the vibrational energy.

By using a Morse potential for the inter atomic potential, and an expression similar to Kirtley and Hansma (1976) for the image dipole interaction, they reproduced the observed top-electrode shift quite well. Kirtley and Hansma concluded that the observed top-electrode shift resulted from a combination of hydrogen bonding, and the image dipole effect. Adkins and Sleigh on the other hand, concluded that the relative size of the top electrode shift and the polarity shift

FIGURE 3.13 Plot of the hydroxyl peak energy in Mg-MgO-Metal gun junctions verses the d character of the cover metal. Lower peak energies are observed in junctions where the cover electrode is more likely to bond with the hydroxyl.

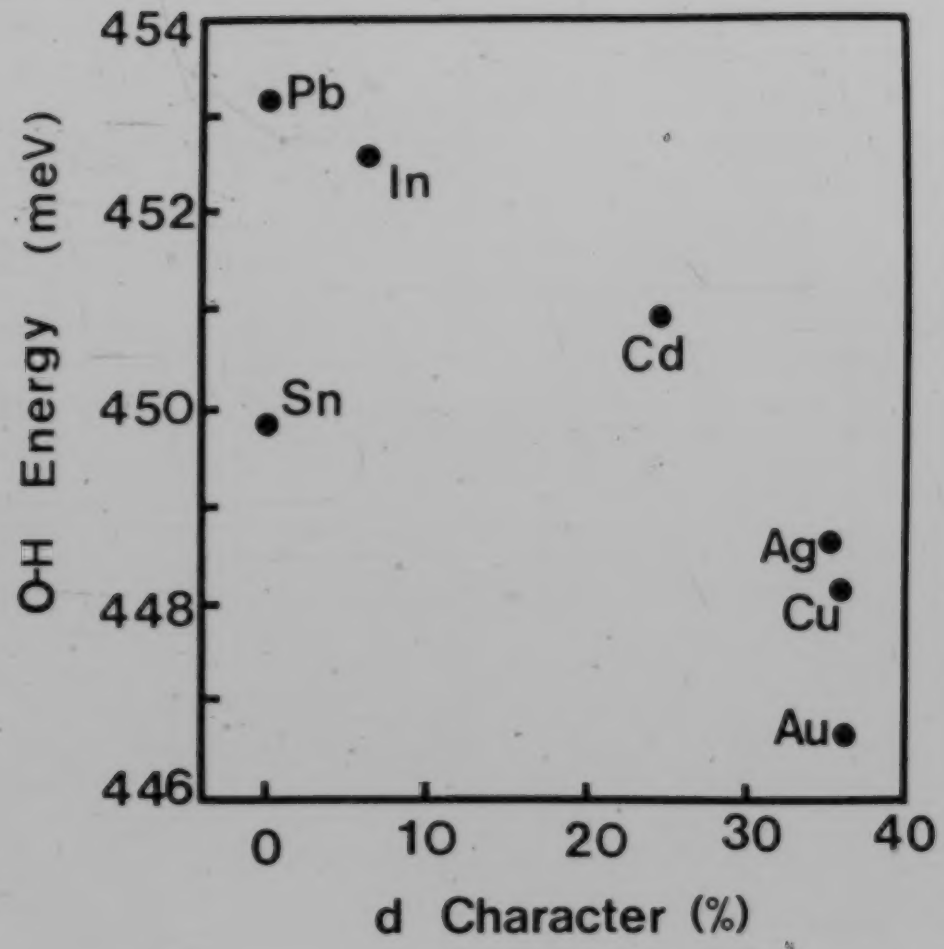
454
452
450
448
446
O-H Energy (meV)
Pb
In
Cd
Sn
Ag
Cu
Au
0
10
20
30
40
d Character (%)

indicates that contributions from hydrogen bonding may be ruled out. Using similar parameters, and by introducing the applied field, Adkins and Sleigh obtained a value of 1.1 meV for the polarity shift which is consistent with the observed value in the Al/AlO/Pb system (Reynolds et al., 1987). The sign of the shift observed in magnesium oxide junctions was consistent with the theoretical predictions of Adkins and Sleigh, however it was found that the size of the shift depended strongly on the cover metal. With Pb as the cover electrode the shift was about 1 meV in agreement with Reynolds et al. (1987), however Ag exhibited a shift of 9.5 meV. In general junctions with large cover electrode shifts exhibited large polarity shifts. Fig. 3.14 illustrates the polarity shift verses the cover electrode shift in gun junctions and the two effects appear to be related.

Though the model of Adkins and Sleigh (1987) seems consistent with the data in many respects, it is unable to explain the large variations in the size of the polarity shift with different cover electrodes. To explain this discrepency one can consider a distribution of O-H impurities throughout the oxide. The concentration of hydroxyl ions is largest at the cover electrode interface. Both the image dipole effect, and any chemical interaction are most prominent for impurities closest to the interface. For this reason, hydroxyl impurities located closest to the cover metal would have a lower vibrational energy than impurities in the interior. The vibrational frequency of hydoxyls at the surface of the oxide may be reduced further by an interaction between neighbouring impurities. Lippincott and Schroeder (1955) found that hydrogen bonding can occur between the H^+ and O^- of adjacent dipoles. This interaction weakens the existing O-H bond and reduces the vibrational frequency.

FIGURE 3.14 The difference in the observed hydroxyl peak energy for each polarity with respect to energy in the positive direction for various Mg-MgO-Metal gun junctions.

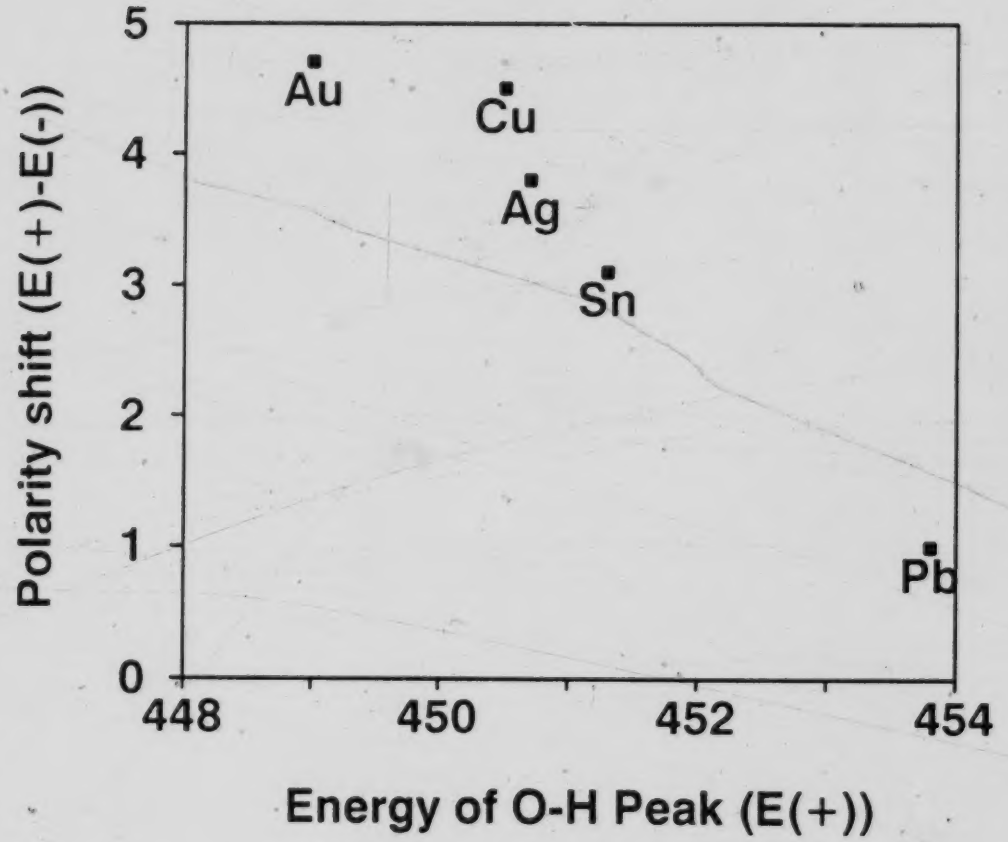
Polarity shift (E(+)-E(-))
5
4
3
2
1
0
Au
Cu
Ag
Sn
Pb
448
450
452
454
Energy of O-H Peak (E(+))

In a manner analogous to the discussion of the peak intensity, electrons tunneling out of the magnesium base electrode should excite impurities closer to the cover electrode interface. These impurities have a lower vibrational energy and in this way shift the peak to lower energies.

3.6.5 Summary

The technique of IETS has been used to investigate the effect of different preparation conditions on the tunneling characteristics of undoped Mg-MgO-metal tunnel junctions. Results indicate that the tunneling characteristics are related to the uniformity of the MgO layer.

Magnesium oxide is a crystalline oxide, and since granular oxides are full of pinholes and defects, the degree of crystallinity affects the tunneling characteristics. Junctions prepared in the dry system exhibited poor tunneling characteristics indicative of a patchy oxide. Junctions prepared in the wet system exhibited improved tunneling characteristics, indicating a more uniform barrier. Increased uniformity could also be attained by pretreating the Mg film with atomic hydrogen.

The pretreatment produced a peak in the IET spectra at 124 meV independent of cover electrode. Analysis of the vibrational energy, barrier parameters and isotopic substitution attributed the peak to hydrogen chemisorption at subsurface sites on the magnesium surface. MgO growth proceeds by island growth which nucleates at defects in the underlying magnesium film. The chemisorbed hydrogen acted as an additional nucleation site for initial oxidation, producing a more uniform oxide.

The additional uniformity of the gun oxide was quite apparent by observing the effect of different cover electrodes on the tunneling characteristics. It was observed that the size of the barrier was decreased by using cover electrodes with smaller ionic radii. Elements with small ionic radii penetrated into the barrier at pinholes and defects in the oxide. This effect was reduced in gun junctions, due to a smaller degree of imperfections. The increased uniformity proved to be essential in order to produce junctions with Al and Mg cover electrodes.

A shift in the 450 meV hydroxyl peak to lower energies was observed and attributed to the proximity of the hydroxyl to the cover electrode in agreement with Kirtley and Hansma (1976b). The size of the shift also depended on the direction of current flow. The peak shift was greater when electrons tunneled out of the base electrode. Cover electrodes which exhibited a larger shift generally produced a larger bias shift. The bias shift is believed to result from the fact that electrons tunneling out of the Mg are more likely to excite hydroxyls closer to the covermetal where the shift is larger.

4 Low Temperature Scanning Tunneling Microscopy and Spectroscopy.

Scanning tunneling microscopy (STM) was developed by Binnig et al. (1982a, 1982b) at IBM Zurich. The technique exploits the principles of electron tunneling to obtain a three dimensional map of a surface on an atomic scale. The work was based on the work of Young et al. (1971,1972) who's Topographiner provided the first example of vacuum tunneling. With the STM Binnig and coworkers reported the observation of atomic scale topography on semiconductor surfaces (Binnig et al., 1983a), reconstructed metal surfaces (Binnig et al., 1982a; 1983b) and chemisorbed molecules (Baró et al., 1984). These reports created a lot of excitement in the physics community culminating in 1986 with Binnig and Rohrer being awarded a share of the Nobel Prize.

The principle of operation involves bringing a fine probe, or tip, to within a few tens of Ångstroms of the sample surface and monitoring the resultant tunnel current. A feedback system is used to maintain a constant tunnel current, and thus separation, as the probe is rastered across the surface. By recording the feedback signal as a function of both X and Y position, a three dimensional image of the surface may be constructed (Fig. 4.1).

Although initially limited to a few groups with working microscopes, STM has grown to become a viable technique in a wide variety of physical, chemical, and biological problems (see for example Proceedings of STM 88 in J. of Microsc. 152, 1988).

This portion of the thesis describes the development and use of a low temperature STM. Low temperature STM was first demonstated by de Lozanne et al. (1985), who measured the spatial variation of the superconducting energy gap in

FIGURE 4.1 By applying a voltage and monitoring the resultant tunnel current, the separation between the sample and tip is kept constant. By rastering the tip across the sample, a three dimensional map of the surface may be constructed.

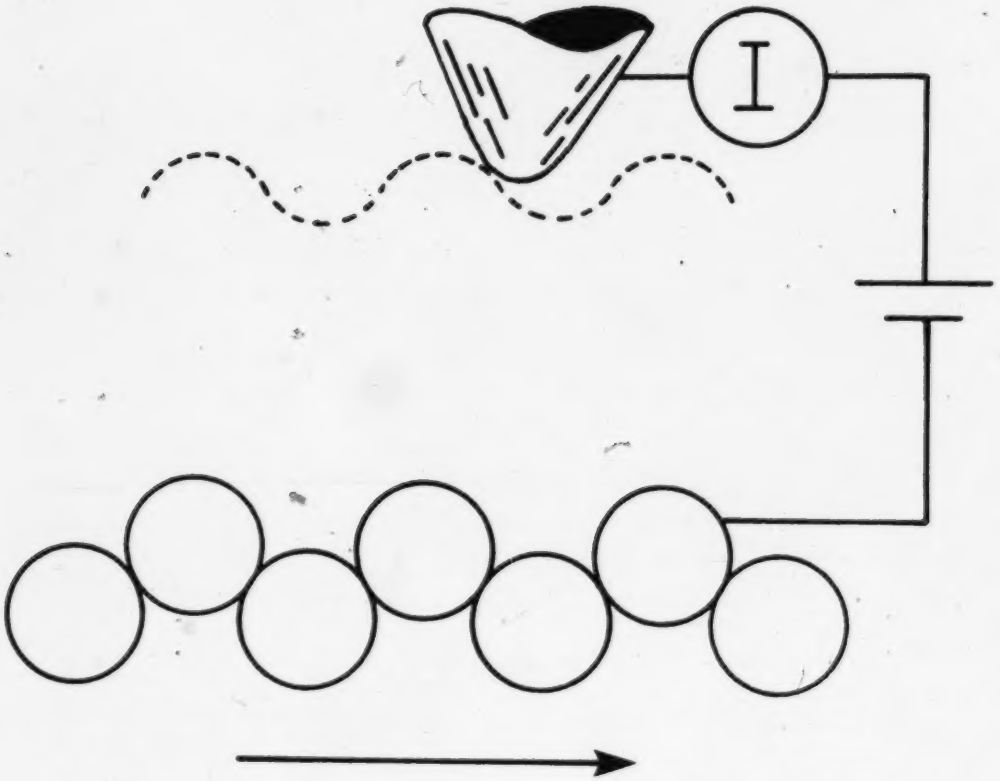
I
scan

Nb_3Sn at 4.2 K. This thesis describes a series of measurements performed with a low temperature STM on a number of high temperature superconductors (Bednorz and Müller, 1986; Wu et al., 1987).

To introduce the concepts, the theory of STM is presented. Generalization of the transfer Hamiltonian technique (Bardeen, 1961) to STM was provided by Tersoff and Hamann (1983, 1985). This theory and further developments by Lang (1985, 1986) are discussed. Since the majority of measurements were made on superconducting samples, a brief overview of superconductivity and superconducting tunneling is given. The design, operation and calibration of the microscopes is outlined in section 4.3. The performance of the microscopes is demonstrated by topographic and spectroscopic measurements performed on $NbSe_2$. Finally the results of a series of measurements on a number of high temperature superconductors are discussed.

4.1 Theory of Scanning Tunneling Microscopy and Spectroscopy

Initially the experimental results were interpreted, simply by extension of the one dimensional tunneling problem. According to Simmons (1963a, 1963b), the current due to free electrons tunneling through a barrier of constant height ϕ is equal to

$$I \propto 1/d^2\{(\phi - eV/2)\exp(-A(\phi - eV/2)^{1/2}d) - (\phi + eV/2)\exp(-A(\phi + eV/2)^{1/2}d)\} \tag{4.1}$$

where d is the electrode separation, V is the bias potential between electrodes, and $A = 1.025(eV)^{-1/2}$ Å^{-1}. When the gap is small, as in STM, and the voltage $V << \phi$, the expression may be simplified to

$$I \propto (V/d)\exp(-2\kappa d) \tag{4.2}$$

where κ is defined as the decay constant and is expressed as $\kappa = \sqrt{2m\phi}/\hbar$.

Typically $\kappa = 1.0$ Å^{-1}, and in this case keeping I constant to within 2% is equivalent to a maintaining the separation constant to within 0.01 Å (Hansma and Tersoff, 1987).

The problem with traditional one dimensional theory is that there is no distinction between surface and tip. In STM this difference is crucial. Tersoff and Hamann (T&H) (1983, 1985) extended the transfer Hamiltonian method to three dimensions to treat tunneling between a sample and tip. T&H started with Bardeen's expression for the tunnel current (eq. 2.5), which at low temperatures, and voltages reduces to

$$I = \frac{2\pi}{\hbar} e^2 V \sum_{\mu,\nu} |M_{\mu\nu}|^2 \delta(E_\nu - E_F)\delta(E_\mu - E_\nu) \tag{4.3}$$

where μ and ν run over all states in the tip and the sample respectively. As Bardeen demonstrated the matrix element may be expressed as

$$M_{\mu\nu} = \frac{\hbar^2}{2m}\int d\vec{S}\cdot(\Psi_\mu^*\nabla\Psi_\nu - \Psi_\nu\nabla\Psi_\mu^*) \tag{4.4}$$

where the integral is evaluated over a surface within the barrier region. Calculation of the tunnel current becomes a matter of choosing the appropriate wavefunctions to describe unperturbed states in the both the sample and tip. T&H expanded the surface wavefunction into a form

$$\psi_\nu = \Omega_s^{-1/2}\sum_G a_G \exp\left[\left(\kappa^2 + \left|\vec{\kappa}_G\right|^2\right)^{1/2} z\right]\exp(i\vec{\kappa}_G\cdot\vec{x}) \tag{4.5}$$

which is a completely general expression for an electron in a periodic potential of reciprocal lattice vector $\vec{G}$ (for description of amorphous surfaces $\vec{G}$ is extended to infinity). κ is the decay constant of the wavefunction normal to the surface, $\vec{\kappa}_G = \vec{k}_{||} + \vec{G}$ where $\vec{k}_{||}$ is the surface Bloch wavevector, and Ω_s is the volume of the sample. Since the exact structure of the tip is in general unknown, T&H used a local spherical potential well to model the sharp tip, and assumed the wavefunction has the symmetric form

$$\psi_\mu = \Omega_t^{-1/2} c_t \kappa R e^{\kappa R}(\kappa\left|\vec{r} - \vec{r}_0\right|)^{-1} e^{-\kappa\left|\vec{r}-\vec{r}_0\right|} \tag{4.6}$$

where $\vec{r}_0$ is the center of the spherical potential well, and R is the radius of curvature of the tip. The factor c_t is a normalization term which depends on the geometry, and the detailed electronic structure of the tip, and on the boundary conditions. In general, c_t is close to 1. To make the analysis easier, the work function for both the

tip and sample were assumed to be the same. The symmetric form of ψ_μ implies an s type wavefunction, or zero angular momentum. In order to simplify determination of the matrix element $M_{\mu\nu}$ (eq. 2.6), the Fourier transform of ψ_μ was found, and expressed in a form similar to ψ_ν. Using this form the matrix element could be evaluated and was found to be

$$M_{\mu\nu} = \left(\frac{\hbar^2}{2m}\right)\frac{4\pi}{\kappa}\Omega_t^{-1/2}\kappa R e^{\kappa R}\psi_\mu(\vec{r}_0) \tag{4.6}$$

Summing over the states in the tip μ, the tunnel current may be expressed in the form

$$I = \frac{32\pi^3}{\hbar}e^2 V \phi^2 D_t(E_F) R^2 \kappa^{-1} e^{2\kappa R} \times \sum_\nu |\psi_\nu(\vec{r}_0)|^2 \delta(E_\nu - E_F) \tag{4.7}$$

$D_t(E_F)$ is defined as the density of states per unit area of the tip at the Fermi energy, and is a constant. The quantity $\sum_\nu |\psi_\nu(\vec{r}_0)|^2 \delta(E_\nu - E)$ is defined as the surface local density of states of the sample. The T&H result indicates that the tunnel current is proportional to the amplitude of the surface wavefunction evaluated at the center of curvature of the tip. T&H have shown that if the wavefunction of the tip is s like; i.e. l=0, then the tunnel current at a position $\vec{r}_0$, is proportional to properties of the bare surface local density of states.

If the tunneling tip is blunt, then states with non zero angular momentum become important. T&H (1983), and Lang (1985) found that only non zero angular momentum states with m=0 contribute appreciably to the tunnel current. Inclusion of these states result in only minor modifications to the final expression. States with

$m \neq 0$ have nodes oriented parallel to the surface and do not contribute to tunneling. In this manner, T&H theory should be equally valid for a sharp monatomic tip, or a tip with small cluster of atoms at the apex.

The expression for the current may be simplified further if typical metallic values are inserted. In this case the tunneling conductance reduces to

$$\sigma = 0.1 R^2 e^{2\kappa R} \rho(\vec{r}_0, E_F) \tag{4.8}$$

From the original form of $\psi_v(\vec{r}_0)$ it is easy to see that the conductance is proportional to $\exp(-2\kappa(R+d))$, where R+d is the distance between the sample and the center of curvature of the tip. The exponential dependence is in agreement with experimental observation, and simple one dimensional theory.

The treatment of T&H was extended by Lang (1985, 1986) to consider tunneling between a single atom tip and an atom on the surface. The model consisted of two metal electrodes each with an adsorbed atom on the surface. This model allowed Lang to consider real atom wavefunctions (Lang and Williams, 1978), instead of using a potential well to model the tip. By generalizing the transfer Hamiltonian formalism to obtain an expression for $j(\vec{r})$, Lang was able to subtract out the current contribution from the electrodes.

Neglecting the effect of the surface atom, the current density in the vicinity of the tip atom was a factor of 20 higher, than between two bare electrodes. This suggests that the majority of the tunnel current emanates from the atom at the apex of the tip and is relatively insensitive to the overall structure of the rest of the tip.

Lang's calculations of the tunnel current were performed for all values of angular momentum. In agreement with T&H (1983), he found that at low bias the

STM images the local density of states at the position of the tip. He also found that only states with m=0 (s, or p_z states) contributed appreciably to the current. Since the density of states will in general be different for different atoms, their apparent size in the STM image will be different. In the extreme case of a helium atom, Lang (1986) found that the tip actually moves towards the sample as it passes over the atom since the helium atom polarizes metal states away from the Fermi energy.

A similar effect may be observed by varying the tunnel voltage. The state density of the sample is in general energy dependent, therefore the observed size and corrugation depends on voltage. At some voltages the atoms may become invisible if the state density at this energy goes to zero.

In addition to providing topographic information, the STM can perform spectroscopic measurements on an atomic scale. Spectroscopy is performed by holding the tip stationary and measuring the tunneling characteristics. In the case of non zero voltage the T&H expression for the tunnel current becomes (Lang, 1986)

$$I \propto \int_{E_F}^{E_f+eV} dE \rho_T(E-V)\rho_S(\vec{r}_0, E) \tag{4.9}$$

The state density of the sample may be written in the form

$$\rho_S(\vec{r}_0, E) \propto \rho_S(\vec{x}_0, E) e^{-2\kappa s} \tag{4.10}$$

where s=R+d and the decay constant $\kappa = \sqrt{2(\phi - E) + V}$ is modified to include a non zero bias. In this form $\rho_S(\vec{x}_0, E)$ can be thought of as the sample state density in the plane of the surface. With the state density expressed in this form, the tunnel current takes the form

$$I \propto \int_{E_F}^{E_f+eV} dE \rho_T(E-V)\rho_S(\vec{x}_0, E) e^{-2\kappa s} \tag{4.11}$$

and the current is proportional to an integral over a product of tip and sample states weighted by a voltage dependent barrier penetration factor. Substituting the state densities for a number of different atom combinations, Lang calculated the voltage dependent tunneling characteristics between a monatomic tip and a single atom on the surface. He found that peaks in dI/dV occur at energies corresponding to resonances in either the sample or tip state densities. To perform spectroscopic measurements it would be desirable to minimize tip effects, and use a tip with a relatively featureless state density. In practice this is often achieved by using a blunt tip (Feenstra, Strosico, and Fein, unpublished).

Blunt tips are also advantageous for spectroscopy in another respect. For sharp tips the uncertainty relation can impose a limit on the energy resolution. The relation requires that $\Delta k \Delta x \sim 1$, therefore a 2 Å radius tip limits momentum resolution to 0.5 $Å^{-1}$ (Kuk and Silverman, 1989). For topography the sharper the tip the better the resolution, thus it would seem that the two procedures require different tips.

T&H (1983) have examined the properties of the surface density of states, $\rho(\vec{r}_0, E)$ to obtain some results concerning topographic resolution with the STM. Due to the decay of the surface wavefunction, at sufficiently large separations $\rho(\vec{r}_0, E)$ is rather smooth. The constant current contour is almost sinusoidal, and only the first order Fourier components are needed to describe the image. In other words,

$$\rho(\vec{r}_0, E_F) = \rho_0(z, E_F) + 2\rho_{G_1}(z, E_F)\cos(\vec{G}_1 \cdot \vec{x}) \qquad (4.12)$$

$\rho_0(z, E_F)$ is dominated by states at the center of the Brillouin zone since states with $\kappa_G \neq 0$ yield the longest decay length. Likewise states with $\vec{k}_{||} = \frac{1}{2}\vec{G}_1$ yield the longest decay length for the $\rho_{G_1}(z, E_F)$ component which is given by

$$\frac{d\ln[\rho_{G_1}(z, E_F)]}{dz} = 2\left(\kappa^2 + \frac{1}{4}G_1^2\right)^{1/2} \approx 2\kappa + \frac{1}{4}G_1^2/\kappa \tag{4.13}$$

If the extreme values of the contour occur at z_+,and z_-, the corrugation amplitude may be defined as $\Delta = z_+ - z_-$. The decay of the zero order term $\rho_0(z, E_F)$ is dominated by the inverse decay length κ^{-1}, therefore

$$\rho_0(z_+, E_F) \approx e^{-2\kappa\Delta}\rho_0(z_-, E_F) \tag{4.14}$$

Using the original definition of $\rho(\vec{r}_0, E)$ this equation can be rearranged to yield

$$e^{-2\kappa\Delta} \approx \frac{\rho_0(z, E_F) - 2\rho_{G_1}(z, E_F)}{\rho_0(z, E_F) + 2\rho_{G_1}(z, E_F)} \tag{4.15}$$

Where z is some average value between z_+ and z_-. Within the limit of small corrugation this expression can be simplified to yield the final result

$$\Delta \approx 2\kappa^{-1}e^{-\beta z} \tag{4.16}$$

where

$$\beta = 2\left(\kappa^2 + \frac{1}{4}G_1^2\right)^{1/2} - 2\kappa \approx \frac{1}{4}\frac{G_1}{\kappa}$$

Thus T&H (1986) found that the amplitude the of corrugation decreases exponentially with distance, and that the rate of decay is quite sensitive to the

surface lattice constant. If the unit cell is large then features within cell may be well resolved i.e. Si 7x7 (Binnig et al., 1983a). The exception to this are materials where the Fermi surface collapses to a point at the corner of the surface Brillouin zone. In this case the STM image results from an individual state and gives rise to a large corrugation with the periodicity of the unit cell. Tersoff (1986) suggests that such a mechanism may be responsible for the so called "giant corrugations" observed on graphite.

The results of T&H may be used to express an effective real space resolution for the STM. The corrugation decays at a rate given by the decay length β. This is equivalent to averaging over a Gaussian resolution function with an rms width $W=(z/2\kappa)^{1}/2)^{1/2}$ (T&H, 1985). Since z=R+d, for a blunt tip R>>d, and the resolution is determined by the tip radius. For a single atom tip the resolution is limited by d. At a seperation of 5 Å a resolution of approximately 1.6 Å can be expected.

Often the quantity of interest is the ability of the microscope to detect atomic corrugations of a relatively close packed surface. This depends on both the resolution and the noise level. To detect atoms separated by a lattice constant a, the signal should be at least as large as the amplitude of the noise n_G. From the preceding discussion this means

$$\begin{aligned} n_G \leq \Delta &= 2\kappa^{-1}\exp[-zG^2/4\kappa] \\ &\approx 2\kappa^{-1}\exp[-G^2W^2/2] \end{aligned} \tag{4.17}$$

Written in another way the criterion is

$$a \geq [2\pi^2/\ln(2/\kappa n_G)]^{1/2} W \tag{4.18}$$

Thus a is the closest equivalent atoms may be and yet still detected. The result indicates that the sensitivity is directly proportional to the resolution function, and the sensitivity also depends on the noise level, however not as strongly.

In order to test the theory T&H calculated contours of constant state density for Au (110) 3x1 and 2x1 reconstructions to compare with experiment. The experimental data obtained by Binnig et al. (1983b) exhibited regions of 2x1 and 3x1 in the same image. T&H first obtained results for the 2x1 structure. By adjusting the radius of curvature of the tip the corrugation amplitude could be adjusted to agree with experiment. Using the same tip parameters, the corrugation amplitude for the 3x1 structure was calculated and found to be in agreement with experiment.

The T&H theory seems to yield a good quantitative understanding of STM within the context of nearly a complete ignorance of the tip. They found that the tunnel current is proportional to the surface local density of states at the position of the tip, and that the sensitivity depends strongly on the size of the unit cell. The lateral resolution can be related to the tip radius R and the gap distance d as $[(R+d)/2\kappa]^{-1/2}$.

4.2 Superconductivity and Superconducting Tunneling

Since the first tunneling experiments by Giaever et al. (1960a, 1960b), tunneling has proven to be the most direct probe of the superconducting state. Superconductivity was first discovered by Kammerlingh Onnes in 1911 when he observed that the electrical resistivity of Hg fell to zero below 4.2 K. Subsequently, numerous materials have been found to exhibit superconductivity at sufficiently low temperatures. In addition to infinite conductivity, superconductors exhibit remarkable magnetic properties. In weak magnetic fields a bulk superconductor acts as a perfect diamagnet, with zero magnetic induction in the interior. At a critical temperature T_c the specimen undergoes a phase transition from a state of normal electrical resistivity to a superconducting state. The specimen reverts back to it's normal resistive state if it is exposed to large magnetic fields, or if large currents are passed through the sample.

The superconducting state is known to be an ordered state of the conduction electrons. Electrons form bound Cooper pairs, despite the mutual Coulomb repulsion between them. The nature of this ordering was explained by the microscopic theory of Bardeen, Cooper, and Schrieffer (BCS) (1957). In the theory, the electron interaction is mediated by the lattice. The first electron polarizes the lattice, and excites a phonon, which is absorbed by a second electron. Since the energies of the two electrons are altered, the phonon exchange has the same effect as a direct interaction between electrons. If the change in energy of the electrons is less than the phonon energy, the interaction is attractive. The strength of the interaction

is maximized for electrons of equal and opposite momentum, and opposite spin. For the superconducting transition to occur the strength of the interaction must exceed the Coulomb repulsion.

In the BCS ground state, electrons in the vicinity of the Fermi energy condense to form Cooper pairs. The condensation reduces the total energy of the system and introduces a gap into the excitation spectrum. That is, excited states have an energy at least Δ above the ground state. The energy gap results in a BCS density of states of the form,

$$\begin{aligned} N(E) &= 0 && E < \Delta \\ &= N_0 \left\{ \frac{|E|}{(E^2 - \Delta^2)^{1/2}} \right\} && E > \Delta \end{aligned} \tag{4.19}$$

where N_0 is the normal density of states at the Fermi energy.

It is this quantity which may be measured directly by elecron tunneling (Giaever, 1960a, 1960b). Giaever observed that when one electrode of a tunnel junction is in the superconducting state, the current voltage characteristics become distinctly nonlinear. At voltages less than Δ/e the junction is highly resistive and little current flows. At $V=\Delta/e$ there is a sharp current rise and higher voltages the curve approaches the normal state curve (Fig. 4.2).

In general the expression for the tunnel current between two metals may be expressed as (Giaever, 1960a, 1960b),

$$I(V) = G_{NN} \int_{-\infty}^{\infty} \rho_L(E) \rho_R(E + eV) [f(E) - f(E + eV)] dE \tag{4.20}$$

FIGURE 4.2 The quasiparticle tunneling characteristics for tunneling between a normal metal and a superconductor. The current is easily visualized by considering the semiconductor model and, how application of a bias V shifts the densities of states rigidly past each other. dI/dV is directly proportional to the density of states in the superconductor.

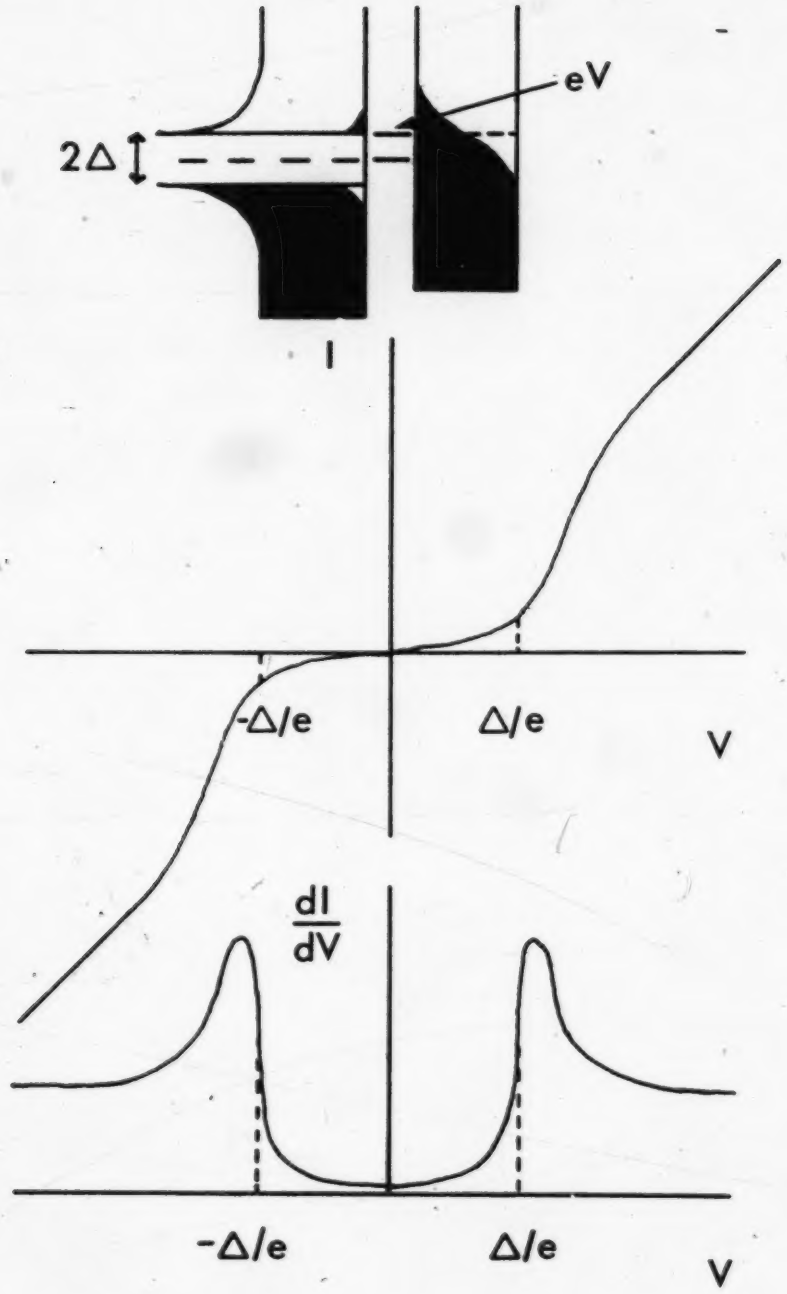
eV
2Δ
I
-Δ/e
Δ/e
V
dI/dV
-Δ/e
Δ/e
V

where $\rho_{L,R}$ are the density of states for the left and right electrode, and G_{NN} is the conductance of the junction in the normal state. If either of the electrodes becomes superconducting the density states term is replaced by N(E), or the quasiparticle density of states.

To visualize the current voltage characteristics Bardeen's semiconductor picture may be used. In this picture the density of states are split symmetrically about the Fermi energy. Application of a voltage V shifts the density of states rigidly past one another (Fig. 4.2).

In the N-I-S case, current below Δ/e arises only to the extent that there are thermally occupied states above the Fermi energy in the metal, and holes in the superconductor. At $V=\Delta/e$ there is a sharp rise in current, broadened by ~$3.5k_BT$ due to Fermi smearing. When $k_BT << \Delta$ the rise is quite sharp and may be used to locate Δ.

Giaever found that measuring the dynamic conductance, dI/dV as a function of voltage resulted in a curve directly proportional to the BCS density of states. Normalizing the data by using the normal state characteristics, tunneling measures the BCS density of states directly.

$$\frac{dI/dV_S}{dI/dV_N} = 0 \qquad E < \Delta$$
$$= \frac{|E|}{(E^2-\Delta^2)^{1/2}} \qquad E > \Delta \tag{4.21}$$

In this way tunneling provides a direct measure of the energy gap. BCS (1957) predicts $2\Delta/k_BT_c=3.53$ in the so called weak coupling limit. This limit is valid for most superconductors, however metals such as Pb and Hg exhibit ratios of 4.3 and 4.6 respectively, and are referred to as strong coupling.

In general, the agreement between experiment and the BCS expression is very good, however deviations are observed. The strong coupling materials exhibit the largest deviations from the theory. Deviations from the BCS expression indicate an energy dependent energy gap parameter $\Delta(E)$ (Eliashberg, 1960; Schrieffer et al., 1963; Rowell, 1969).

In BCS theory the electron electron interaction is assumed to be instantaneous, and non local. Moreover the interaction strength is assumed to be constant up to a cut off frequency given by the Debye frequency ω_D. To model the short range and retarded nature of the phonon interaction requires the Green's function formalism developed by Eliashberg (1960). Schrieffer, Scalapino and Wilkins (1963) used an effective phonon density of states and found that not only is the gap energy dependent, but it is complex. The corresponding tunneling density of states is,

$$N_T(E) = Re\left\{\frac{|E|}{(E^2-\Delta^2(E))^{1/2}}\right\} \tag{4.22}$$

Within the Eliashberg formalism, the energy dependence of the gap function contains detailed information about the interaction giving rise to superconductivity. Using a technique developed by McMillan and Rowell (1965), the tunnelling data may be inverted to obtain the electron phonon spectral function.

If we return to the general expression for the tunnel current (eq. 4.20) and consider the case of two superconducting electrodes, then each density of states term is replaced by the appropriate quasiparticle state density. In this case at T=0 there is

no current below $eV=\Delta_L+\Delta_R$, where an abrupt rise occurs. The rise is temperature independent since it corresponds to the crossing of the two singularities in the state densities. The rise acts as an extremely accurate measure of $\Delta_R+\Delta_L$. In the case of non zero temperature thermally activated quasiparticles produce a cusp at $\Delta_R-\Delta_L$ (assuming $\Delta_R \geq \Delta_L$). Provided the temperature is high enough that $\exp(-\Delta_L/k_BT)$ is appreciable this provides accurate determination of $\Delta_R-\Delta_L$ (Fig. 4.3).

One additional feature of tunneling between superconductors is the presence of a current at zero bias. The Josephson current (Josephson, 1962) results from tunneling of Cooper pairs driven by the phase difference between the superconducting wavefunction on either side of the junction. Although the pair tunneling is an effect of the same order as quasiparticle tunneling, the phase coherence is easily broken by thermal fluctuations and noise. For this reason the Josephson current is more readily observed in the weak barrier or point contact regime (Wolf, 1985).

Recently, superconducting tunneling has been demonstrated with the STM. de Lozanne et al. (1985) measured the spatial dependence of the energy gap at the surface of Nb_3Sn at 4.2 K. Similar measurements were obtained by Kirtley et al. (1987a) on NbN at 4.2 K in magnetic fields as high as 8 T. Le Duc et al. (1989) have successfully measured structure in the tunneling density of states related to the phonon spectra of Pb with a Au tip. Although these experiments were performed in the regime of weak coupling between the sample and tip, STM provides the additional capability of varying this coupling by adjusting the voltage to the Z piezo.

FIGURE 4.3 Tunneling between two superconductors. Both superconducting gaps may be determined from structure at the sum and the difference of the gaps.

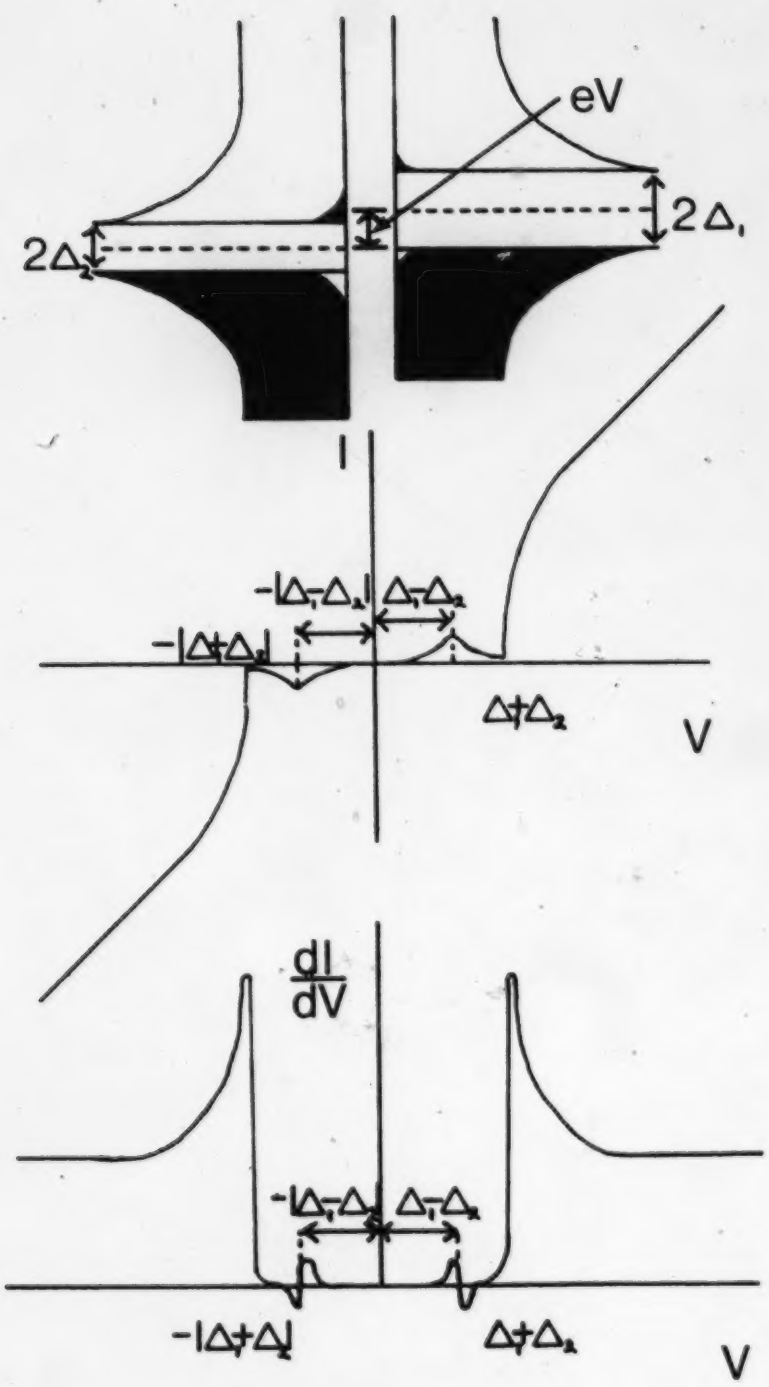
eV
2Δ1
2Δ2
I
-|Δ1-Δ2|
Δ1-Δ2
-|Δ1+Δ2|
Δ1+Δ2
V
dI/dV
-|Δ1-Δ2|
Δ1-Δ2
-|Δ1+Δ2|
Δ1+Δ2
V

Blonder et al. (1982) have developed a theory to calculate the tunnel current between a normal metal and a superconducting electrode as a function of barrier strength. The theory is valid over the entire range of coupling strengths from the tunneling regime to metallic contact. The authors treated the barrier as a perturbing potential which was inserted into the Bogoliubov equations (Bogoliubov, 1958), and used to determine the fraction and type of reflected particles as a function of energy and barrier strength.

For strong barriers the theory reproduces the traditional tunneling curves, while weaker barriers introduce modifications. As the strength of the barrier is reduced it is found that the probability of Andreev reflection (Andreev 1964) is increased. Andreev reflection, or quasiparticle injection, occurs at energies less than Δ/e when electrons impinging upon the interface from the normal metal reflect a hole of equal and opposite momentum back into the metal, and create a Cooper pair in the superconductor. In the extreme case of pure metallic contact, the probability of Andreev reflection approaches unity and as a result the current at energies less than the gap is twice that of the normal state (Fig. 4.4).

Fig. 4.5 illustrates examples of curves obtained in both the tunneling and point contact regime. The experimental curves were obtained on a Pb film using an STM. The coupling was modified by adjusting the voltage to the Z piezo. The I-V and dI/dV curve obtained on the surface of a ceramic $YBa_2Cu_3O_x$ sample (Fig. 4.6) also provides a clear example of Andreev refection. The curve indicates an energy gap $2\Delta \sim 10$ meV. The minima at zero bias results from a difference between the Fermi velocities of the superconductor and the PtIr tip (Blonder and Tinkham, 1983). The curves in the point contact regime provide a clear indication of superconductivity,

FIGURE 4.4 The I-V (a), and dI/dV-V (b) characteristics between a superconductor and a normal metal in the extreme case of no barrier. The resistance for energies less then Δ is reduced due to the increased probability of Andreev reflection.

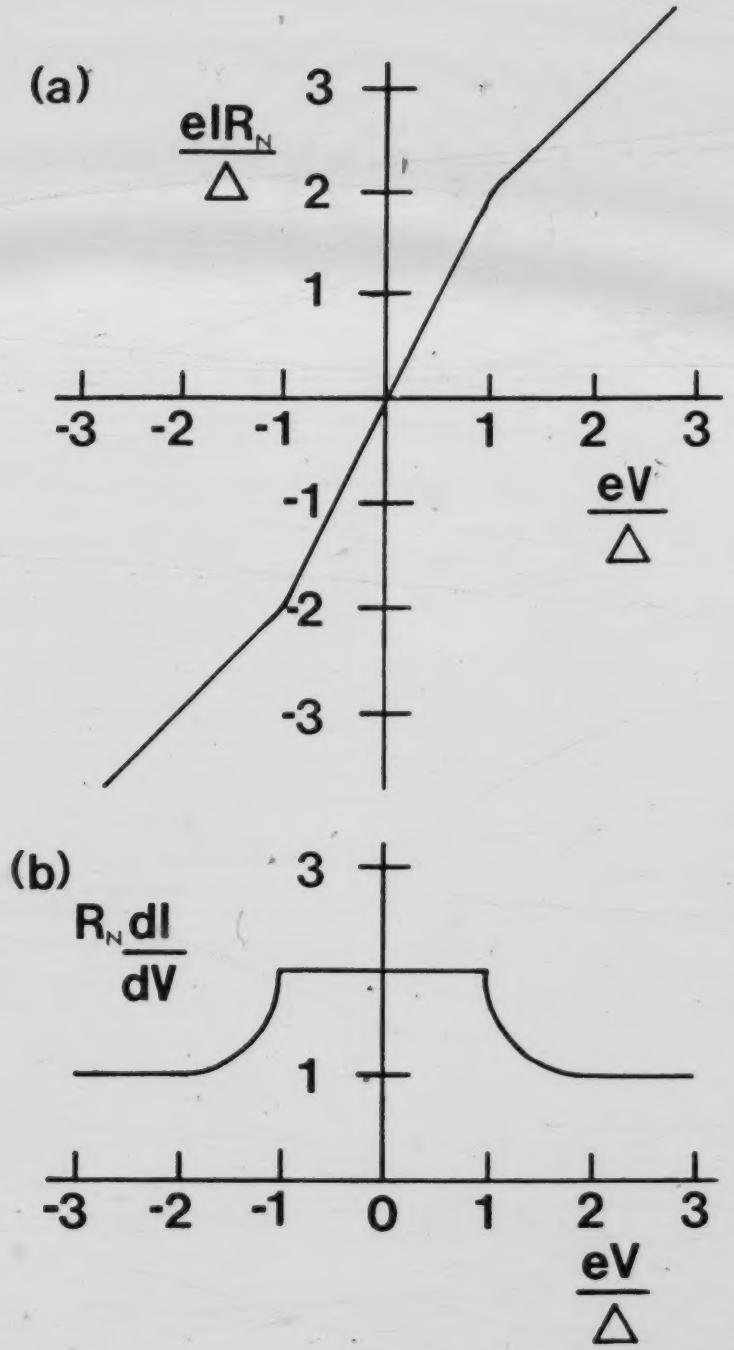
(a)
eIR_N / Δ
3
2
1
-1
-2
-3
-3 -2 -1 1 2 3
eV / Δ
(b)
R_N dI / dV
3
1
-3 -2 -1 0 1 2 3
eV / Δ

FIGURE 4.5 Current Voltage characteristics between a PtIr STM tip and a Pb film at 4.2 K. Curve (a) is obtained in the weak coupling regime and measures the quasiparticle density of states in the Pb film. Curve (b), obtained at a lower tunneling resistance, indicates strong coupling between the sample and tip and Andreev reflection.

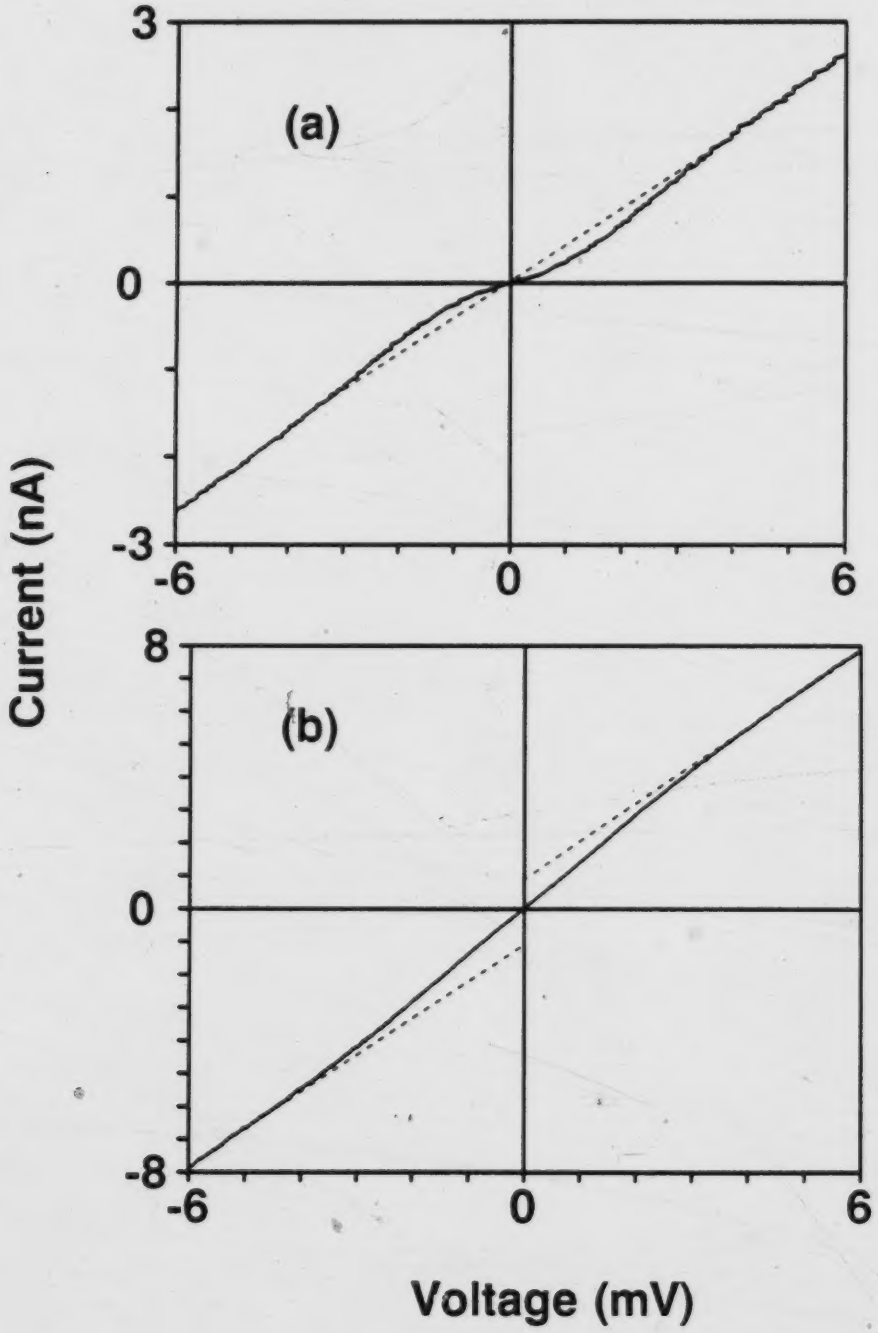
3
(a)
0
-3
-6
0
6
8
(b)
0
-8
-6
0
6
Current (nA)
Voltage (mV)

FIGURE 4.6 An example of Andreev strong coupling between a PtIr STM tip and a ceramic sample of $Al_{0.05}Y_{0.95}Ba_2Cu_3O_{6.5+x}$. The curve infers an energy gap of $2\Delta = 4.8$ meV.

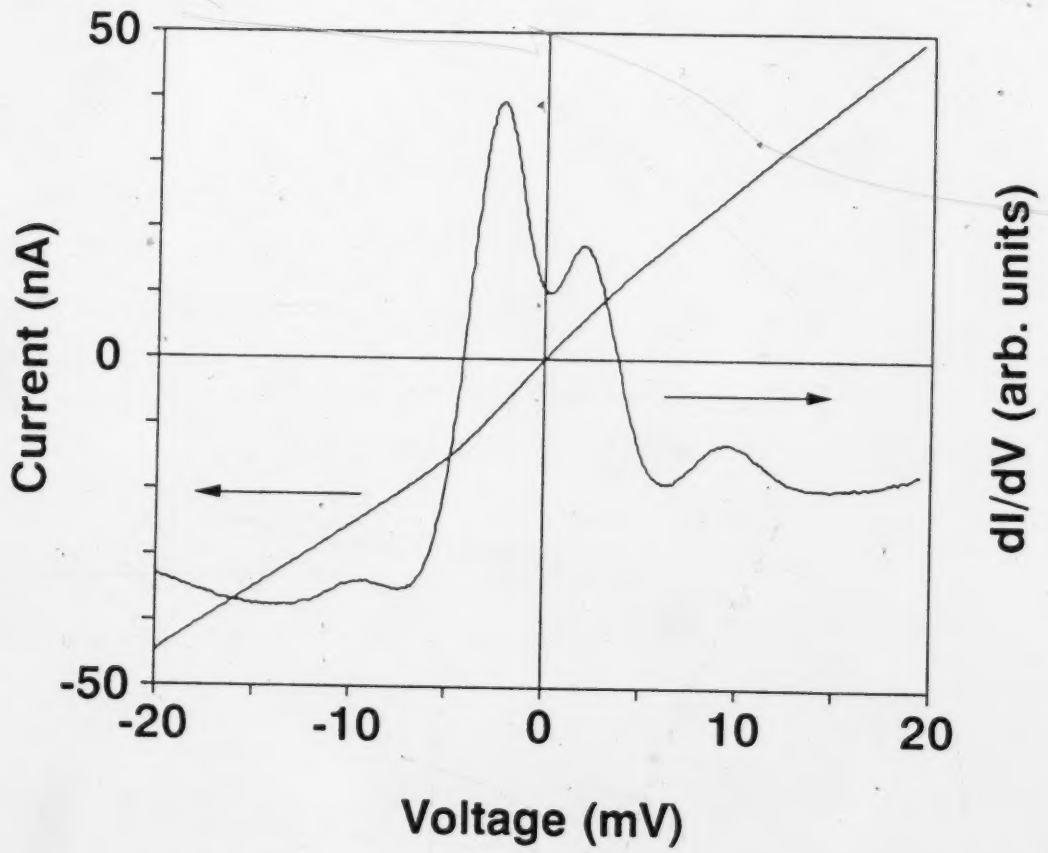
50
0
-50
Current (nA)
-20
-10
0
10
20
Voltage (mV)
dI/dV (arb. units)

and the distinctive shape means they are less likely to be confused with curves resulting from non superconducting behaviour such as charging effects (Giaever and Zeller, 1968).

In summary, tunneling can be used to measure the superconducting density of states. The energy gap value provides a measure of the strength of the interaction, and deviations from the BCS form can be inverted to provide detailed information about the interaction giving rise to superconductivity.

4.3 Experimental Techniques

4.3.1 Microscope Design

The principle of scanning tunneling microscopy is to bring a fine tip to within about 10 Å of the sample of interest, and use a feedback mechanism to keep the gap constant to within 0.01 Å, as the tip is scanned across the surface.

Both the scanning, and the Z feedback motion are achieved with piezoelectric actuators, which provide resolution of less than an Ångstrom in all three perpendicular directions. Piezoelectrics are ferroelectric materials which experience stress when exposed to an electric field. Depending on the direction of field the material will either expand or contract in order to reduce this stress. To a good approximation the amount of expansion is directly proportional to the applied field. To obtain the proportionality constant the actuators have to be calibrated against a grid of known spacing.

Two basic microscope designs were used for all our low temperature tunneling microscopy and spectroscopy experiments. The first was based on an instrument described by Drake et al.(1986), and modified to operate at low temperatures. The design uses a single piece of machined Channel 5400 piezoelectric ceramic[1]. The arms are poled to provide the X and Y motion for scanning (Fig. 4.7). The Z movement is provided by a bimorph disk, or two pieces of channel 5800 piezoelectric glued together. The behavior of the bimorph is illustrated in Fig. 4.7. When an electric field is applied across the disks, each disk is poled so that one expands while

1. Channel Industries Inc., 839 Ward Dr., Santa Barbara, Calif. 93111., U.S.A.

FIGURE 4.7 Piezoelectric transducers for the bimorph microscope. The X and Y motion are provided by single piece of Channel 5400 ceramic (a). The X motion is achieved by applying a voltage to the two parallel arms. The arms are poled in such a way (indicated in diagram) that one arm extends while the other contracts. Y motion is achieved by a single arm oriented perpendicular to the other two. The bimorph provides the Z motion. Application of a voltage to the bimorph contracts one disk and expands the other bending the bimorph.

(a)

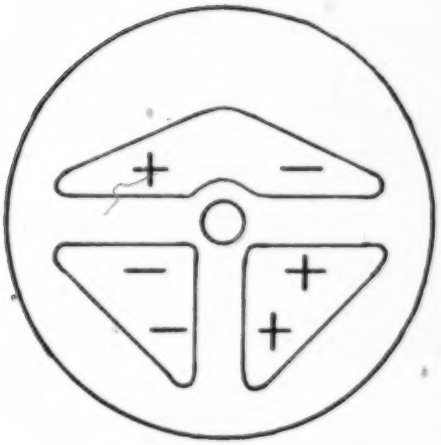

(b)

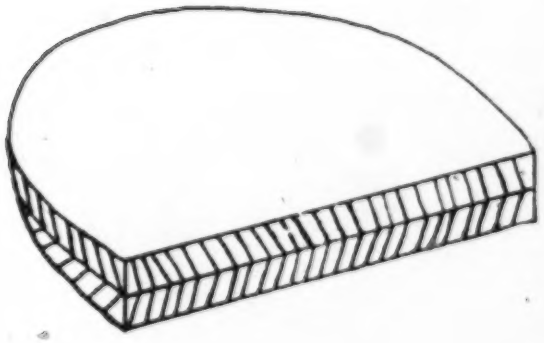

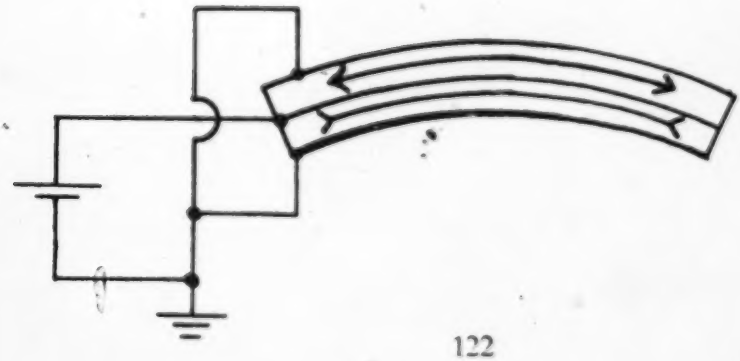

the other contracts. The resultant motion of the bimorph is to bend in a direction parallel to the applied field. It is this bending motion which provides the Z movement required for feedback.

The second microscope design utilizes a single piezoelectric PZT-5H tube. The single tube design was first proposed by Binnig and Smith (1986). The tubes are 0.5" long and 0.25" in diameter with a wall thickness of 0.020". Each tube is sectored to provide motion in all three X, Y and Z directions (Fig. 4.8). Incorporating the movement into one actuator adds stability to the microscope, and the compact nature of the tube increases the resonant frequency allowing more rapid scans. The main advantage of the tube compared with the bimorph microscope, is that for similar applied voltages it provides an order of magnitude larger field of view. The larger scan range is quite important at low temperatures where the peizoelectric effect is smaller. At 4.2 K, by applying voltages of 1000 V to both X and Y, the tube can scan an area of approximately 1x1 μm^2.

A critical aspect of any microscope design is the tunneling tip approach mechanism. The tip must be brought to within the dynamic range of the Z actuator with no risk of touching the sample. Any tip contact can degrade tip quality, and result in poor images. The bimorph microscope utilizes both a coarse and fine adjust mechanism to meet this requirement. The coarse approach is part of the tip mounting. The tunneling tip is inserted into a 26 gauge hypodermic needle, which provides a snug fit for the 0.01" diameter wire used for the tip (Fig. 4.9). To provide stability the hypodermic is crimped at the end closest to the tip. Next, the hypodermic is slipped inside a 0.080" stainless steel screw with the crimped end providing a secure fit. The screw is attached to the X-Y translator of the microscope

FIGURE 4.8 Movement of the tunnel tip (e), in the three orthogonal directions can be achieved by sectoring a single piezoelectric tube in the appropriate manner. X or Y motion is achieved by energizing either electrode (a) or (b) with respect to the ground electrodes (d), and Z motion is obtained by energizing the inner electrode (c).

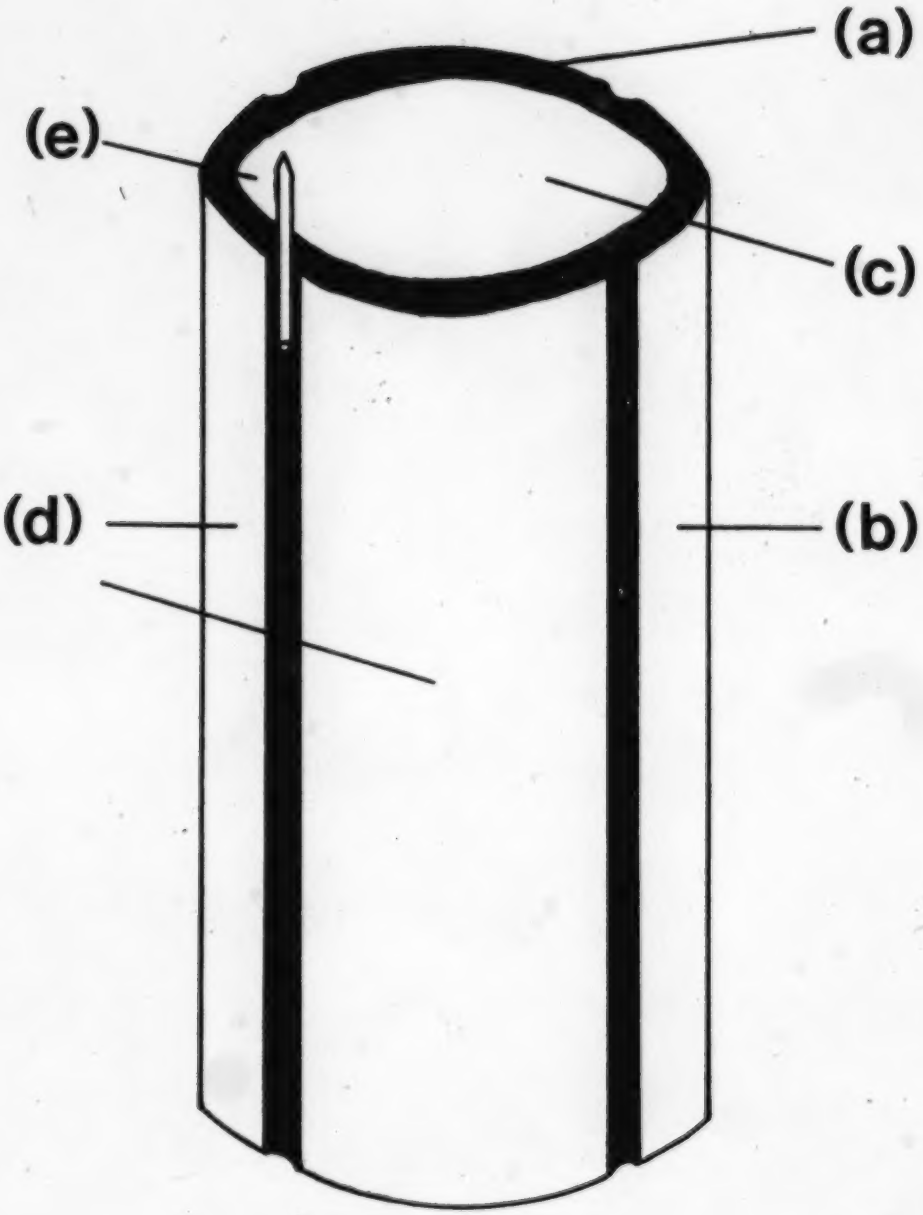
(a)
(e)
(c)
(d)
(b)

FIGURE 4.9 Schematic of the bimorph microscope: top view (i), side view (ii). (a) Brass fine adjust screw, (b) X-Y translator, (c) nylon collets, (d) coarse adjust spring, (e) hypodermic insert, (f) Macor body, (g) sample holder, (h) beryllium copper spring, and (i) bimorph.

(i)

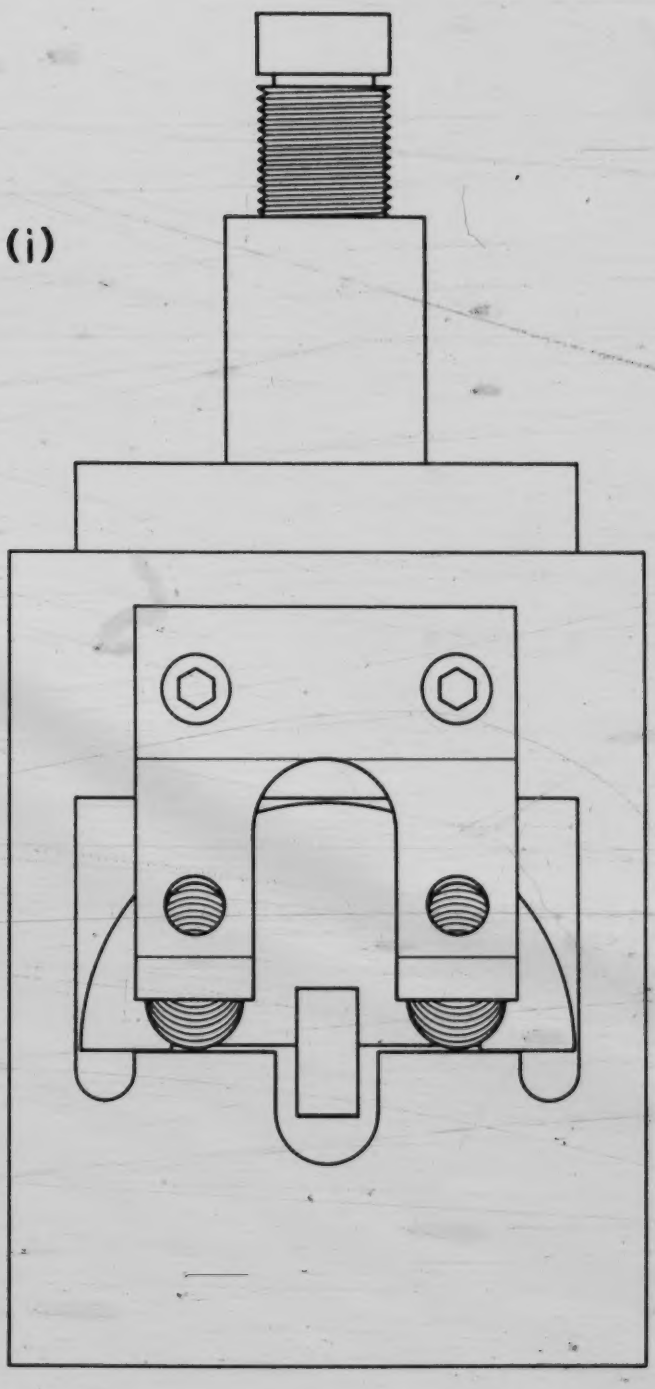

1 cm

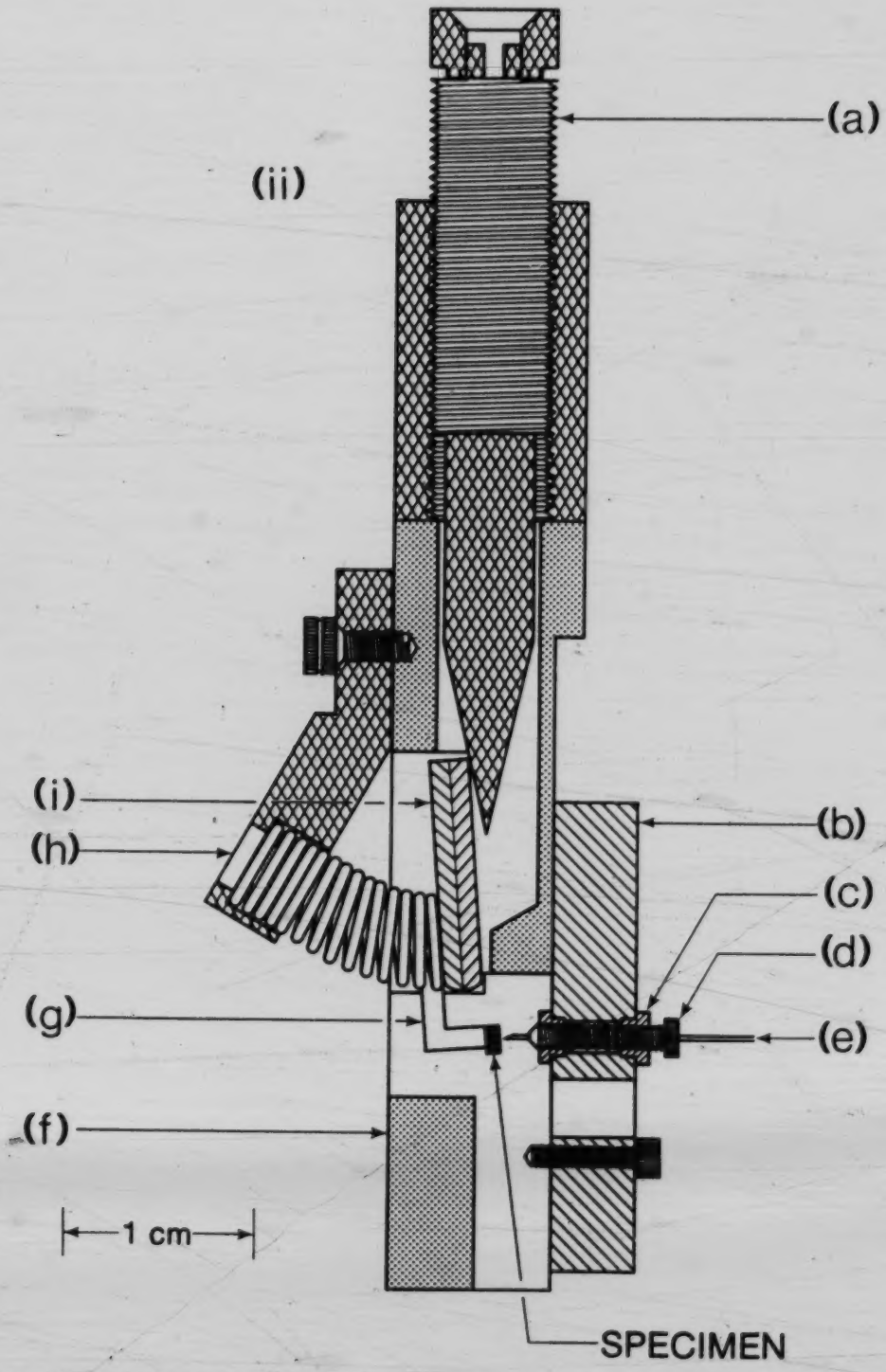
(ii)
(a)
(i)
(h)
(b)
(c)
(d)
(g)
(e)
(f)
1 cm
SPECIMEN

by two nylon collets. Coarse adjustment is provided by advancement of the 0.080" screw. The threading of the screw provides for an advancement of about 0.0125" per turn. The approach is monitored visually.

The fine approach uses a tapered screw to tilt the back of the bimorph disk. The screw is threaded at 80 threads per inch, which advances 0.0125" or 0.313 mm per turn. The angle of the taper is 13.4°, meaning one turn of the screw lifts the back of the bimorph 75 μm. The difference in the lever arms between the sample and the back of the bimorph provides for a mechanical disadvantage of 5 in movement. This means that the sample moves 15 μm towards the tip per turn of the tapered screw, and brings separation to within the dynamic range of the bimorph with no risk of contact.

The tube microscope also uses both a coarse and fine approach to provide tip approach (Fig. 4.10). The tip is mounted onto the tube which is in turn glued to a spring loaded pedestal. The pedestal may be moved towards the sample by adjusting two spring loaded 0.080" screws on either side of the pedestal. When tip is the desired distance from the sample, the pedestal is clamped to the body of the microscope for stability.

Fine approach is achieved with a differential spring arrangement. The mechanism is illustrated in Fig. 4.10. A screw threaded at 80 threads per inch pushes on a Beryllium Copper spring. The spring in turn pushes on a plunger which provides pressure to a Copper leaf onto which the sample is glued. The amount of force required to bend the leaf is larger than that required to compress the spring. It is this difference which provides the mechanical disadvantage required to bring the sample to within the dynamic range of the tube scanner without tip contact.

FIGURE 4.10 Tube microscope: (a) Macor body, (b) coarse approach pedestal, (c) fine approach screw, (d) beryllium copper spring, (e) ball bearing, (f) plunger, (g) copper leaf, (h) tube, (i) sample, and (j) tip.

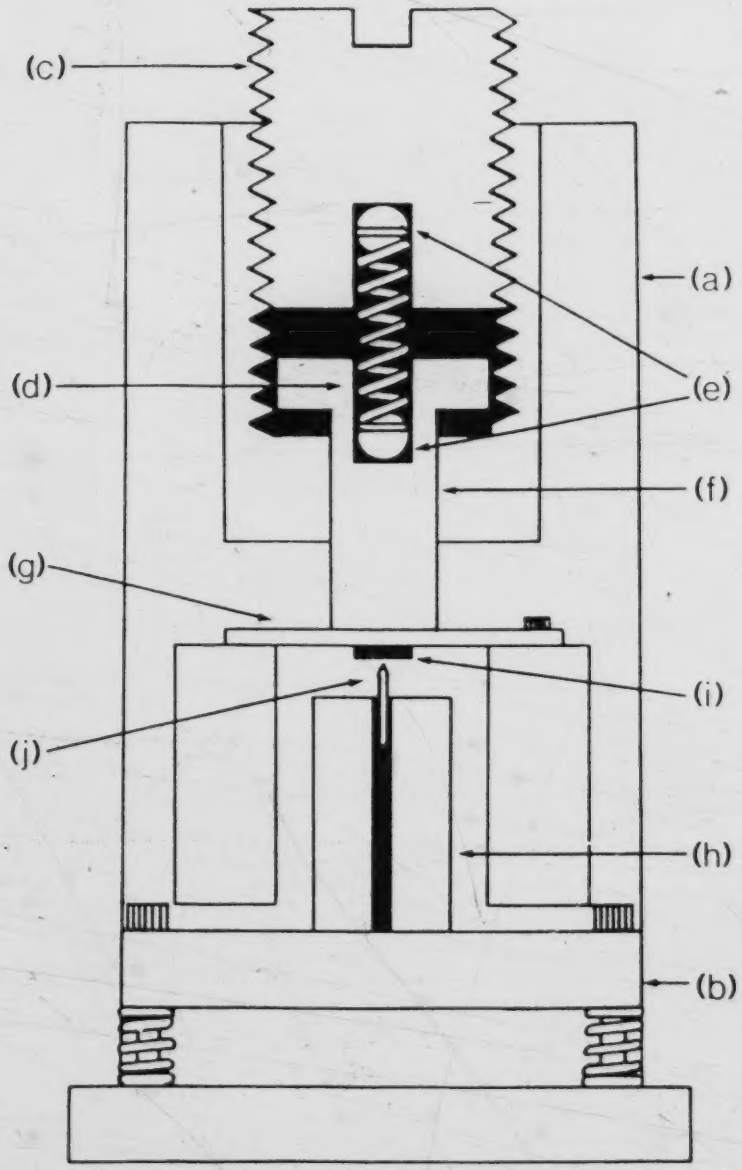
(c)
(a)
(d)
(e)
(f)
(g)
(i)
(j)
(h)
(b)

The bodies of the microscopes were constructed of Corning Macor. Macor, a machinable ceramic, provides rigidity, and has a low coefficient of thermal expansion, which is important when cooling the microscope to low temperatures. To provide ballast, the microscopes were mounted onto a Pb weight, and the weight was suspended from a brass cradle to provide vibration isolation. All the wires necessary for the peizoelectric movement of the microscope, and the current voltage measurement between the tip and sample, were attached by two Amphenol four pin connectors located on the top of the cradle.

To operate at low temperatures, the cradle was attached to a dipstick of approximately four feet in length, which allows the microscope to be inserted into low temperature dewars. The dipstick provides for electrical connections to the cradle, and enables remote operation of the fine adjust mechanism of either microscope. Both microscopes are oriented so that the fine adjust screw is concentric with the center of the cylindrical cradle. The dipstick and the cradle are constructed to allow a long screwdriver to be inserted down the inside of the stainless steel tubing of the dipstick, and operate the fine approach screw.

For added stability, and in particular to isolate the experiment from low frequency building vibrations, the microscope and the dewar are placed on an air table.

4.3.2 Experimental Setup

A schematic of the experimental setup for performing scanning tunneling microscopy and spectroscopy is shown in Fig. 4.11. A voltage v_0, which can range

FIGURE 4.11 Experimental schematic for Scanning Tunneling Microscopy and Spectroscopy experiments.

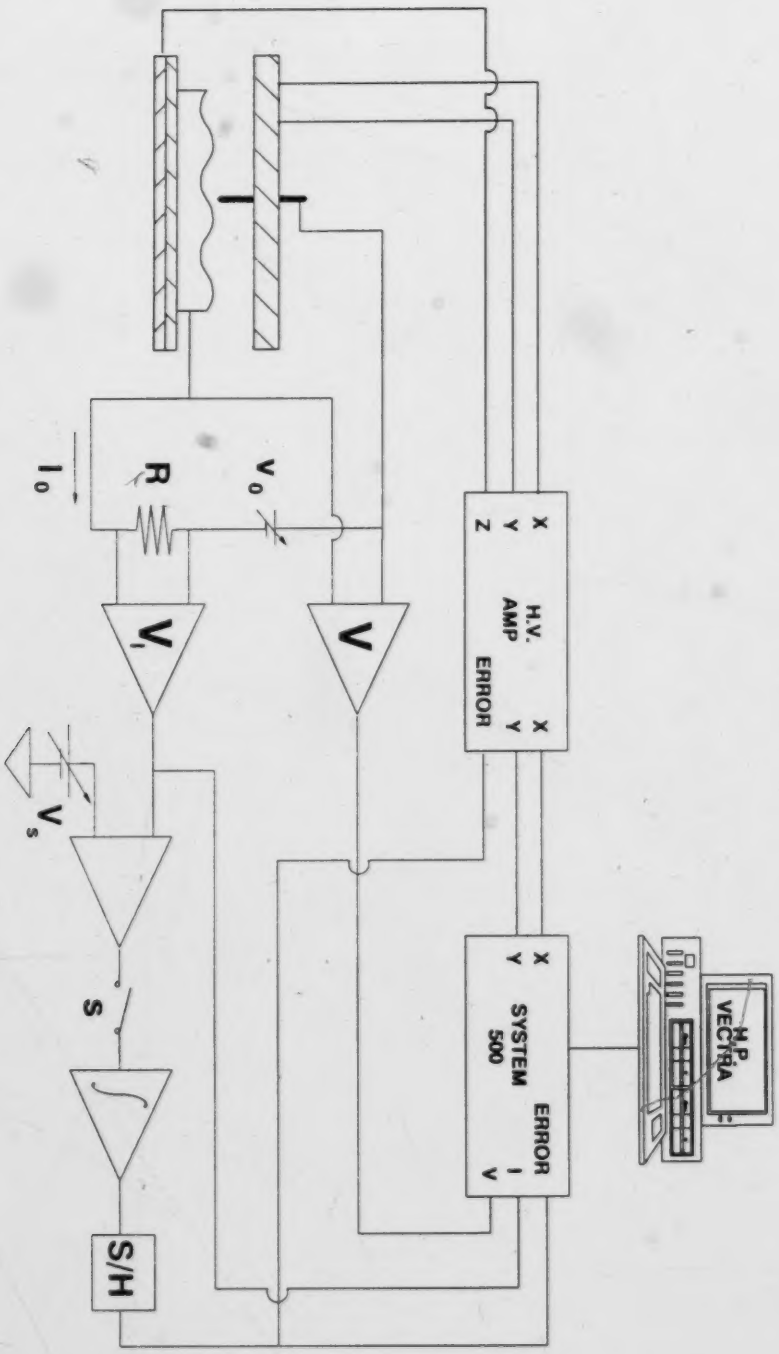
R
V_o
I_o
V_i
V
V_s
S
S/H
X
Y
Z
H.V.
AMP
ERROR
X
Y
X
Y
SYSTEM
500
ERROR
I
V
H.P.
VECTRA

from between a few millivolts to a few volts is applied between the sample and tip. When tip is within tunneling distance of the sample, the tunnel current i_0, is monitored by measuring the voltage drop across a series resistor R.

The voltage across the resistor V_I, is fed to the feedback electronics. The signal V_I is compared with a reference voltage V_S and the difference signal is sent to an integrator $\int$. The integrator provides an error signal which is sent to the high voltage amplifier. The error signal attempts to minimize the difference between the reference voltage and the current signal by correcting the tunneling distance appropriately. The exponential distance dependence of the tunneling current provides for remarkable stability. If the voltage V_I, and thus the tunnel current, is kept to within 1% of the reference voltage, this is equivalent to maintaining the separation constant to within 0.01 Å.

With the feedback maintaining a constant tunnel current, the tip is scanned over the surface to obtain the STM image. Data acquisition and control is provided by an XT compatible Hewlett Packard Vectra personal computer. The computer interfaces with the experiment via a Keithley Series 500 measurement and control system, which consists of a series of digital and analog input and output slots. The system is remotely located from the computer, and communicates via a connecting cable and interface card. The Series 500 is controlled by a number of Keithley supplied subroutines which may be called from Basic, C, and Pascal programming languages.

To produce a tunneling image, the tip is scanned laterally across the surface of the sample by rastering the X and Y Voltages to the appropriate X and Y piezoelectric actuators. The voltage values are output from the Keithley, amplified by the high voltage amplifier, and applied to the piezos. The output of the

integrator, or the error signal, keeps the tunnel current constant during scanning, and changes in the error signal reflect changes in the sample surface. By monitoring the error signal as a function of X and Y voltage, a three dimensional map of the surface may be constructed.

To obtain spectroscopic information the feedback loop must be interrupted. This is achieved by simultaneously opening switch s and activating the sample and hold module at the output of the integrator. With the feedback disabled, the tip remains stationary while the voltage between the sample and tip is ramped and the current voltage characteristics are measured. To ensure that any structure which may appear in the characteristics does not result from unwanted tip motion, the data is recorded for both increasing an decreasing voltages. In this manner the two curves may be compared for reproducibility. After the sweep, the voltage is returned to v_0, switch s is closed and the module is returned to the sample mode. Using this technique spectroscopy can be performed at various positions on the sample surface to provide spatial information.

4.3.3 Tip preparation

One of the keys to obtaining good quality tunneling images is satisfactory preparation of the tunneling tip. Resolution of a few Ångstroms requires an atomically sharp tip. The size, shape, and chemical identity of the tip will influence both the spatial resolution, and the measured tunneling characteristics. Tips were produced by grinding, electrochemical etching, or commercially prepared tips were used.

Nb tips prepared by etching proved successful in obtaining atomic resolution. The tips were prepared using an a.c. self-termination method (Jaklevic, private communication). The Niobium wire was placed in a 2 N NaOH solution, and an a.c. voltage of about 6 V was applied between the wire and a concentric copper tube. As the wire is etched away the solution eventually falls away from end of the wire, leaving a conical point. Inspection of these tips with a scanning electron microscope indicated that the apex was quite rough and possessed many microtips with radii of curvature of the order of 200 nanometers.

Attempts to produce W tips with a similar technique proved unsuccessful. Instead of obtaining conical points, the technique produced tips with a concave character and a high aspect ratio. Scanning tunneling microscopy with these tips were plagued with excessive vibrational problems.

Atomic scale topography was also obtained using ground tips of both W and Nb. The wires were ground on a dremel machine. The wire was slowly rotated while in contact with the dremel bit, until a conical point was produced. Although many of these tips produced the desired resolution, the reproducibility was not as high as with the etched tips.

In addition to producing tips, commercially produced PtIr tips of varying tip sizes were used with a large degree of success.

4.3.4 Calibration

In order to obtain meaningful tunneling images the movement of the piezoelectric actuators must be calibrated at low temperatures. To calibrate the X and Y motion highly ordered pyrolytic graphite was used as a calibration grid. Graphite is a layered material and is easily cleaved with adhesive tape. After

cleaving, the sample surface exhibits atomically flat regions of up to 1x1 μm^2. The carbon atoms are arranged in a honeycomb lattice with two inequivalent sites depending on whether or not the atom is located above a carbon atom in the second layer. The dominant feature of the tunneling image a deep depression at the center of each honeycomb ring resulting from the low electron density at this position (Fig. 4.12).

The periodicity of the graphite unit cell, and the large depression is 2.46 Å. Using this fact, atomic scale images of graphite could be used as an accurate calibration grid for the X and Y piezoelectric response. Atomic scale images were obtained at different X and Y voltages to ensure a good calibration over the entire range of each actuator. The microscopes were also thermally cycled a number of times during calibration to ensure reproducibility of the numbers.

The calibrated movement of each actuator proved to be a little different, yet the calibration for each remained constant. The translator in the bimorph microscope 04 for example, had an X sensitivity of 0.92 Å/V and a Y sensitivity of 0.63 Å/V at 4.2 K. These values varied by at most 3% with repeated measurement. The amount of crosstalk between X and Y movement due to nonorthogonal movement was extremely small and could be neglected in the calibration.

Calibration of the Z movement at low temperatures presented its problems. Attempts to observe atomic steps on gold proved unsuccessful. Gold is known to grow epitaxially when evaporated onto heated mica substrates if the temperature is above 250 ^{o}C (Reichelt and Lutz, 1971). Images obtained at low temperatures indicated the films were quite rough. It may be that the process of cooling these films to Helium temperatures produced enough stress to destroy the epitaxial surface

FIGURE 4.12 A perspective and topographic view of a graphite surface obtained at 4.2 K with a bimorph microscope using a ground W tip. The maxima in the image are spaced 2.5 Å apart (the periodicity of the graphite unit cell) and are used to calibrate the movement of the microscope.

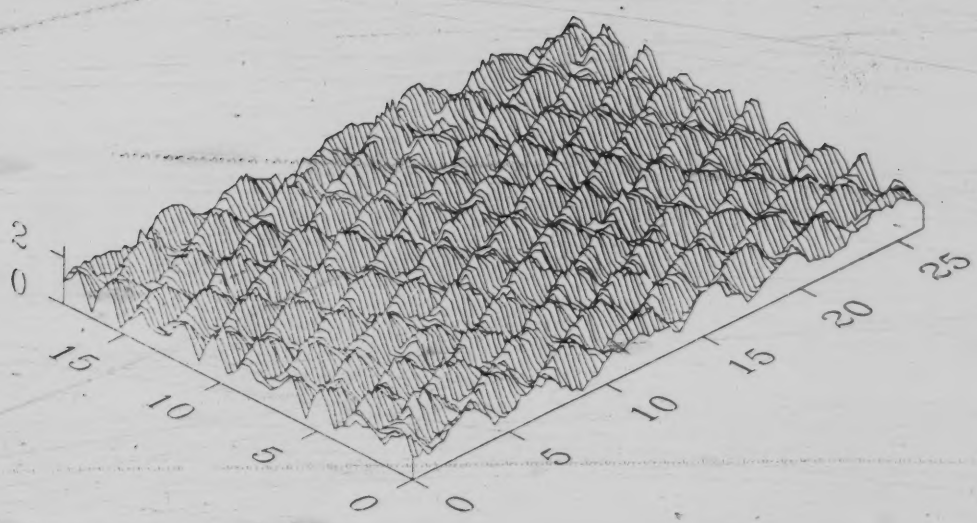
0
2
15
10
5
0
0
5
10
15
20
25

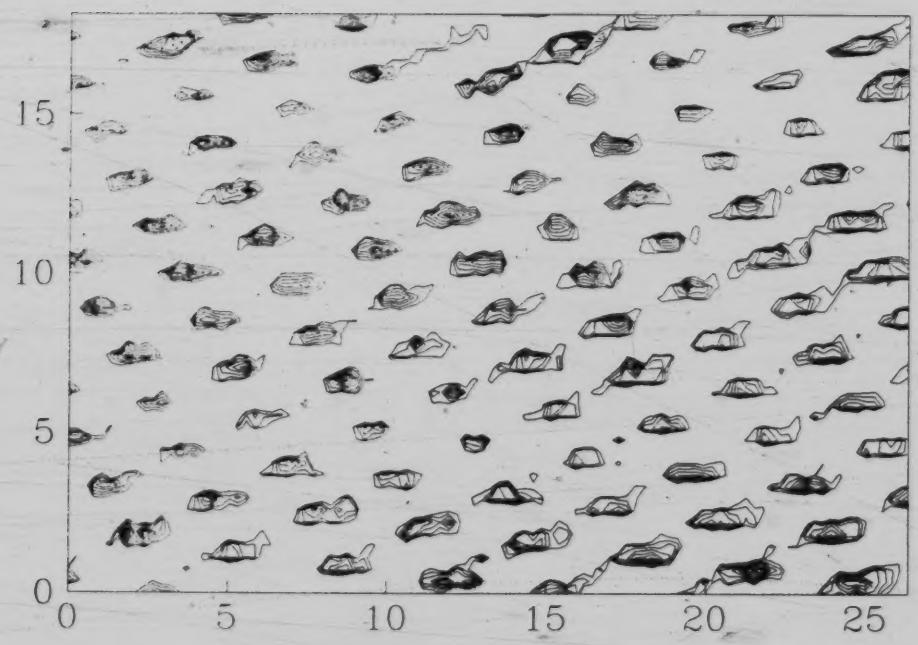
15
10
5
0
0
5
10
15
20
25

layer. Calibration was also attempted by growing Au (111) facets on a Au ball as described by Schneir et al. (1988). Although we did observe steps at room temperature we were unable to do so at low temperatures.

In the absence of any alternative techniques the bimorph was calibrated in the following manner. The fine adjust screw is known to move the sample 15 μm towards the tip per turn. With the feedback operating the fine adjust screw is advanced further to decrease the sample separation. The feedback responds by retracting the bimorph to maintain a constant tunneling current. By measuring the angle of rotation of the screw, and the change in voltage required to maintain the tunnel current, the Z sensitivity is calculated. The bimorph on microscope 04 yielded a calibration of about 16 Å/V.

The Z sensitivity of the bimorph was checked using an additional technique. The sample was mounted at an angle with respect to the X-Y translator. The angle was measured accurate to within a degree. By measuring the slope on the STM images and comparing this with the known angle of inclination, the Z response could be estimated. Numbers obtained in this way were similar to those obtained using the first method.

4.4 Experimental Results

4.4.1 Performance

To test the topographic and spectroscopic capabilities of the microscopes at 4.2 K, 2H-$NbSe_2$ was chosen as a substrate. Niobium diselenide is a layered transition metal dichalcogenide with a charge density wave transition at 33 K and a superconducting transition at 7.2 K, below which the two coexist.

$NbSe_2$ crystals grow as three atomic layers in a hexagonal close packed sandwich of Nb and Se atoms. In the 2H phase there are two sandwiches per unit cell, and each are separated by a Van der Waals gap. The Van der Waals interaction allows the sample to be cleaved easily like graphite. The fresh surface is atomically flat over regions as large as a micron, and remains stable in air.

A number of groups have imaged $NbSe_2$ with an STM. Bando et al. (1987) have imaged the lattice at room temperature, as did Coleman et al. (1988) at 77 K. Both Giambattista et al. (1988) and Hess et al. (1989) have imaged both the lattice and the charge density wave at helium temperatures. The STM image of $NbSe_2$ of consists of a hexagonal pattern of selenium atoms spaced 3.45 Å apart. Each maximum is surrounded by three minima, with 3 saddle points located above the Nb atoms in the second layer.

Fig. 4.13(b) is an STM image of $NbSe_2$ obtained at 4.2 K using a ground W tip. The selenium atoms are clearly visible. The image was obtained at 25 mV using a tunnel current of 2 nA. The size of the Z corrugation ranged from between 1.6 to 2.8 Å. This value is considerably larger than that observed by Giambattista et al. (1988), however consistent with the room temperature results of Bando et al. (1987).

FIGURE 4.13 A spectroscopic (a), and topographic image (b) obtained at 4.2 K with the STM using a ground W tip. Although substantially broadened, the current voltage curve does show evidence of a superconducting energy gap. The image clearly illustrates maxima corresponding to close packed selenium atoms spaced 3.5 Å apart.

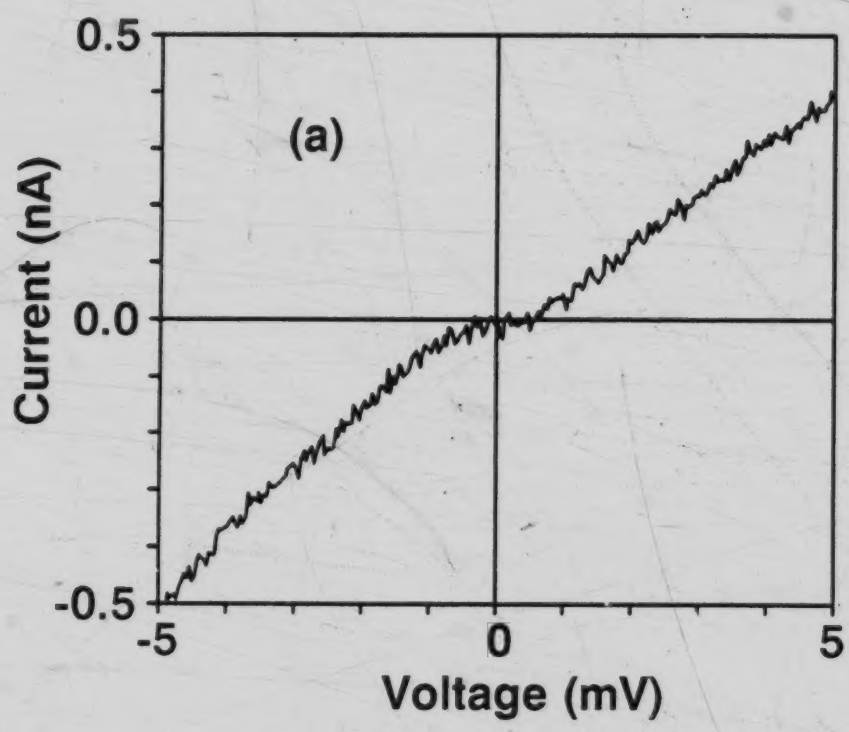
(a)
0.5
0.0
-0.5
Current (nA)
-5
0
5
Voltage (mV)

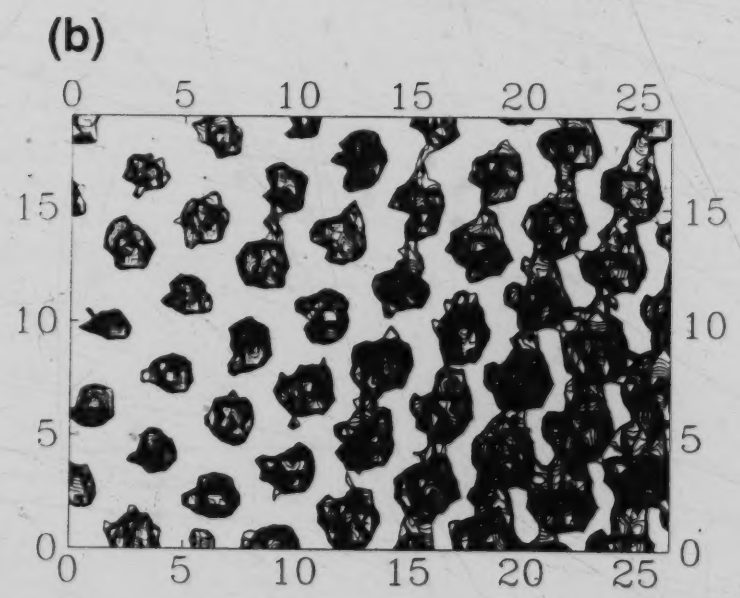
(b)
0
5
10
15
20
25

Unfortunately we were unable to observe the charge density wave modulation. Giambattista et al. (1988) found that under ideal conditions an additional modulation due to the charge density wave could be observed. Every third selenium atom appeared higher, translating into a CDW of wavelength ~$3a_0$. The total height variation associated with the CDW was only about 0.2 Å, making it hard to observe.

To test the spectroscopic capabilities of the microscope, the feedback loop was interrupted to measure the current voltage characteristics at different positions on the surface. Fig. 4.13(a) illustrates a current voltage curve obtained at one position. Although broadened, the curve does show evidence of an energy gap with a magnitude $2\Delta \approx 1.1$ meV. This value agrees with previous point contact measurements (Morris and Coleman, 1973), but is approximately half that reported by Hess et al. (1989). The excessive broadening evident in the curve may result from thermal effects, or from momentum resolution limitations imposed by the uncertainty principle (Kuk and Silverman, 1989).

The STM image and the current voltage curve indicate that the microscopes are capable of providing atomic resolution topography, while at the same time obtaining current voltage curves with millivolt resolution.

4.4.2 Scanning Tunneling Microscopy and Spectroscopy of High Temperature Superconductors.

Superconductivity in the copper oxide perovskites was first reported by Bednorz and Müller (1986). The authors observed superconductivity in the La-Ba-Cu-O system at temperatures in excess of 30 K. Subsequent work by a number of authors (Wu et al., 1987; Maeda et al., 1988; Sheng and Hermann, 1988) has led to a number of compounds with transition temperatures in excess of 77 K. The highest transition temperature is attributed to the compound $Tl_2Ba_2Ca_2Cu_3O_{10}$ (Torardi et al., 1988) with a transition temperature of 125 K.

Since the discovery of these materials there has been a great deal of work done to try and find the underlying mechanism behind this new class of materials. Central to this understanding, is the search for an energy gap. The vast majority of superconductors exhibit a gap 2Δ in the density of states at the Fermi energy. Within Eliashberg formalism (Eliashberg, 1960), the energy dependence of the gap can provide detailed information about the interaction giving rise to superconductivity (Schrieffer et al., 1963; McMillan and Rowell, 1965). The ratio of the gap to transition temperature provides a measure of the strength of this interaction, with the lower bound determined by the BCS (1957) weak coupling limit $2\Delta/k_bT_c=3.53$.

In conventional superconductors, tunneling has proven to be the most sensitive probe of the superconducting state. When tunneling between a normal metal and a superconducting electrode, the dynamic conductance of the junction is directly proportional to the quasiparticle density of states in the superconductor (Giaever, 1960a, 1960b).

This chapter describes the results of a series of experiments performed on a number of high transition temperature oxide superconductors using the low temperature scanning tunneling microscope. The measurements were performed to provide a better understanding of the superconducting properties of these materials.

Spectroscopic measurements of the tunnel current, and the dynamic conductance as a function of voltage were obtained for a number of ceramic, and single crystal samples to try and measure the energy gap. Large spatial variations in the tunneling characteristics were observed. The variation is attributed to the short superconducting coherence lengths in these materials, and problems related to the granular nature of the samples.

Simultaneous topographic and spectroscopic measurements were performed on a number of $YBa_2Cu_3O_x$ film samples. The measurements were used to provide information concerning the nature of the surface of these films.

Prior to a discussion of the experimental results, a brief introduction of the structure of the materials is presented.

4.4.2.1 Structure of the Oxide Superconductors

Measurements were performed on the $YBa_2Cu_3O_x$ (YBC) (Wu et al., 1987) system, and the Bi superconductor (Meada et al., 1988). Ceramic, single crystal, and thin film samples of YBC were measured, and ceramic samples of $BiSrCaCu_2O_x$.

The high T_c phase of YBC is an orthorhombic structure (Fig. 4.14), with two CuO_2 planes oriented parallel to the a and b directions, and one dimensional CuO chains running along the b direction. The orthorhombic distortion results from buckling of the CuO_2 planes.

FIGURE 4.14 Crystal structure of $YBa_2Cu_3O_7$ illustrating the CuO chains in the b direction and the CuO_2 layers in the a-b plane. The unit cell has a= 3.86 Å, b= 3.92 Å, and c= 11.84 Å (Pickett, 1989).

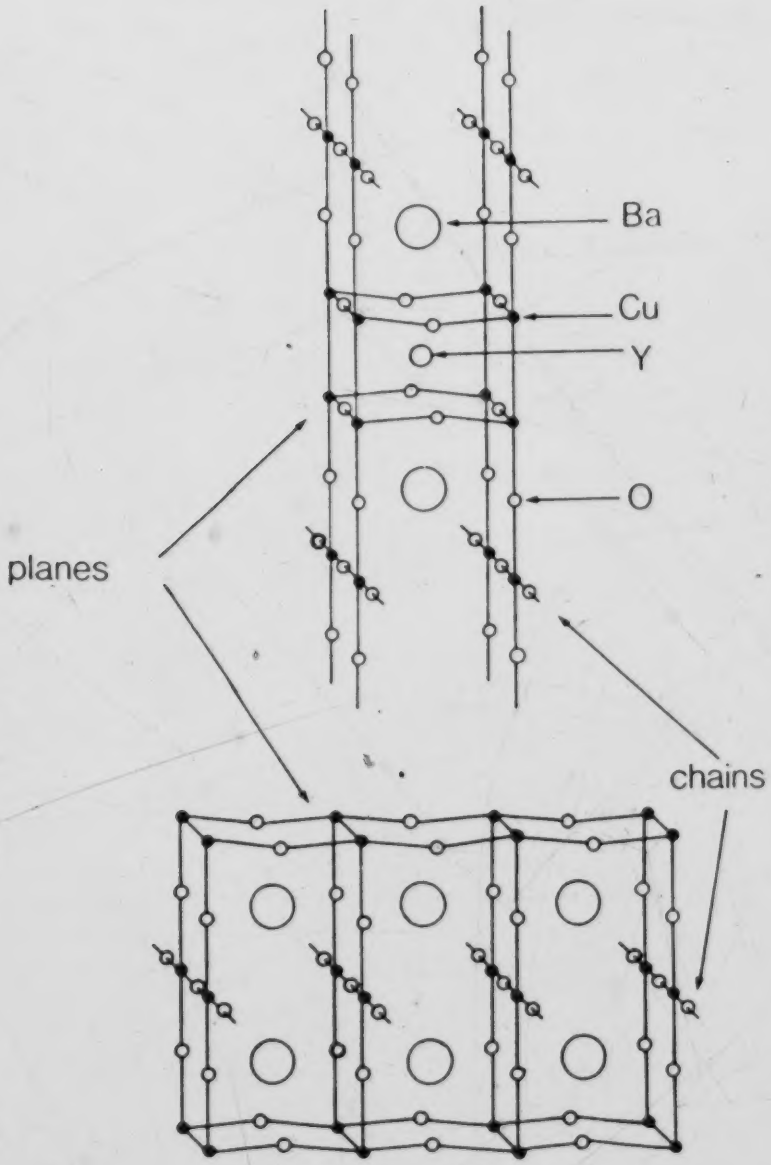
Ba
Cu
Y
O
planes
chains

The Bi-Sr-Ca-Cu-O compound has a number of superconducting phases, and each differ in the number of CuO_2 planes per unit cell. In both the Bi and Tl compounds, the transition temperature increases as the number of copper oxide planes is increased (Torardi et al., 1988). The crystal structure of the Bi material is described as a pseudo-tetragonal unit cell (Fig. 4.15), with a strong superlattice structure superimposed. The superlattice is due to a missing row of Bi atoms in the <110> direction every nine or ten atom distances (Kirk et al., 1988). The missing row reduces the lattice mismatch arising from the different Bi-O and Cu-O bond lengths.

Band calculations indicate that the majority of conduction electrons reside within the CuO planes in both these systems. The two dimensional nature of the planes results in highly anisotropic normal and superconducting characteristics (Gallagher, 1988).

4.4.2.2 Spectroscopic Measurements of the Ceramic and Single Crystal Samples

Both the bimorph and the tube STM were used to perform I-V and dI/dV-V measurements on a number of ceramic and single crystal samples of YBC, and on ceramic samples of Al doped $Y_{0.95}Al_{0.05}Ba_2Cu_3O_x$ (Al YBC) and $BiSrCaCu_2O_x$.

The purpose of the measurements was to probe the quasiparticle density of states in these materials in order to provide a measure of the energy gap. The experiments were also aimed at trying to understand the wide variation in the gap values reported in the literature. The results of tunneling measurements differ

FIGURE 4.15 The idealized unit cell of $Bi_2Sr_2CaCu_2O_8$ a= b= 3.82 Å and c= 30 Å (Tarascon et al, 1988). Not shown is the strong superlattice structure in the a-b plane (see text).

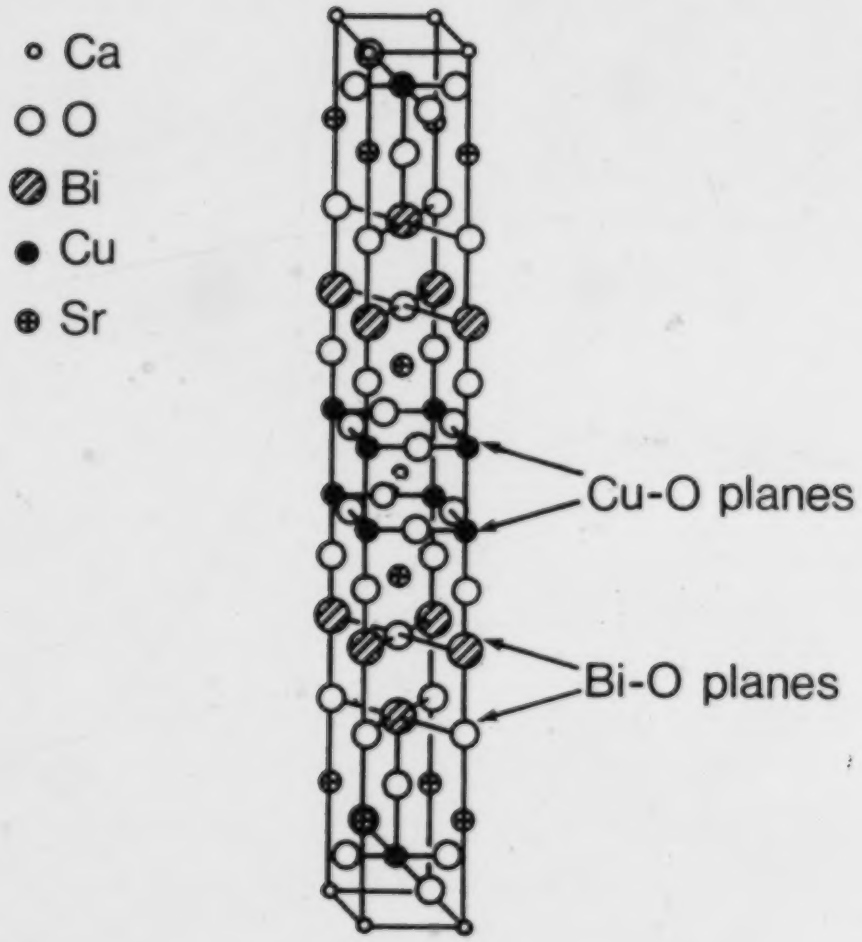
Ca
O
Bi
Cu
Sr
Cu-O planes
Bi-O planes

substantially from group to group. Values of $2\Delta/k_BT_c$ ranging from between 3 to 6 have been reported (Hohn et al., 1987; Koch et al., 1987; Moreland et al., 1987; Kirtley et al., 1988a; Sera et al., 1988; van Bentum et al., 1988a).

The YBC and the Al YBC ceramic samples were all single phase as determined by X-ray diffraction, and had zero resistance temperatures in excess of 88 K[1]. The resistive transition in these samples was quite sharp. The transition from 80% of the normal state resistance to 20% occurred in less than 2 K. The Bi sample had a T_c of 62 K and a transition width of about 5 K[1], and the single crystals had transition temperatures in excess of 85 K[2]. All the ceramic samples were inside edges of freshly broken pieces of sintered pellets. The samples were immediately mounted into the STM and cooled to 4.2 K, a process which took about one hour.

Attempts to obtain topographic data at 4.2 K on any sample proved unsuccessful. At resistances of much less than $10^8\ \Omega$ the tip tended to get stuck in some sort of insulating surface layer. Much of the spectroscopic data was obtained at resistances of about $10^6\ \Omega$, and at these resistances the tip was undoubtedly embedded within this nonconducting layer. The fact that the curves were produced with an embedded tip rather than vacuum tunneling enhanced junction stability, allowing the data to be obtained without feedback to the Z piezo. The presence of the surface layer also made it necessary to use the fine approach screw on the microscopes to back off and reapproach in order to study different positions on the sample. This made quantitative spatial analysis impossible.

---

1. Samples provided by J. Jung and J.P. Franck, The University of Alberta.
2. Samples provided by J.E. Greedan, McMaster University.

The curves were obtained by measuring the voltage directly across the junction, and using the voltage across a series resistor to monitor the current. In order to measure dI/dV a modulation voltage was superimposed onto the tunnel voltage. Using a lock in, dI/dV was obtained by measuring the phase sensitive signal across the series resistor. To obtain I and dI/dV simultaneously the tunnel junction was incorporated into one arm of an a.c. bridge. The curves were recorded using either the Keithley System 500 or a digital storage scope.

The tunneling curves obtained on all the samples exhibited large spatial variations between different spots on the surface. Many curves were relatively featureless and exhibited no signs of superconducting behavior, while others exhibited a wide range of apparent energy gap values. Fig. 4.16 is an example of three curves obtained at different locations on the surface of a ceramic Al YBC sample. Assuming the curves represent superconducting tunneling between the surface of the sample and the Nb tip, energy gap values of between 5 and 190 meV may be inferred. The characteristics were also found to depend strongly on the tunneling resistance. In many instances curves obtained at lower resistances exhibited an abundance of structure. The dI/dV curve in Figure 4.17 shows a series of symmetric maxima which occur at voltages $\pm V_0$, $\pm 3V_0$, and $\pm 5V_0$. Structure such as this is unrelated to superconductivity, but arises from the granular nature of the materials and the highly local probe being used to measure the characteristics.

Like curves 4.16(a) and 4.16(b), many of the curves which suggested the presence of an energy gap were of rather poor quality. The curves exhibited large leakage currents below the gap, and the current voltage characteristics outside the gap were non linear, and in general asymmetric. The exceptions were curves such as

FIGURE 4.16 I-V tunneling characteristics obtained at different positions on the surface of an aluminum-doped YBC ceramic. The curves were obtained at 4.2 K with a Nb tip. Note the different scales used for each curve.

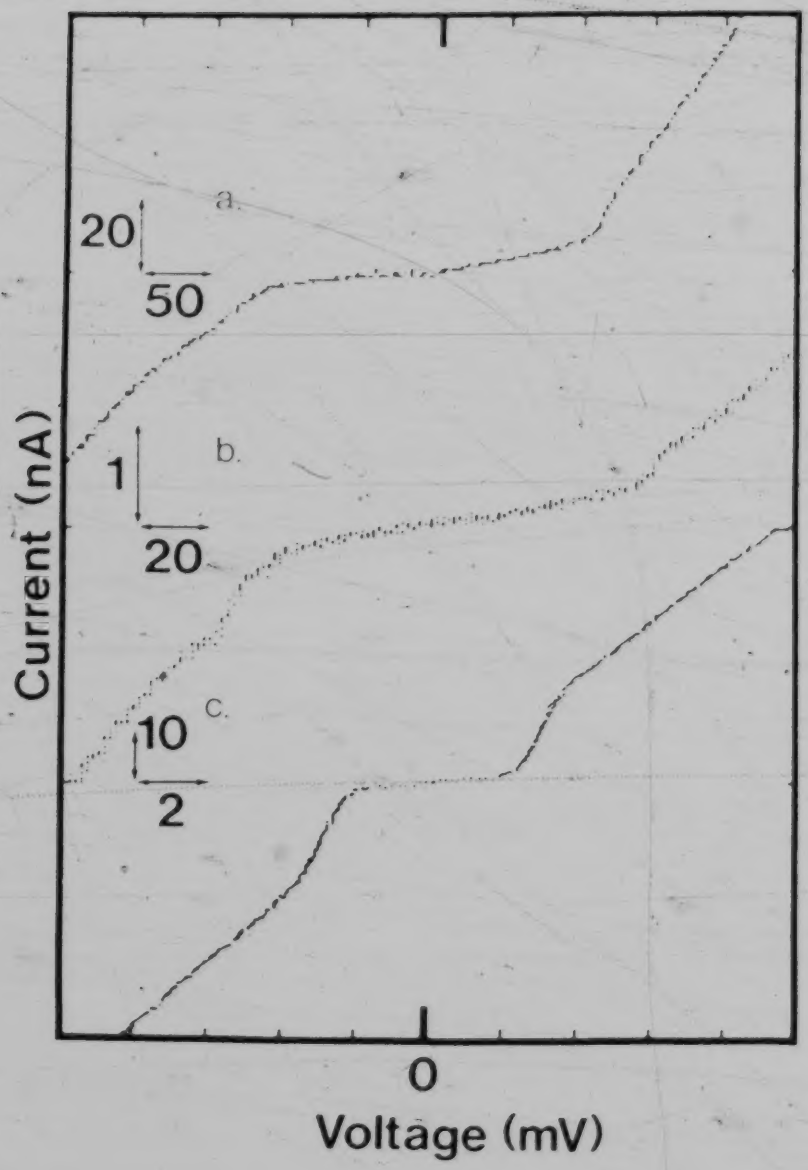
a.
20
50
b.
1
20
c.
10
2
Current (nA)
0
Voltage (mV)

FIGURE 4.17 I-V and dI/dV characteristics obtained on the surface of a $YBa_2Cu_3O_x$ single crystal using a W tip. The peaks in dI/dV provide evidence for tunneling into a small isolated particle on the sample.

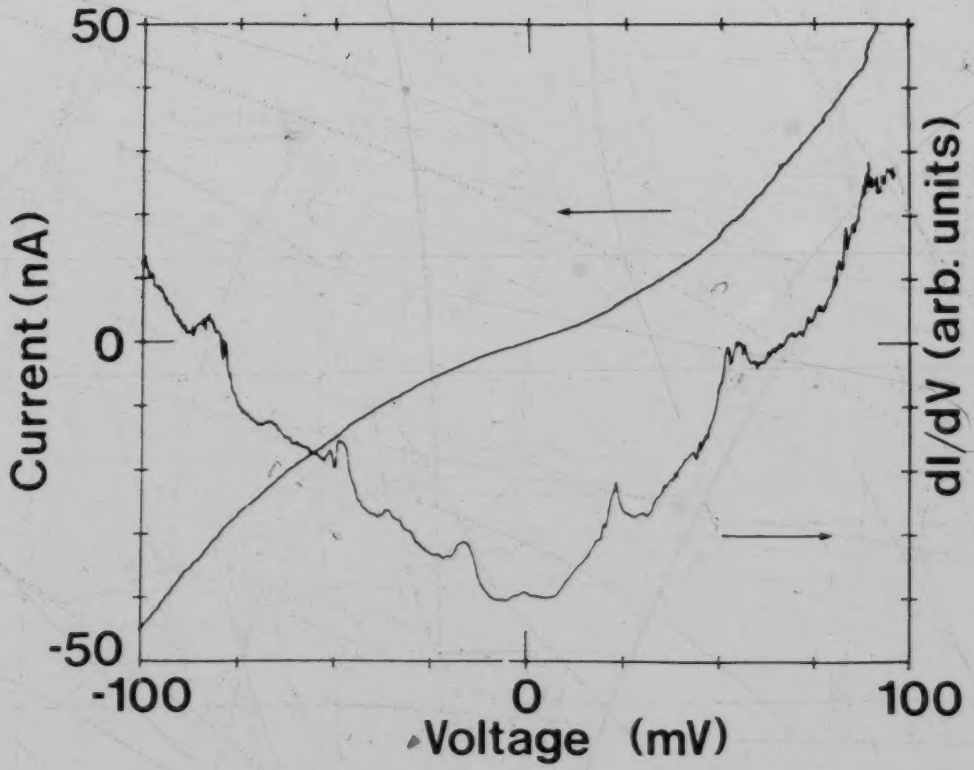
50
0
-50
Current (nA)
-100
0
100
Voltage (mV)
dI/dV (arb. units)

Fig. 4.16(c). This small, sharp gap was observed on each of the ceramic YBC and Al YBC samples. Fig. 4.18 was obtained on a YBC sample using a W tip, the quality of the superconducting characteristics are, like Fig. 4.16(c), quite high.

Evident in Fig. 4.18 are a number of peaks in the curve which lie outside the gap region. At any particular spot on the surface these peaks remained stable over many sweeps, however when a similar gap was observed at a different spot, the peaks generally appeared at different voltages. The peaks are not symmetric in energy, as would be expected if one was observing structure in the density of states due to phonon mediated pairing. The variation between different locations on the surface, and the lack of symmetry makes the origin of these peaks a mystery.

The size of the small sharp energy gap was $2\Delta = 5.0 \pm 0.5$ meV, which considering the 88 K transition temperature, yields a value $2\Delta/k_bT_c = 0.7$ far below the BCS weak coupling limit. A probable explanation for this gap is the presence of a low temperature phase in the ceramic samples. A low temperature phase would explain why no evidence of this gap was found at 77 K, and why no small gap was observed in the YBC single crystal samples.

The spatial variation observed in the tunneling characteristics may arise from multiple phases within the samples. Despite the fact that X-ray analysis of the YBC and Al YBC samples showed them to be single phase, this does not rule out small inclusions of a different phase. The variation may also be related to the extremely short coherence lengths in these novel superconductors (Gallagher, 1988). The short coherence length prevents the superconducting wavefunction from averaging over inhomogeneities, and results in normal or even insulating regions within the sample. These regions may result from areas of oxygen deficiency, grain boundaries or even

FIGURE 4.18 dI/dV data obtained on a ceramic $YBa_2Cu_3O_{6.5+x}$ sample using a W tip.

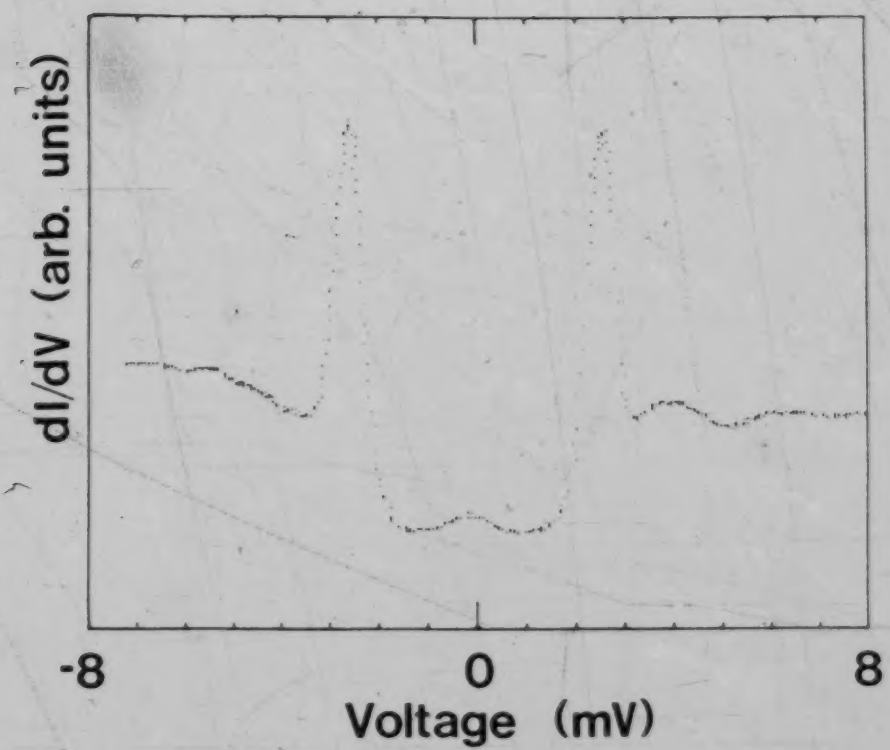
dI/dV (arb. units)
-8
0
8
Voltage (mV)

twin boundaries (Deutscher and Müller, 1987). At any point where an insulating region separates two areas of superconductivity, an S-I-S junction is formed. In specimens such as this the macroscopic superconducting properties are limited by Josephson coupling between adjacent microscopic regions within the sample. Josephson coupling between grains has been observed by point-contact spectroscopy using normal metal tips (Estève et al, 1987), and is also used to account for much of the critical current data (Chaudhari et al., 1988).

The extremely short coherence length puts stringent requirements on the surface quality of the samples. Superconducting tunneling is only sensitive to electrons which reside within a coherence length of the sample surface, which in these materials means a few atomic layers. In this case the measured value of the energy gap would depend strongly on the condition of the surface at each point (Gavaler et al., 1989).

In the same way as Estève et al (1987) ascribed their I-V characteristics to coupling between superconducting regions within the sample, many of the curves which exhibit large apparent gaps may be examples of S-I-S tunneling between coupled regions within the sample. As a result, the curves may be due to a multiplicity of Δ values. The different possible tunneling mechanisms makes an unambiguous estimate of Δ for each curve difficult.

Tunneling between a series of grains within the sample may be help explain curves such as Fig. 4.19, which indicates a different gap value depending on the direction of current flow. If the current path is different in each direction, the coupling between adjacent superconducting regions will in general be different, and lead to a different apparent Δ.

FIGURE 4.19 I-V characteristic obtained between an aluminum-doped sample and a Nb tip. The curve exhibits a different gap value for each polarity.

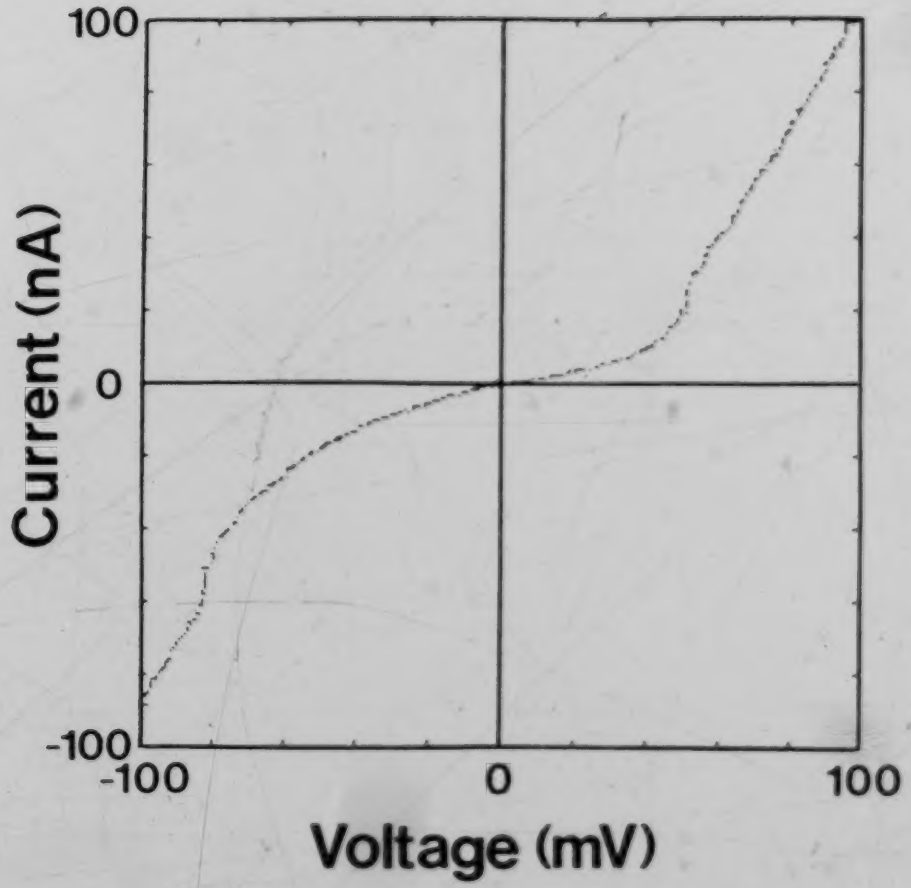
100
0
-100
Current (nA)
-100
0
100
Voltage (mV)

The curves obtained at lower tunneling resistances often contained an abundance of structure. In many cases the structure are examples of single electron tunneling in small capacitance tunnel junctions. In classical terms the tunnel junction is really just a capacitor. In most capacitors the gain or loss of a single electron is hardly noticed, however if the capacitance is small enough, the addition of one electron can change the electric potential across the junction by several millivolts. This change in energy can impede the tunneling electron and block current flow. The so called Coulomb blockade was first observed by Giaever and Zeller (1968) in a tunnel junction containing small isolated metal grains within the barrier. The capacitance of the grains was low enough to impede tunneling at low voltages.

In a tunnel junction biassed at a voltage V, the electron gains an energy eV as it crosses the barrier. If the junction has a capacitance C the potential across the junction is reduced by an amount e/2C. For this reason no current can flow as long as $V<e/2C$, and the junction exhibits a high resistance. In the I-V curve this means a low slope for voltages less then e/2C (Fig. 4.20(a)). The offset in the otherwise linear I-V is the signature of the Coulomb blockade. The effect is only observed if the charging energy $e^2/2C>k_BT$ since non zero temperature produces a number of empty states below e/2C. In addition to the early experiments by Giaever and Zeller, the Coulomb blockade has recently been observed in a small area tunnel junctions by Fulton and Dolan (1987), and by STM (van Bentum, 1988b). The shape of the I-V characteristic due to the Coulomb blockade is in many ways similar to superconducting curves, and so care must be taken to distinguish the two.

If two small capacitance junctions are connected in series, the Coulomb blockade is still observed, however under special circumstances ($R_1<<R_2$, and $C_1<C_2$) the I-V curve exhibits a series of current steps with a voltage spacing of

FIGURE 4.20 If the capacitance C of a tunnel is small enough the addition of one electron can change the electric potential across the junction. This charging energy can impede tunneling at low voltages (a). With two such junctions connected in series and with $R_1 << R_2$ and $C_1 < C_2$, a series of current steps may be observed (b).

(a)

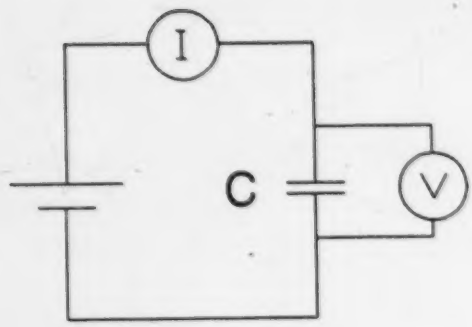

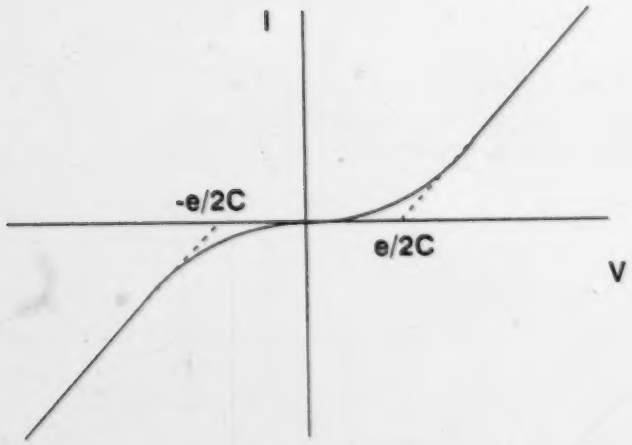

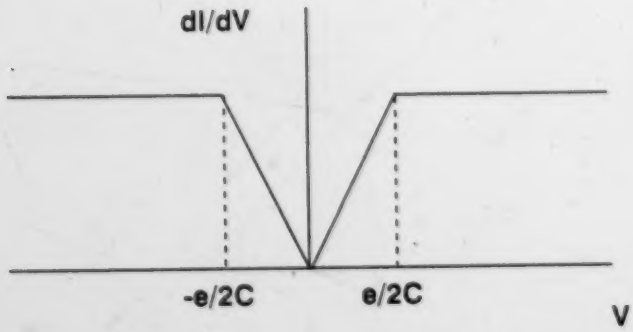

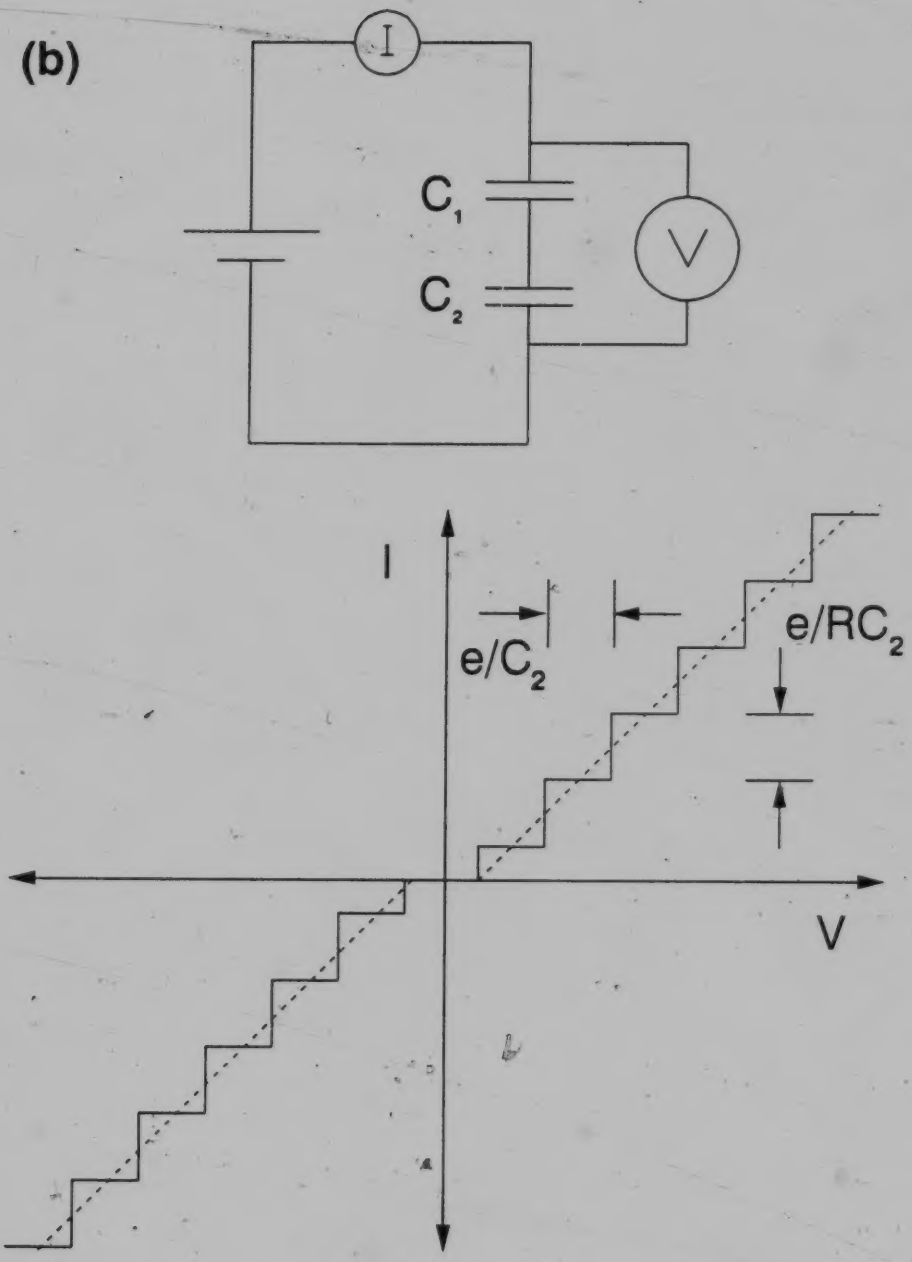
(b)
I
C1
C2
V
I
e/C2
e/RC2
V

$e/(C_1+C_2)$ (Mullen et al., 1988). The origin of the steps, or the Coulomb staircase, is related to the fact that the Fermi level of the interjunction region is free to shift as the amount of charge in the region changes. Since the amount of charge is quantized, the change in the Fermi level increases stepwise in response to the incremental electrostatic energy associated with each additional electron. Tunneling is only possible if there are available states at an energy below eV. The electrostatic energy prohibits tunneling at voltages less than $e/2(C_1+C_2)$, or the voltage required to overcome the charging energy. The tunneling of each subsequent electron requires an additional voltage $e/(C_1+C_2)$, and produces a series of current steps in the I-V curve in a characteristic 1:3:5 spacing (Fig. 4.20(b)). To observe the steps the tunneling rate of the first junction must be larger than the second. In this way the central region will always be "full", or take on the largest amount of charge allowed by the charging energy. This condition is satisfied if $R_1<R_2$ or $C_1<C_2$.

Experimentally the Coulomb staircase was first observed by Barner and Ruggiero (1987) who tunneled into an ensemble of isolated Ag particles embedded into the oxide layer of a tunnel junction. The staircase was also observed with the STM by van Bentum et al. (1988), and similar structure has also been observed by a number of authors investigating high T_c superconductors with the STM (Naito et al., 1987; Kirk et al., 1987; & Kirtley et al., 1987b).

The curve in Fig. 4.17 is clearly an example of the Coulomb staircase. Despite the fact that the steps are not resolved in the I-V, the resultant peaks in dI/dV are clearly visible. The existence of the staircase indicates that the tunneling mechanism was via an isolated particle on the surface of the crystal. The spacing between the peaks suggests a capacitance of $4.3\text{x}10^{-18}$ F, or a particle diameter of the order of

100 Å. The nature of the particle is unknown, however similar effects have been seen on single crystals by other workers (Kirtley et al., 1987; van Bentum et al., 1988c).

The Coulomb staircase was also observed on the ceramic Bi samples. Fig. 4.21 illustrates a series of curves obtained at one position on the surface of a ceramic $BiSrCaCu_2O_x$ sample using a W tip. Curves 4.21(a) and (b) obtained at lower junction resistance are clear examples of the Coulomb staircase. Although the structure of both curves is due to incremental charging, the curves do exhibit a number of deviations from the theory, which should be addressed.

The most striking deviation is the presence of a Josephson current in curve (a). This curve was obtained at the lowest tunneling resistance and indicates strong coupling between superconducting grains within the sample. The coexistence between pair tunneling and charging effects was first observed by Iansiti et al. (1988) using small area Sn Josephson junctions. Curves (a) and (b) also differ from theory in the sense that the curves exhibit sharp voltage, rather than current steps. This difference may be related to the fact that the experiment was performed using a near constant current load line, while the theory (Mullen et al., 1988) and much of the other experimental work (Barner and Ruggeiro, 1987; van Bentum et al, 1988; McGreer et al., 1989; Wilkins et al., 1989) was obtained using a constant voltage supply. van Bentum et al. (1988c) have performed a Monte Carlo simulation using a constant current load line to calculate the I-V characteristics. They concluded that the Coulomb staircase may still be observed without a constant voltage load line, and that the curve will still exhibit current steps. The exact reason Fig. 4.21 exhibits sharp voltage plateaus is not known, however the periodic spacing is still clear evidence of incremental charging.

FIGURE 4.21 I-V and dI/dV characteristics obtained at one position on a $BiSrCaCu_2O_x$ sample with a W tip. As the tunneling resistance is increased the curves show a transition from tunneling between Josephson coupled grains exhibiting a Coulomb staircase (a), to a featureless curve at higher resistance (d).

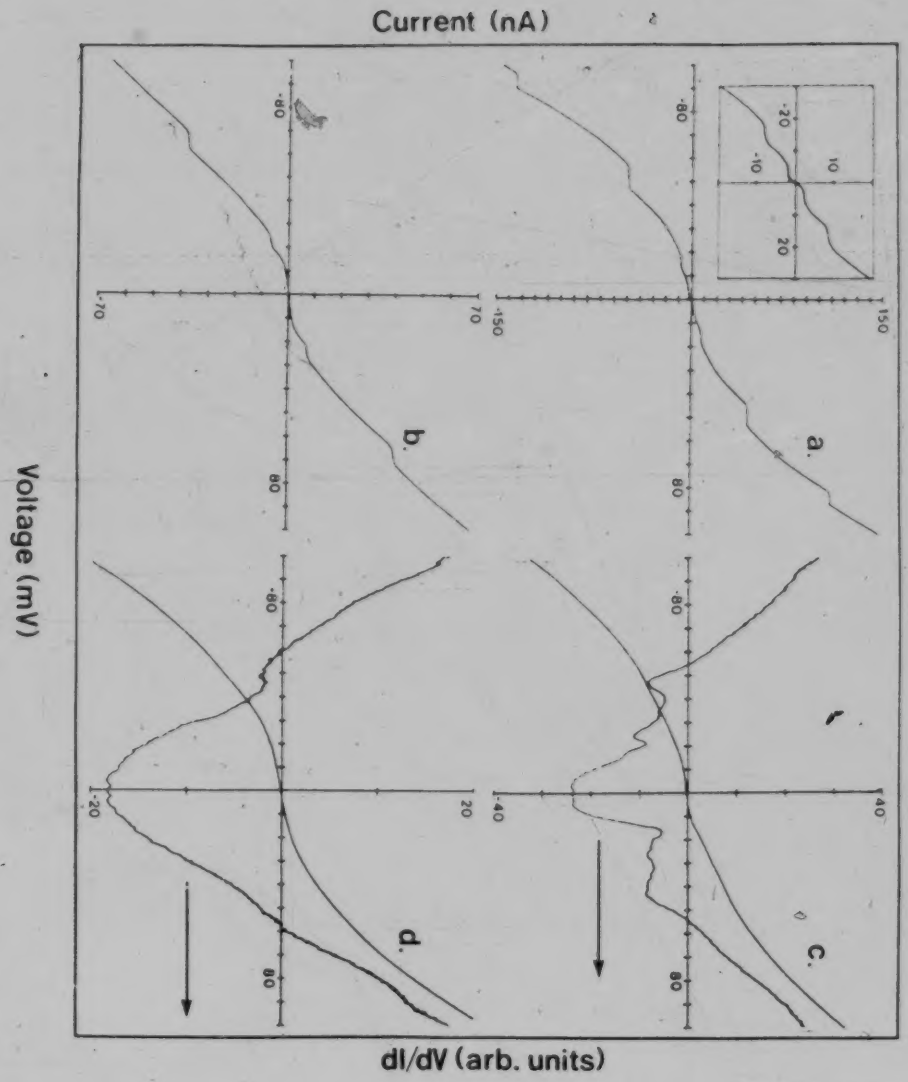
Current (nA)
Voltage (mV)
dI/dV (arb. units)
a.
b.
c.
d.
-80
80
-150
150
-70
70
-40
40
-20
20
-10
10

Another peculiarity in the data was the dependence of the step spacing on the tunneling resistance. The periodicity of the steps could be changed by adjusting the tunneling resistance. By increasing R the voltage spacing between steps was increased. According to theory (Mullen et al., 1988) to observe clear steps $C_1 < C_2$ and $R_1 << R_2$, and the step spacing is $e/(C_1+C_2) \sim e/C_2$ with a height of $e/R_2(C_1+C_2) \sim e/R_2C_2$. It was observed that the height of the steps remained constant, independent of the voltage spacing. This implies that $C_2 \propto 1/R_2$, despite the fact that tunneling theory predicts $C_T \propto 1/\ln(R_T)$. The origin for this dependence is unknown.

The staircase structure appears superimposed onto a non-linear I-V characteristic. The background curve indicates that the experiment does not measure the response of a single grain, but instead a parallel array of coupled junctions. Often times one or more grains contributed additional steps to the I-V characteristics making quantitative interpretation of the curves difficult.

One characteristic feature of not only this data, but all other STM reports of the staircase, is the size of the capacitance. Inevitably capacitances of 10^{-18} F are observed, yielding particle sizes of the order of 100 Å irrespective of the system (van Bentum et al, 1988; McGreer et al., 1989; Wilkins et al., 1989). Theoretically there is no factor which favours particles of this size, yet experimentally this seems to be the case. One feature common to all the measurements is the tunnel tip. The small capacitance may be an intrinsic property of the tip rather than the substrate. Clearly more work needs to be done in this regard, in particular topographic measurements of grains exhibiting the staircase should be made and compared with charging predictions.

In addition to charging effects, Fig. 4.21 indicates how the tunneling characteristics depended strongly on the tip to sample coupling. Curves (a) and (b) display single electron charging, and (a) exhibits strong coupling between superconducting grains within the sample. Despite this, curve (d) obtained at a larger tunneling resistance, displays a rather featureless I-V and dI/dV. At intermediate coupling Fig. 4.21(c) could easily be interpreted as a superconducting energy gap. This interpretation is not unique however, since the structure may be an example of a Coulomb blockade.

If the curve 4.22(c) is related to the superconducting density of states it is unclear why the gap disappears at larger tunneling resistances. It may be that the short coherence length limits observation of the energy gap to a small range of tip and sample coupling. The presence of the Josephson current at low tunneling resistance, indicates that the dominant tunneling mechanism may be S-I-S tunneling between grains within the sample. In this case the gap may only be observed when the tip makes metallic contact to one grain, and tunneling occurs between grains within the sample. Tunneling between grains yields an energy gap value, $2\Delta \sim 17$ meV. Much like the curves obtained on the YBC and Al YBC samples, the ambiguity concerning the exact tunneling mechanism makes interpretation of the curves difficult.

In summary, STM measurements performed on a number of superconducting samples failed to produce a definitive value for the energy gap in these materials. In all the samples a non conducting surface layer made it impossible to perform topographic measurements at low temperatures, and made it necessary to imbed the tip in order to tunnel. The tunneling characteristics exhibited extensive spatial variations, and many curves suggested tunneling between a series of coupled grains

within the sample. A small 5 meV gap was observed in the YBC and Al YBC ceramic samples, however this is probably related to a low temperature phase in these samples. The tunneling characteristics also depended strongly on the coupling strength between the sample and tip. Curves obtained at lower tunneling resistances often exhibited structure related to charging effects. In one particular example (Fig. 4.22), the curves obtained at lower tunneling resistances exhibited a Coulomb staircase and Josephson tunneling between grains, yet curves obtained at larger tunneling resistances were rather featureless.

The results indicate that much of the variation may be ascribed to the short coherence length in these materials, and many curves exhibit structure which arises from trying to perform local tunneling measurements on granular materials.

4.4.2.3 Topographic and Spectroscopic Studies of $YBa_2Cu_3O_x$ Films

In addition to spectroscopic measurements, the low temperature STM was used to study the surface properties of a number of YBC films[1]. Unlike previous measurements on the oxide superconductors, the surface layer of the films remained conducting at low temperatures. This eliminated the need to drive the tip into the surface, and allowed the full capabilities of the STM to be exploited by correlating spectroscopic data with topographic measurements.

The films were fabricated by rf sputtering from a single YBC target onto an alumina stabilized MgO substrate. After sputtering, the samples were removed from the preparation chamber and annaealed in an O_2 atmosphere. The samples were

1. Films provided by J. Vrba, CTF Systems Inc., Port Coquitlam B.C.

heated for a few minutes at between 900 and 950°C, then cooled rapidly to 500°C and annealed for a few hours. The nominal thickness of the films was 2 μm, and the zero resistance temperatures ranged from 75 to 80 K.

Both the bimorph microscope and the tube were used to obtain the measurements. Contrary to previous experience on single crystal and ceramic YBC samples, little evidence was found for a non-conducting layer on the surface of the films at 4.2 K. Stable topographic images were obtained with tunneling voltages as low as 2 mV with no sign of tip contact.

Large area STM scans indicated a granular surface with a large distribution in grain size (Fig. 4.22). The observations were consistent with scanning electron micrographs (SEM) (Fig. 4.23). Despite the granular nature, the film surface was rather smooth. The greatest relief, as measured by the STM, was 100 nm and in contrast to the 1 μm value reported by Niedermann and Fischer (1989) for similarly prepared films.

The conducting surface may be related to the presence of a thin surface layer. Cross sectional SEM images, obtained after breaking the samples, indicated that the brief heating of the samples was sufficient to produce a smooth shell a few tenths of a micron thick (Fig. 4.24).

Small area scans were obtained on the flat surfaces of individual grains. The scans showed no signs of atomic corrugations, or structure indicative of twin boundaries characteristic of the a-b plane in YBC (van de Leemput et al., 1988; Laiho et al., 1988; Anselmetti et al., 1988; Vieira et al., 1988). Instead the surface appeared rough and disordered on an atomic scale. The degree of roughness was of the order of 15 Å, and consistent with the single crystal results of van de Leemput et

FIGURE 4.22 Large area STM scan of the surface of a $YBa_2Cu_3O_x$ film at 4.2 K. The surface is polycrystalline with a large variation in grain size.

10 nm/div
100 nm/div
100 nm/div

FIGURE 4.23 Scanning electron micrograph of the surface of a $YBa_2Cu_3O_x$ film. The image is in agreement with large area STM scans.

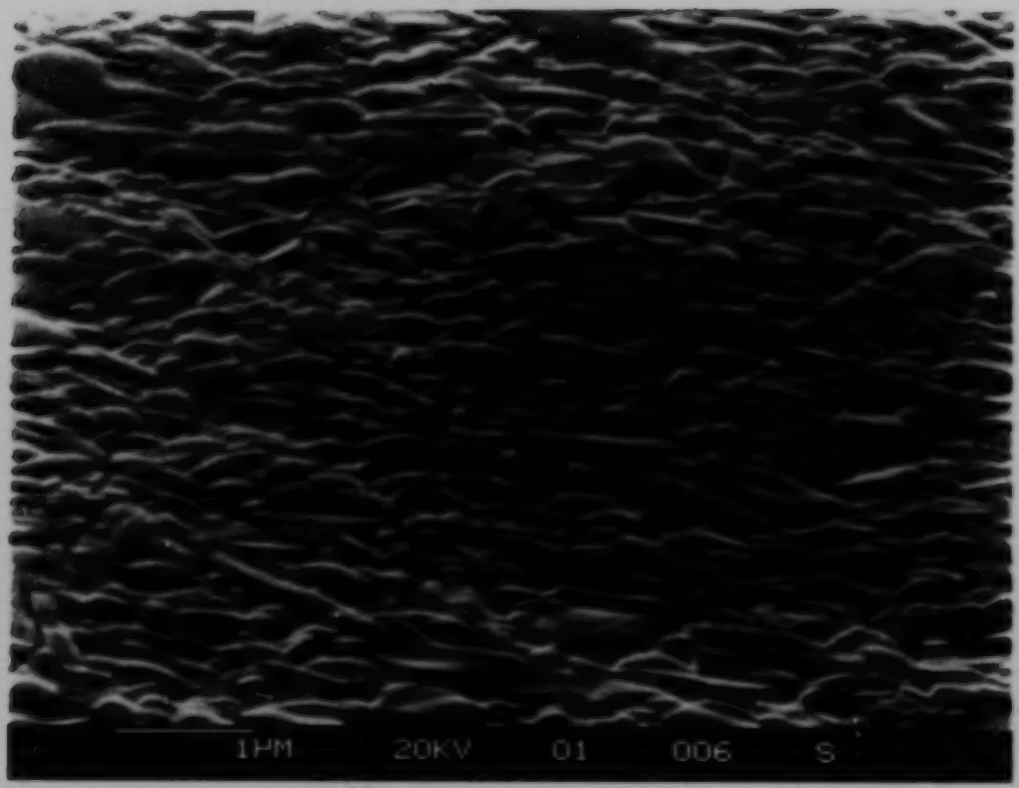
1PM
20KV
01
006
S

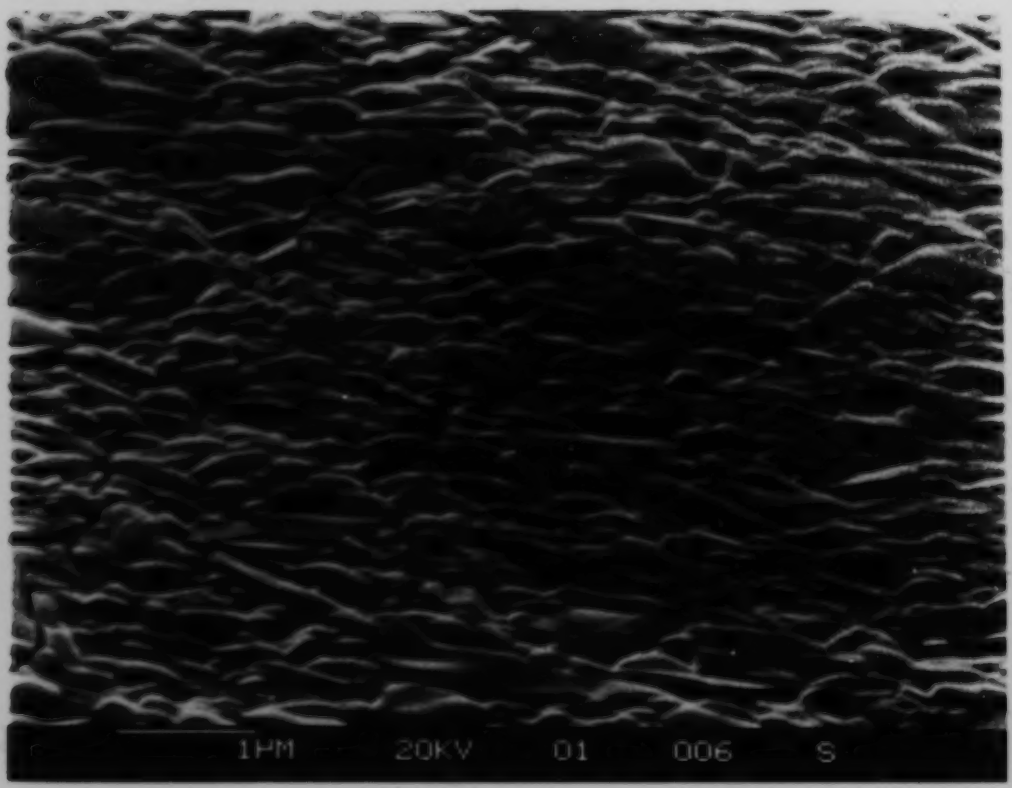
1MM 20KV 01 006 S

FIGURE 4.24 A cross sectional SEM image obtained by breaking the film. The image indicates the presence of a smooth shell a few tenths of a micron thick at the surface.

PAGINATION ERROR.

TEXT COMPLETE.

ERREUR DE PAGINATION.

LE TEXTE EST COMPLET.

NATIONAL LIBRARY OF CANADA.
CANADIAN THESES SERVICE.

BIBLIOTHEQUE NATIONALE DU CANADA.
SERVICE DES THESES CANADIENNES.

al. (1988) for tunneling parallel to either the [100] or [010] directions in the crystal. The results suggest that the grains at the surface of the films have a preferred orientation, with the a-b copper oxide planes oriented normal to the surface.

This orientation may also contribute to the conducting nature of the surface of these films. Both the electrical conductivity and the superconducting coherence length are larger in the a-b plane (Gallagher, 1988). The superior electrical properties may contribute to the improved surface characteristics.

It would seem, from the cross sectional SEM photographs, and the STM topography, that the brief heating of the films at 900^{o}C is sufficient to produce a relatively smooth, and conducting shell at the surface. The morphology of the surface of the film is different from that of the bulk. To better understand the nature of this surface layer, and in particular to determine if it is superconducting, we performed spectroscopic measurements at different points on the surface.

The measurements were performed using a sample and hold technique to momentarily break the feedback loop while the current voltage characteristics were obtained. The vast majority of the curves indicated that the surface was metallic, and at some positions superconducting characteristics were observed (Fig. 4.25).

Many curves exhibited signs of single electron tunneling due to the microscopic nature of the tip (van Bentum et al., 1988c). The curves were highly resistive at low bias resulting from a Coulomb blockade of electrons (Zeller and Giaever, 1969), with a characteristic offset from zero volts at higher voltages (Fig. 4.26). The shape of curves exhibiting a Coulomb blockade are similar to superconducting characteristics,

FIGURE 4.25 Current-voltage curves obtained at different points on the surface as indicated. Curves (a) and (b) are examples of Andreev reflection and indicate strong coupling between the sample and tip. Curves (c) and (d) are examples of quasiparticle tunneling and weak tip to sample coupling.

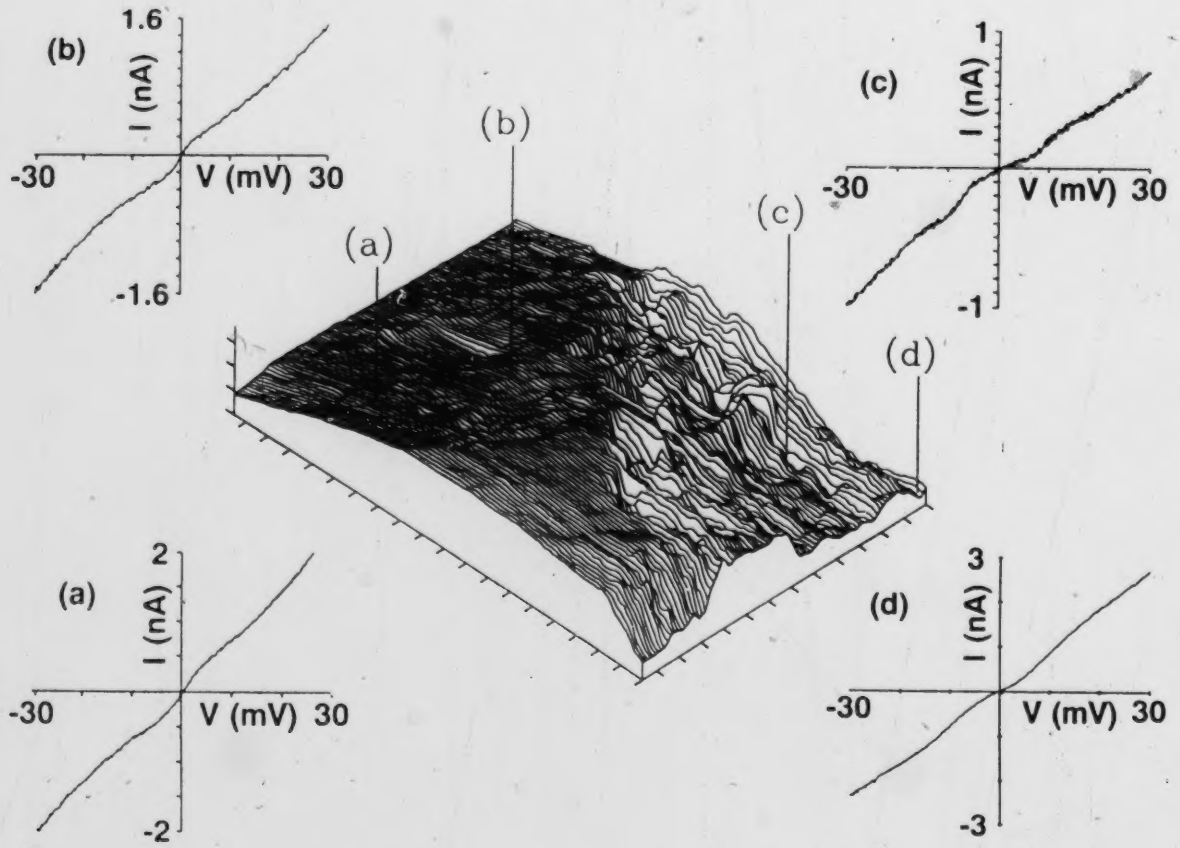
(b)
1.6
I (nA)
-30
V (mV) 30
-1.6
(c)
1
I (nA)
-30
V (mV) 30
-1
(a)
(b)
(c)
(d)
(a)
2
I (nA)
-30
V (mV) 30
-2
(d)
3
I (nA)
-30
V (mV) 30
-3

FIGURE 4.26 I-V characteristic obtained at one position which exhibits a Coulomb blockade.

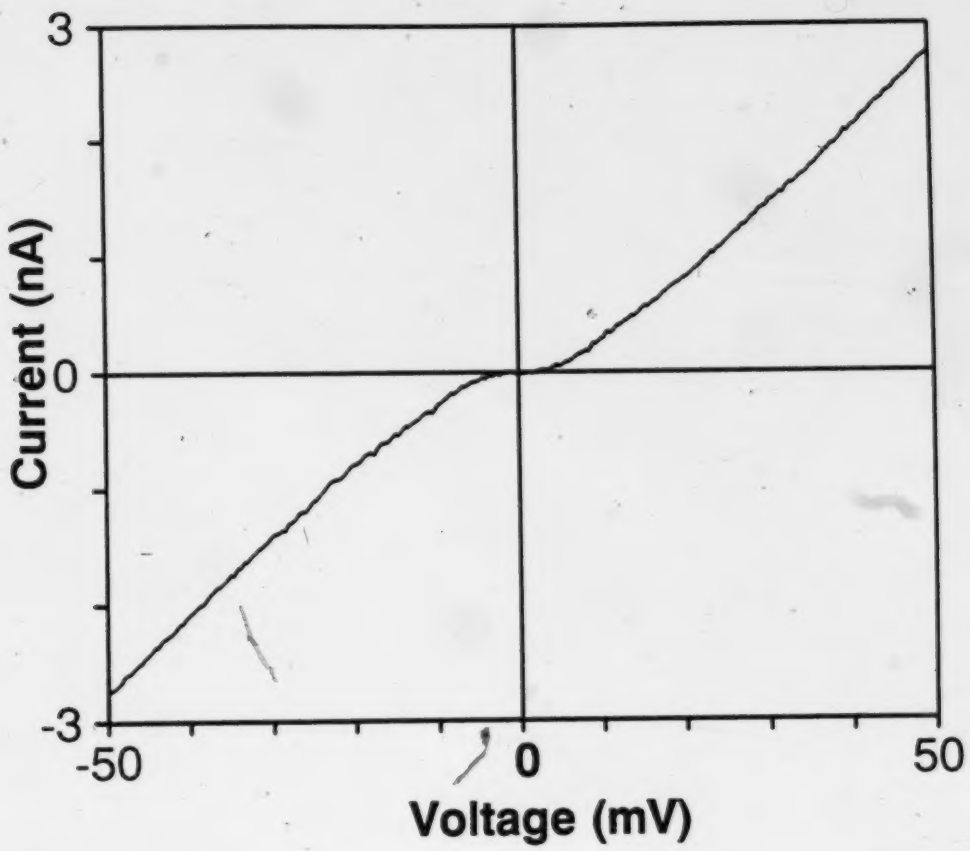
3
0
-3
Current (nA)
-50
0
50
Voltage (mV)

and so required careful interpretation. In one instance a curve with a series of current steps was observed (Fig. 4.27) indicating tunneling via a small particle on the surface of the film (Mullen et al., 1988; Barner and Ruggiero, 1987).

Charging of the surface may explain why at times a series of I-V curves recorded consecutively at the same position on the surface yielded different characteristics (Coleman, 1989). Often the curves only varied for the first few sweeps until an equilibrium curve was obtained.

Many of the curves exhibiting superconducting behaviour were of rather poor quality, however they do demonstrate that superconductivity can extend out to the surface of the films. Different superconducting curves indicated varying degrees of coupling between the surface and the tip. Curves (c) and (d) of Fig. 4.25 are examples of quasiparticle tunneling, and indicate a weak tip-sample interaction, while curves (a) and (b) indicate quasiparticle injection and strong coupling. Injection, or Andreev reflection, occurs at a normal metal-superconductor interface. An electron from the normal metal, with an energy $|E| < \Delta$, impinging on the interface reflects a hole of equal and opposite momentum back into the metal. At the same time a Cooper pair is added to the condensate of the superconductor. The process tends to dominate for strong coupling between the sample and tip (Blonder and Tinkham, 1983). Injection provides unambiguous evidence of superconductivity.

Andreev reflection was observed despite the fact we found no evidence of tip contact. In Fig. 4.25 the strong coupling curves occurred above a relatively smooth region, while the tunneling curves were obtained over a rougher area. The reason why strong coupling between the tip and sample was observed in the smooth region is unclear. It may be the additional roughness indicates the presence of a thin contamination layer?

FIGURE 4.27 Curves obtained at one position of the surface exhibiting a Coulomb staircase. The two curves were obtained sequentially, but the voltage was ramped in opposite directions. Although the signal to noise is poor the steps are clearly reproduced in both curves.

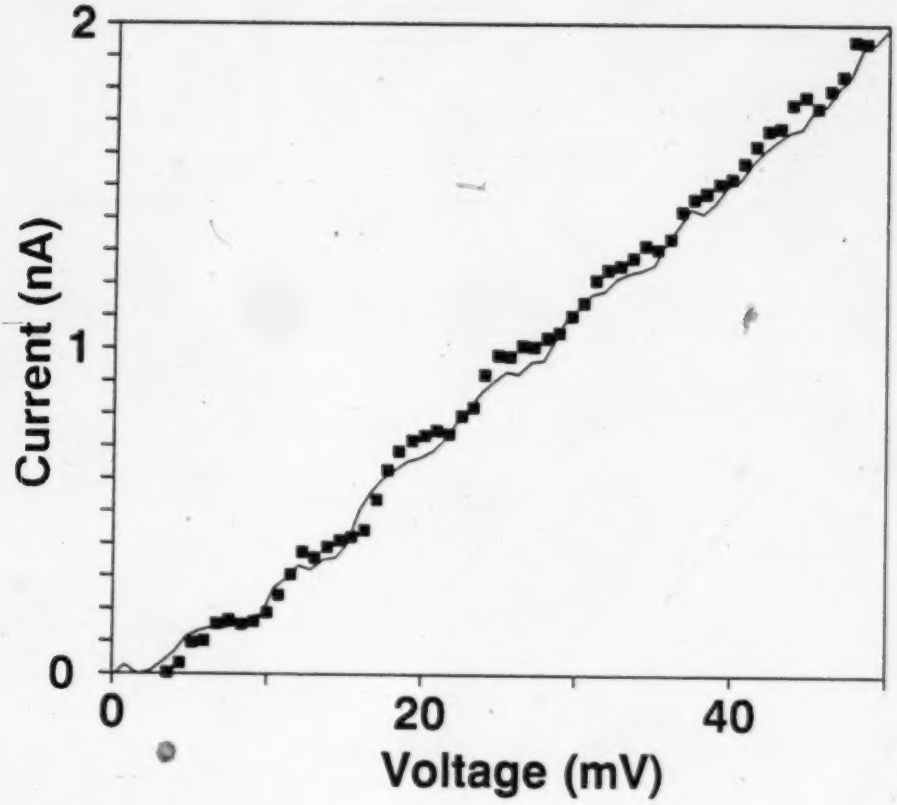
2
1
0
Current (nA)
0
20
40
Voltage (mV)

Like the previous measurements on ceramic samples the inferred gap value varied from point to point on the surface. Values as high as 20 meV were observed which, assuming a T_c of 75 K, yield a value $2\Delta/k_BT_c=3.3$. This value approaches the BCS weak coupling limit and is similar to the values reported by others (Kirtley et al., 1988a; Sera et al., 1988; van de Leemput et al., 1989). Since these measurements were obtained without driving the tip into the material, and at tunnel resistances an order of magnitude larger than the ceramics, contributions from tunneling within the sample were not observed.

The quality of the superconducting curves were quite poor. The curves exhibited large leakage currents below the gap and excessive broadening. The broadening has been observed by a number of authors and possible mechanisms have been discussed (Kirtley et al., 1988a; Ng et al., 1987; Dynes et al., 1984). Depairing can contribute to broadening. Depairing may occur as the result of the large current densities in the vicinity of the tunnel tip (Ng et al., 1987), or from short inelastic scattering rates in the films (Dynes et al., 1984). Charging effects can also contribute to broadening (Kirtley et al., 1988a). As electrons move on and off a grain the potential fluctuates by an amount e/C (where C is the capacitance of the grain) smearing the characteristic. Considering the frequency with which charging effects were observed at normal regions, it is probable that this mechanism had a large effect.

The microscopic nature of the STM tip can also contribute to broadening in one other respect. Since the area probed by the STM is so small, the uncertainty principle can place a limit on energy resolution. The sharper the tip the more broadened the characteristics become (Kuk and Silverman, 1989).

Despite the fact that most regions of the surface were metallic, occasionally the feedback response became unstable over particular areas of the surface resulting in noisy patches in the tunneling images. By obtaining I-V curves on top of and adjacent to these regions (Fig. 4.28), it was possible to ascribe the instability to areas of reduced surface conductivity. Curve (b) indicates metallic behavior despite the presence of a small Coulomb gap. Curve (a) on the other hand, exhibits a small band gap and reduced conductivity.

Summarizing, we have used the STM to measure the topographic and spectroscopic characteristics of a number of YBC films. Film preparation produced a thin shell at the surface. The STM measurements were used to ascertain that the surface layer was predominantly metallic, and that superconductivity does persist out to the surface. Energy gap values as high as 20 meV were measured, despite excessive broadening. By combining spectroscopic information with tunneling images it was possible to correlate noisy patches with areas of reduced surface conductivity.

FIGURE 4.28 Topograph and curves showing quiet and noisy regions as discussed in the text.

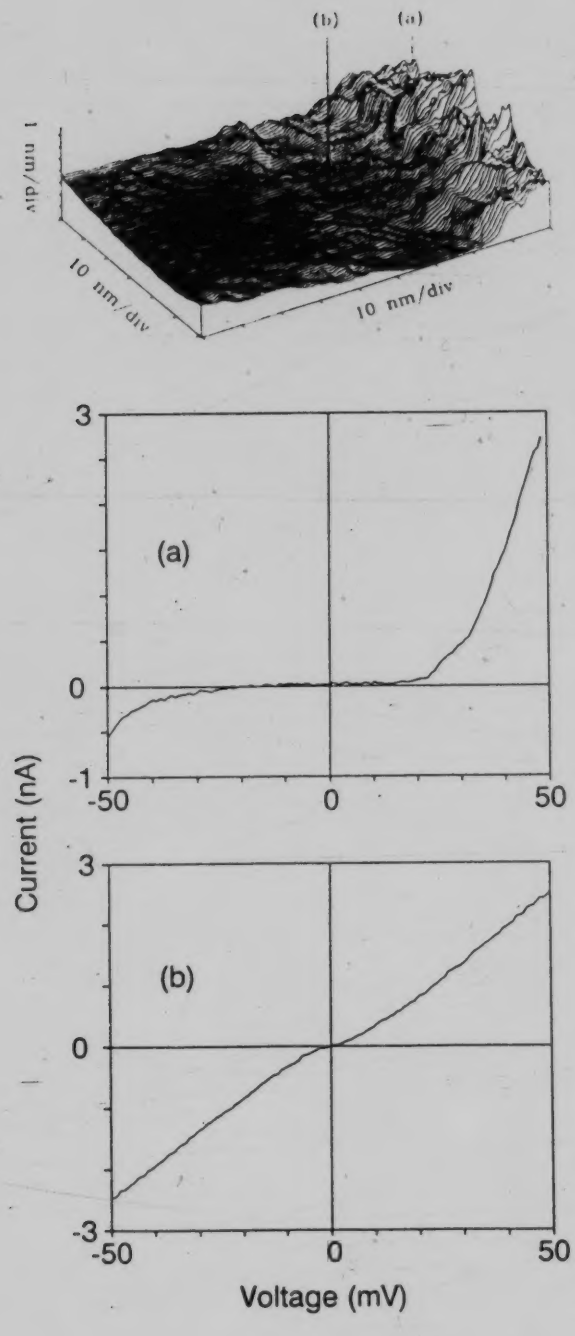
(b)
(a)
1 nm/div
10 nm/div
10 nm/div
3
(a)
0
-1
-50
0
50
Current (nA)
3
(b)
0
-3
-50
0
50
Voltage (mV)

5 Summary and Conclusions

5.1 Discussion

This thesis has outlined two series of experiments encompassing different aspects of electron tunneling.

The technique of inelastic electron tunneling spectroscopy was used to investigate the effect of different preparation conditions on the tunneling characteristics of undoped Mg-MgO-metal tunnel junctions. The results indicate that much of the observed variation may be ascribed to differences in the structure of the barrier. The tunneling characteristics of the tunnel junctions could be improved by increasing the uniformity of the oxide layer. Uniform oxide growth could be achieved by oxidizing in a wet environment, or by pretreating the Mg film with atomic hydrogen. Magnesium oxidized in a dry system produced junctions with poor tunneling characteristics, indicative of a patchy barrier.

The hydrogen pretreatment resulted in hydrogen being chemisorbed at the magnesium surface, as evidenced by a large peak in the IET spectra at 124 meV. The chemisorbed hydrogen acted as an additional nucleation site for MgO oxidation, promoting more uniform growth.

The uniformity of the barrier was apparent when junctions were prepared with different cover electrodes. Both the IET spectra, and the elastic tunneling characteristics of hydrogen treated junctions seemed less effected by the choice of cover electrode. The barrier parameters indicated that metals with smaller ionic radii reduced the apparent barrier height of the junction by penetrating the oxide at pinholes and defects. The effect was reduced in hydrogen treated junctions

indicating a smaller degree of imperfections. The degree of penetration was such that junctions with Al or Mg cover electrodes could only be produced after hydrogen pretreatment.

Different cover electrodes produced a shift in the 450 meV hydroxyl peak to lower energies. The shift was attributed to the proximity of the hydroxyl to the cover electrode in agreement with Kirtley and Hansma (1976b). The shift was larger with the Mg negatively biassed. The bias dependence may result from the fact that electrons tunneling out of the magnesium are more likely to excite hydroxyls closer to the covermetal where the shift is largest.

The technique of low temperature scanning tunneling microscopy was also discussed. The design and operation of low temperature microscopes were presented, including preparation of tunneling tips, and piezoelectric calibration using a graphite lattice.

To test the capabilities of the low temperature system, topographic and spectroscopic measurements were performed on $NbSe_2$ at 4.2 K. The results indicate that the microscopes are capable of obtaining atomic resolution while at the same time measuring the tunneling characteristics at any point on the surface with millivolt resolution.

Using low temperature STM, the surface properties of a number of high temperature superconductors were measured. The presence of a non-conducting surface layer on the majority of these samples made it impossible to utilize the scanning capability of the STM since the tip had to be driven into the surface to obtain a tunnel current.

Experiments obtained with the stuck tip failed to produce a definitive energy gap value. Instead, the extremely short coherence lengths in these materials produced large spatial variations in the tunneling characteristics. In many cases the characteristics were dominated by tunneling between a series of grains within the sample rather than tunneling between the sample and tip. This provided uncertainty as to the exact tunneling mechanism, and made an unambiguous estimate of the energy gap impossible. A sharp 5 meV gap was observed in the ceramic YBC and Al doped YBC materials indicating a low temperature phase in these samples.

The tunneling curves also depended to a great extent on the strength of the coupling between the sample and tip. Curves obtained at lower tunneling resistances often showed evidence of charging effects such as the Coulomb staircase (Mullen et al., 1988). In one particular case, the tunneling characteristics between a $BiSrCaCu_2O_x$ sample and a W tip evolved from a curve exhibiting a Coulomb staircase with Josephson coupling between grains, to a rather featureless characteristic by increasing the tunneling resistance.

The non-conducting surface layer was not a problem on a series of YBC films. The surface of the films exhibited a thin conducting shell, and spectroscopic measurements indicated that superconductivity did persist out to surface of the films. While many of the curves exhibited charging effects related to the microscopic nature of the tip, curves showing evidence of quasiparticle tunneling and Andreev reflection were observed. Despite excessive broadening, energy gap values as high as 20 meV were measured. Combining topographic information with spatially resolved spectroscopic data, it was possible to relate regions of unstable feedback response to areas of reduced surface conductivity.

5.2 Suggestions for Further Work

The results of the IETS experiments indicated that hydrogen pretreatment of the magnesium electrode can promote uniform growth of the oxide barrier to produce junctions with improved tunneling characteristics. The results on magnesium suggest that the technique should be applied to other base electrodes which produce "patchy" oxides i.e. Pb, Nb. Since the process provides an efficient method of introducing hydrogen, the pretreatment may also be used as a basis for IETS studies of hydrogen chemisorption in a variety of metals.

The STM experiments produced a number of interesting questions which should be addressed. The first concerns the excessive broadening of the superconducting tunneling characteristics obtained on the YBC films. It is not clear whether the broadening is an intrinsic property of the high temperature superconductors, related to the granular nature of surface, or inherent to the technique of low temperature STM. To address this question experiments need to be performed on materials with known superconducting characteristics. In this way variations in the tunneling characteristics may be related to changes in grain size or tip radius.

The second question concerns the observation of single electron tunneling effects with the STM, and in particular the observation of the Coulomb staircase. In addition to high temperature superconductors, the Coulomb staircase has been observed in a number of different systems (Naito et al.,1987; Kirk et al., 1987; Kirtley et al., 1987b; van Bentum et al., 1988; McGreer et al., 1989; Wilkins et al., 1989). Despite this, in all cases the observations imply capacitances of the order or 10^{-18} F, or a particle size of about 100 Å. Why the experiments continually favor this

extremely small particle size in different materials is unclear? To address this question more experiments need to be performed where observation of the staircase is combined with topograph measurements to try and characterize the nature of the isolated particle. In addition, the technique of scanning tunneling potentiometry (Kirtley et al., 1988b) could be used to determine the electrical contact between the particle and the rest of the sample.

6 Bibliography

Adkins, C.J. and Sleigh, A.K. (1987). J. Phys. C: Solid State Physics 20, 4307.

Adler, J.G. and Jackson, J.E. (1966). Rev. Sci. Instrum. 37, 1049.

Adler, J.G. (1969). Solid. Stat. Commun. 7, 1635.

Adler, J.G. (1982). in Tunneling Spectroscopy, Capabilities, Applications and New Techniques, P.K. Hansma ed., (Plenum, New York, 1982), p423.

Andreev, A.F. (1964). JETP 19, 1228.

Anselmetti, D., Heinzelmann, H., Wiesendanger, R., Jenny, H., Güntherodt, H.J., Düggelin, M. and Guggenheim, R. (1988). Physica C 153-155, 1000.

Aquista, N., Schoen, L., and Lide, D. (1968). J. Chem. Phys. 48, 1534.

Bando, H., Tokumoto, H., Mizutani, W., Watanabe, K., Okano, M., Ono, M., Murakami, H., Okayama, S., Ono, Y., Wakiyama, S., Sakai, F., Endo, K. and Kajimura, K. (1987). Jpn. J. Appl. Phys. 26, L41.

Bardeen, J., Cooper, L.N. and Schrieffer, J.R. (1957). Phys. Rev. 108, 1175.

Bardeen, J. (1961). Phys. Rev. Lett. 6, 57.

Barner, J.B. and Ruggiero, S.T. (1987). Phys. Rev. Lett. 59, 807.

Baró, A.M., Binnig, G., Rohrer, H., Gerber, Ch., Stoll, E., Baratoff, A., and Salvan, F. (1984). Phys. Rev. Lett. 52, 1304.

Bednorz, J.G. and Müller, K.A. (1986). Z. Phys. B 64, 189.

Binnig, G. Rohrer, H., Gerber, Ch. and Weibel, E. (1982a). Appl. Phys. Lett. 40, 178.

Binnig, G. Rohrer, H., Gerber, Ch. and Weibel, E. (1982b). Phys. Rev. Lett. 49, 57.

Binnig, G., Rohrer, H., Gerber, Ch. and Weibel, E. (1983a). Phys. Rev. Lett. 50, 120.

Binnig, G., Rohrer, H., Gerber, Ch. and Weibel, E. (1983b). Surf. Sci. 131, L379.

Binnig, G. and Smith, D.P.E. (1986) Rev. Sci. Instrum. 57, 1688.

Blonder, G.E., Tinkham, M. and Klapwijk, T.M. (1982). Phys. Rev. B 25, 4515.

Blonder, G.E. and Tinkham, M. (1983). Phys. Rev. B 27, 112.

Bogoliubov, N.N. (1958). Sov. Phys. JETP 7, 41.

Brinkman, W.H., Dynes, R.C. and Rowell, J.M. (1970). J. Appl. Phys. 41, 1915.

Buchanan, R.A., Caspers, H.H., and Murphy, J. (1963). J. Appl. Opt. 2, 1147.

Cederberg, A.A. (1981). Surf. Sci. 103, 148.

Chaudhari, P., Mannhart, J., Dimos, D., Tsuei, C.C., Chi, J., Oprysko, M.M and Scheuermann, M. (1988). Phys. Rev. Lett. 60, 1653.

Coleman, R.V., Giambattista, B., Johnson, A., McNairy, W.W., Slough, G., Hansma, P.K. and Drake, B. (1988). J. Vac. Sci. Technol. A 6, 338.

Coleman, R.V. (1989). private Communication.

Dawson, P., Hadfield, C.D. and Wilkinson, G.R. (1973). J. Chem. Solids 34, 1217.

de Lozanne, A.L., Elrod, S.A. and Quate, C.F. (1985). Phys. Rev. Lett. 54, 2433.

Deutscher, G. and Müller, K.A. (1987). Phys. Rev. Lett. 59, 1745.

Drake, B., Sonnefeld, R., Schneir, J., Hansma, P.K., Slough, G., and Coleman, R.V. (1986). Rev. Sci. Instrum. 57, 1688.

Dynes, R.C., Garno, J.P., Hertel, G.P., and Orlando, T.P. (1984). Phys. Rev. Lett. 53, 2437.

Eley, D.D. and Wilkinson, P.R. (1960). Proc. R. Soc. London, Ser. A 254, 327.

Eliashberg, G.M. (1960). Zh. Eksp. Teor. Fiz. 38, 966 (Eng. trans. Sov. Phys.-JETP 11, 696).

Elrod, S.A., de Lozanne, A.L. and Quate, C.F. (1984). Appl. Phys. Lett. 45, 1240.

Estève, D., Martinis, J.M., Urbina, C., Dovoret, M.H., Collin, G., Monod, P., Ribault, M. and Revcolevschi, A. (1987). Europhys. Lett. 3, 1237.

Fisher, J.C. and Giaever, I. (1961). J. Appl. Phys. 32, 172.

Frenkel, J. (1930). Phys. Rev. 36, 1604.

Freud, F. and Wengler, H. (1982). J. Phys. Chem. Solids 43, 129.

Fulton, T.A., and Dolan, G.J. (1987). Phys. Rev. Lett. 59, 109.

Gallagher, W.J. (1988). J. Appl. Phys. 63, 4216.

Gavaler, J.R., Braginski, A.I., Forrester, M.G., Talvacchio, J. and Greggi, J. (1989). to be published in IEEE Trans. Magn. MAG-25.

Giaever, I. (1960a). Phys. Rev. Lett. 5, 147.

Giaever, I. (1960b). Phys. Rev. Lett. 5, 464.

Giaever, I. and Zeller, H.R. (1968). Phys. Rev. Lett. 20, 1504.

Giambattista, B., Johnson, A., Coleman, R.V., Drake, B. and Hansma, P.K. (1988). Phys. Rev. B 37, 2741.

Gjisen, J., Namba, H., Thiry, P.A., Pireaux, J.J. and Caudano, P. (1981). Appl. Surf. Sci. 8, 371.

Glass, A.M. and Searle, T.M. (1967). J. Chem. Phys. 46, 2092.

Gonzalez, R., Chen Y. and Mostoller, M. (1981). Phys. Rev. B 24, 6862.

Halbritter, J. (1983). IEEE Trans. Magn. MAG-19, 799.

Hansma, P.K. and Tersoff, J. (1987). J. Appl. Phys. 61, R1.

Harrison, W.A. (1961). Phys. Rev. 123, 85.

Herzberg, G. (1950). in Spectra of Diatomic Molecules (Van Nostrand, New York, 1950), p560.

Hess, H.F., Robinson, R.B., Dynes, R.C., Valles, J.M. and Waszczak, J.V. (1989). Phys. Rev. Lett. 62, 214.

Hjelmberg, H. (1979). Surf. Sci. 81, 539.

Hohn, N., Koltun, R., Schmidt, H., Blumenröder. S., General, H., Güntherodt, G. and Wohlleben, D.L. (1987). Z. Phys. B 69, 173.

Iansiti, M., Johnson, A.T., Lobb, C.J. and Tinkham, M. (1987). Phys. Rev. Lett. 60, 2414.

Igalson, J. and Adler, J.G. (1983). Phys. Rev. B 28, 4970.

Jaklevic, R.C. and I ambe J. (1966). Phys. Rev. Lett. 17, 1139.

Johansan, P.K. (1981). Surf. Sci. 104, 510.

Josephson, B.D. (1962). Phys. Rev. Lett. 1, 251.

Kane, E.O. (1969). In Tunneling Phenomena in Solids, E. Burstein and S. Lundqvist eds., (Plenum, New York, 1969), p1.

Kirk, C.T. Jr. and Huber, E.E. (1968). Surf. Sci. 9, 217.

Kirk, M.D., Smith, D.P.E., Mitzi, D.B., Sun, J.Z., Webb, D.J., Char, K., Hahn, M.R., Naito, M., Oh, B., Beasley, M.R., Geballe, T.H., Hammond, R.H., Kapitulnik, A. and Quate, C.F. (1987). Phys Rev. B 35, 8850.

Kirk, M.D., Nogami, J., Baski, A.A., Mitzi, D.B., Kapitulnik, A., Geballe, T.H. and Quate, C.F. (1988). Science 242, 1673.

Kirtley, J., Scalapino, D.J. and Hansma, P.K. (1976a). Phys. Rev. B 14, 3177.

Kirtley, J.R. and Hansma, P.K. (1976b). Phys. Rev. B 13, 2910.

Kirtley J.R., and Hall, J.T. (1980). Phys. Rev. B 22, 848.

Kirtley, J., Raider, S.I., Feenstra, R.M. and Fein, A.P. (1987a). Appl. Phys. Lett. 50, 1607.

Kirtley, J.R., Collins, R.T., Schlesinger, Z., Gallagher, W.J., Sandstrom, R.L., Dinger, T.R. and Chance, D.A. (1987b). Phys. Rev. B 35, 8846.

Kirtley, J.R., Feenstra, R.M., Fein, A.P., Raider, S.I., Gallagher, W.J., Sandstrom, R., Dinger, T. Shafer, M.W., Koch, R. Laibowitz, R. and Bumble, B. (1988a). J. Vac. Sci. Technol. A 6, 269.

Kirtley, J.R., Washburn, S. and Brady, M.J. (1988b). Phys Rev. Lett. 60, 1546.

Klein, J., Léger, A., Belin, M., Défourneau, D. and Sangster M.J.L. (1973). Phys. Rev. B 7, 2336.

Koch, H., Cantor, R., March, J.F., Eickenbusch, H. and Schollhorn, R. (1987) Phys. Rev. B 36, 722.

Konkin, M.K. and Adler, J.G. (1976). J. Appl. Phys. 50, 8125.

Kuk, Y. and Silverman, P.J. (1989). Rev. Sci. Instrum. 60, 165.

Laiho, R., Heikkila, L. and Snellman, H. (1988). J. Appl. Phys. 63, 225.

Lambe, J. and Jaklevic, R.C. (1968). Phys. Rev. 165, 821.

Lang, N.D. and Williams, A.R. (1978). Phys. Rev. B 18, 616.

Lang, N.D. (1985). Phys. Rev. Lett. 55, 230.

Lang, N.D. (1986). Phys. Rev. Lett. 56, 11.

Langan, J.D. and Hansma, P.K. (1975). Surf. Sci. 52, 211.

LeDuc, H.G., Kaiser, W.J., Hunt, B.D., Bell, L.D., Jaklevic, R.C. and Youngquist, M.G. (1989). Appl. Phys. Lett. 54, 946.

Leihr, M. and Ewert, S. (1983). Z. Phys. B 52, 95.

Liboff, R.L. (1980). Introductory Quantum Mechanics (Holden-Day, San Francisco, 1980).

Lippincott, E.R. and Schroeder, R. (1955). J. Chem. Phys. 23, 1099.

Mal'tseva, N.N. and Kharitonov, Y.Y. (1962). Zh. Neorg. Khim. 7, 489.

McGreer, K.A., Wan, J.-C., Anand, N. and Goldman, A.M. (1989). Phys. Rev. B 39, 12260.

McMillan, W.L. and Rowell, J.M. (1965). Phys. Rev. Lett. 14, 108.

Maeda, H.,Tanaka, Y., Fukutomi, M. and Asano, T. (1988) Jpn. J. Appl. Phys. 27, L209.

Miles, J.L. and Smith, P.H. (1963). J. Electrochem. Soc. 110, 1240.

Moreland, J., Ekin, J.W., Goodrich, L.F., Capobianco, T.E., Clark, A.F., Kwo, J., Hong, M. and Liou, S.H. (1987). Phys. Rev. B 35, 8856.

Morris, R.C., and Coleman, R.V. (1973). Phys. Lett. 43A, 11.

Mullen, K., Ben-Jacob, E., Jaklevic, R.C. and Schuss, Z. (1988). Phys. Rev. B 37, 98.

Naito, M., Smith, D.P.E., Kirk, M.D., Oh, B., Hahn, M.R., Char, K., Mitzi, D.B., Sun, J.Z., Webb, D.J., Beasley, M.R., Fischer, O., Geballe, T.H., Hammond, R.H., Kapitulnik, A. and Quate, C.F. (1987). Phys. Rev. B 35, 7228.

Namba, H., Darville, J. and Gilles, J.M. (1981). Surf. Sci. 108, 446.

Ng, K.W., Pan, S., de Lozanne, A.L., Panson, A.J. and Talvacchio, J. (1987). Jap. J. Appl. Phys. 26-3, 993.

Niedermann, Ph. and Fischer, Ø., (1989). J. Microsc. 152, 93.

Park, Sang-Il and Quate, C.F. (1985). Appl. Phys. Lett. 48, 112.

Pauling, L. (1949). Proc. R. Soc. London, Ser. A 196, 343.

Pickett, W.E. (1989). Rev. Mod. Phys. 61, 433.

Plesiewicz, W., and Adler, J.G. (1986). Phys. Rev. B 34, 4583.

Reichelt, K., Lutz, H.O., (1971). J. Cryst. Growth 10, 103.

Reynolds, S., Peasgood, A., Oxley, D.P., Pritchard, R.G., Walmsley, D.G., Tomlin, J.L. and Turner, R.J. (1987). J. Phys. C: Solid State Phys. 20, 4297.

Rieder, K.H. and Horl, E.M. (1968). Phys. Rev. Lett. 20 (1968).

Rowell, J.M. in Tunneling Phenomena in Solids (Eds. E. Burstein and S. Lundqvist, Plenum Press, New York, 1969), p274.

Sangster, M.J.R., Pekham, G. and Saunderson, D.H., (1970) J. Phys. C 3, 1026.

Scalapino, D.J. and Marcus, S.M. (1967). Phys. Rev. Lett. 18, 459.

Schneir, J., Sonnenfeld, R., Marti, O., Hansma, P.K., Demuth, J.E. and Hamers R.J. (1988). Appl. Phys. Lett. 63, 717.

Schrieffer, J.R., Scalapino, D.J. and Wilkins, J.W. (1963). Phys. Rev. Lett. 10, 336.

Sera, M., Shamoto, S. and Sato, M. (1988). Solid Stat. Commun. 65, 997.

Sheng Z.Z. and Hermann, A.M. (1988). Nature 332, 55; ibid., p. 138.

Simmons, J.G. (1963a). J. Appl. Phys. 34, 1973.

Simmons, J.G. (1963b). J. Appl. Phys. 34, 2581.

Sommerfeld, A. and Bethe, H.A. (1933). in Handbuch der Physik, S. Fugge ed. (Springer-Verlag, Berlin, 1933), Vol. 24, p150.

Sonnenfeld, R. and Hansma, P.K. (1986). Science 232, 211.

Talvacchio, J., Gavaler, J.R., Braginski, A.I. and Janocko, M.A. (1985). J. Appl. Phys. 58, 4638.

Tarascon, J.M., Le Page, Y., Barboux, P., Bagley, B.G., Greene, L.H., McKinnon, W.R., Hull, G.W., Giroud, M. and Hwang, M. (1988). Phys. Rev. B 37, 9382.

Tersoff, J. and Hamann, D.R. (1983). Phys. Rev. Lett. 50, 1988.

Tersoff, J. and Hamann, D.R. (1985). Phys. Rev. B 31, 805.

Tersoff, J. (1986). Phys. Rev. Lett. 57, 440.

Torardi, C.C, Subramanian, M.A., Calabrese, J.C., Gopalakrishnan, J., Morrissey, K.J., Askew, T.R., Flippen, R.B., Chowdhry, U. and Sleight, A.W. (1988). Nature 240, 631.

van Bentum, P.J.M., Hoevers, H.F.C., van Kempen, H., van de Leemput, L.E.C., de Nivelle, M.J.M.F., Schreurs, L.W.M., Smokers, R.T.M. and Teunissen, P.A.A. (1988a). Physica C 153-155, 1718.

van Bentum, P.J.M., van Kempen, H., van de Leemput, L.E.C. and Teunissen, P.A.A. (1988b). Phys. Rev. Lett. 60, 369.

van Bentum, P.J.M., Smokers, R.T.M. and van Kempen, H. (1988c). Phys. Rev. Lett. 60, 2543.

van de Leemput, L.E.C., van Bentum, P.J.M., Schreurs, L.W.M. and van Kempen, H. (1988). Physica C 152, 99.

van de Leemput, L.E.C., van Bentum, P.J.M., Schreurs, L.W.M. and van Kempen, H. (1989). J. Microsc. 152, 103.

Verma, M.P. and Dayal, B. (1967). Phys. Status Solidi 19, 751.

Vieira, S., Ramos, M.A., Buendia, A. and Baro, A.M. (1988). Physica C 153-155, 1004.

Walmsley, D.G., Nelson, W.J., Brown, N.M.D. and Floyd, R.B. (1980). Applic. Surf. Sci. 5, 107.

Wilkins, R., Ben-Jacob, E. and Jaklevic, R.C. (1989). to be published.

Willmott, J.G. (1956). Proc. Phys. Soc. B 69, 129.

Wolf, E.L. (1985). Principles of Electron Tunneling Spectroscopy (Oxford University Press, New York, 1985) p104.

Wu, M.K., Ashburn, J., Torng, C.J., Hor, P.H., Meng, R.L., Gao, L., Huang, Z.J., Wang, Y.Q. and Chu, C.W. (1987).

Young, Russell, Ward, John and Scire, Fred (1971). Phys. Rev. Lett. 27, 922.

Young, Russell, Ward, John and Scire, Fredric (1972). Rev. Sci. Instrum. B43, 999.

Zeller, H.R. and Giaever, I. (1969). Phys. Rev. 181, 789.